Steps towards a GaN nanowire based light emitting diode and its integration with Si-MOS technology

D I S S E R T A T I O N

zur Erlangung des akademischen Grades

Doctor rerum naturalium (Dr. rer. nat.)
im Fach Physik

eingereicht an der
Mathematisch-Naturwissenschaftlichen Fakultät I
Humboldt-Universität zu Berlin

von
Dipl.-Phys. Friederich Limbach

Präsident der Humboldt-Universität zu Berlin:
Prof. Dr. Jan-Hendrik Olbertz

Dekan der Mathematisch-Naturwissenschaftlichen Fakultät I:
Prof. Dr. Andreas Herrmann

Gutachter:
(i) Prof. Dr. Henning Riechert
(ii) Prof. Dr. Ted Masselink
(iii) Prof. Dr. Hans Lüth

eingereicht am: 13. März 2012
Tag der mündlichen Prüfung: 22. Juni 2012

„All of physics is either impossible or trivial.
It is impossible until you understand it,
and then it becomes trivial.“
Ernest Rutherford (1871- 1937)

Für meine Familie.

Abstract

This work is concerned with the realization and investigation of a light emitting diode (LED) structure within single GaN nanowires (NWs) and its integration with Si technology.
To this end first a general understanding of the GaN NW growth is given. This is followed by investigations of the influence which doping species, such as Mg and Si, have on the growth of the NWs. The experience gathered in these studies set the basis for the synthesis of nominal p-i-n and n-i-p junctions in GaN NWs. Investigations of these structures resulted in the technologically important insight, that p-type doping with Mg is achieved best if it is done in the later NW growth stage. This implies that it is beneficial for a NW LED to place the p-type segment on the NW top.
Another important component of an LED is the active zone where electron-hole recombination takes place. In the case of planar GaN LEDs, this is usually achieved by alloying Ga and In to form InGaN. In order to be able to control the growth under a variety of conditions, we investigate the growth of InGaN in the form of extended segments on top of GaN NWs, as well as multi quantum wells (MQWs) in GaN NWs. All the knowledge gained during these preliminary studies is harnessed to reach the overall goal: The realization of a GaN NW LED. Such structures are fabricated, investigated and processed into working LEDs.
Finally, a report on the efforts of integrating III-nitride NW LEDs and Si based metal-oxide-semiconductor field effect transistor (MOSFET) technology is given. This demonstrates the feasibility of the monolithic integration of both devices on the same wafer at the same time.

Keywords: GaN, MBE, LED, nanowires

Zusammenfassung

In dieser Arbeit wird die Machbarkeit der Herstellung von Leuchtdioden Strukturen (LEDs) in einzelnen GaN Nanodrähten (ND) und deren Integration mit herkömmlicher Si Technologie untersucht.
Hierzu wird zunächst ein generelles Verständnis des Wachstums von GaN ND erarbeitet und dargestellt. Es folgen Untersuchungen zum Einfluss von Dotierstoffen, wie z.B. Mg und Si, auf das Wachstum der ND. Dieses Wissen wird anschließend angewandt um Dotierübergänge in GaN ND herzustellen die nominell n-i-p bzw. p-i-n dotiert sind. Diese Untersuchung brachte die technologisch wichtige Erkenntnis, dass eine p-Dotierung mit Mg am besten erreicht werden kann wenn die ND bereits wohl entwickelt sind. Dies bedeutet, dass der obere Teil der ND LEDs aus p-Typ Material bestehen wird.
Eine weitere wichtige Komponente von LEDs ist die aktive Zone in der die Elektron-Loch-Rekombination stattfindet. Im Fall von planaren GaN LEDs wird diese durch Zugabe von In und die Formierung von InGaN hergestellt. Wir untersuchen das Wachstum von InGaN auf Si, GaN NDs und in Form von MQWs, um das Wachstum und insbesondere den In Gehalt unter vielen Bedingungen kontrollieren zu können.
Das gesamte Wissen der Voruntersuchungen wird kombiniert und für das Ziel dieser Arbeit nutzbar gemacht: Die Herstellung von GaN ND basierten LEDs. Diese Strukturen werden untersucht und zu einer funktionierenden LED weiter prozessiert.
Abschließend wird von den Anstrengungen zur Integration von III-Nitrid LEDs und Si basierter MOSFET Technologie berichtet. Es wird erstmalig erfolgreich die monolithische Integration dieser beiden Bauelemente und ihr gleichzeitiges Funktionieren gezeigt.

Stichworte: GaN, MBE, LED, Nanodrähte

Publications

F. Limbach, E. O. Schäfer-Nolte, R. Caterino, T. Gotschke, T. Stoica, E. Sutter, and R. Calarco, *Morphology and optical properties of Mg doped GaN nanowires in dependence of growth temperature*, J. Optoel. and Adva. Mat. **12**, 6, 1433 - 1441 (2010).

E. O. Schäfer-Nolte, T. Stoica, T. Gotschke, F. Limbach, E. Sutter, P. Sutter, and R. Calarco, *Highly polarized Raman scattering anisotropy in single GaN nanowires*, Appl. Phys. Lett. **96**, 091907 (2010).

E. O. Schäfer-Nolte, T. Stoica, T. Gotschke, F. Limbach, D. Grützmacher, E. Sutter, P. Sutter, and R. Calarco, *Enhanced light scattering of the forbidden longitudinal optical phonon mode studied by micro-Raman spectroscopy on single InN nanowires*, Nanotechnology **21**, 31, 315702, (2010).

F. Limbach, T. Gotschke, T. Stoica, R. Calarco, E. Sutter, J. Ciston, R. Cusco, L. Artus, S. Kremling, S. Hoefling, L. Worschech, and D. Gruetzmacher, *Structural and optical properties of InGaN-GaN nanowire heterostructures grown by molecular beam epitaxy*, J. Appl. Phys. **109**, 1, 014309, (2011).

T. Schumann, T. Gotschke, F. Limbach, T. Stoica, and R. Calarco, *Cathodoluminescence spectroscopy on selectively grown GaN nanowires*, Proc. SPIE 7939, 793903 (2011).

H. Riechert, O. Brandt, C. Cheze, V. Consonni, M. Knelangen, J. Lähnemann, F. Limbach, C. Pfüller, A. Trampert, M. Wölz and L. Geelhaar, *Nitride nanowire structures for LED applications*, Proc. SPIE 7954, 79540S-79540S-8 (2011).

T. Schumann, T. Gotschke, F. Limbach, T. Stoica and R. Calarco, *Selective-area catalyst-free MBE growth of GaN nanowires using a patterned oxide layer*, Nanotechnology **22**, 9, 095603, (2011).

T. Gotschke, E. O. Schäfer-Nolte, R. Caterino, F. Limbach, T. Stoica, E. Sutter, K. Jeganathan and R. Calarco, *Properties of uniform diameter InN nanowires obtained under Si doping*, Nanotechnology **22**, 12, 125704, (2011).

T. Gotschke, T. Schumann, F. Limbach, T. Stoica, and R. Calarco, *Influence of the adatom diffusion on selective growth of GaN nanowire regular arrays*, Appl. Phys. Lett. **98**, 10, 103102, (2011).

T. Stoica, A. Haab, D. Griesche, M. Mikulics, F. Limbach, T. Schumann, T. Gotschke, E. Sutter, R. Calarco, H. Hardtdegen,and D. Grützmacher, *Photoluminescence and Raman Scattering Studies of GaN Nanowires Obtained by Top-down and Bottom-up Approaches*, MRS Proc. **1408**, MRSF11-1408-BB20-14, (2012).

F. Limbach, R. Caterino, T. Gotschke, T. Stoica, R. Calarco, L. Geelhaar, and H. Riechert, *The influence of Mg doping on the nucleation of self-induced GaN nanowires*, AIP Advances **2**, 1, 012157, (2012).

F. Limbach, O. Brandt, T. Gotschke, T. Stoica, D. Grützmacher, C. Pfüller, F. Grosse, X. Kong, A. Trampert, S. Geburt, C. Ronning, R. Calarco, and H. Riechert, *Suppressed Mg*

incorporation in the initial stage of GaN nanowire growth by molecular beam epitaxy, submitted to Appl. Phys. Lett. (June 2012).

F. Limbach, C. Hauswald, J. Lähnemann, M. Wölz, O. Brandt, A. Trampert, M. Hanke, U. Jahn, R. Calarco, L. Geelhaar, and H. Riechert, *Current path in light emitting diodes based on nanowire ensembles*, in preparation.

F. Limbach, M. Erenburg, M. Wölz, J. Ledig, C. Hauswald, O. Brandt, R. Calarco, L. Geelhaar, H. Weihrich, A. Waag, and H. Riechert, *Single chip monolithic integration of a (In,Ga)N / GaN nanowire LED and a Si based MOSFET*, in preparation.

K. K. Sabelfeld, V. M. Kaganer, F. Limbach, P. Dogan, O. Brandt, L. Geelhaar, and H. Riechert, *Diffusional interaction in self-induced GaN nanowire growth*, in preparation.

Conference presentations

F. Limbach, T. Stoica , T. Gotschke, R. Caterino, G. Mussler, R. Meijers, E. Sutter, and R. Calarco, *III-N nanowires for solid-state lighting* (poster), Jara-Fit ScienceDays, Schleiden, Germany, Jun. 2009

F. Limbach, T. Stoica, T. Gotschke, R. Caterino, E. Sutter, and R. Calarco, *Growth and optical properties of p-doped GaN nanowires* (talk), GdR Nanofils et Nanotubes Semiconducteurs - Workshop 2009, Grenoble, France, Jul. 2009

F. Limbach, E O. Schäfer-Nolte, R. Caterino, T. Schumann, T. Gotschke, T. Stoica, E. Sutter, and R. Calarco, *GaN Nanowires: The effect of Mg doping* (talk), German MBE-Workshop, Bochum, Sep. 2009

F. Limbach, T. Stoica, R. Caterino, E. O. Schäfer-Nolte, E. Sutter, R. Meijers, and R. Calarco, *Influence of Mg-doping on growth and optical properties of GaN-nanowires* (poster), Nanowire-Growth-Workshop, Paris, Okt. 2009

F. Limbach, T. Gotschke, T. Stoica, E. Sutter, R. Cusco, L. Artus, R. Calarco, and D. Grützmacher, *Formation of a vertical and lateral heterostructure by InGaN overgrowth of GaN nanowires* (poster), 16th International Winterschool on New Developments in Solid State Physics: Low Dimensional Systems, Mauterndorf, Austria, Feb. 2010

F. Limbach, T. Stoica, R. Caterino, E. O. Schäfer-Nolte, T. Gotschke, E. Sutter, and R. Calarco, *Mg-doped GaN nanowires: Their optical and morphological properties* (poster), Spring Meeting of the Deutsche Physikalische Gesellschaft (DPG), Regensburg, Germany, Mar. 2010

F. Limbach, T. Gotschke, T. Stoica, R. Calarco, E. Sutter, R. Cusco, and L. Artus, *Vertical and lateral heterostructureof GaN/InGaN within nanowires* (talk), Spring Meeting of the Deutsche Physikalische Gesellschaft (DPG), Regensburg, Germany, Mar. 2010

F. Limbach, T. Gotschke, T. Stoica, C. Pfüller, O. Brandt, A. Trampert, S. Geburt, C. Ronning, and R. Calarco, *Effects of doping profile on the optoelectronic properties of GaN nanowires*

(talk), Spring Meeting of the Deutsche Physikalische Gesellschaft (DPG), Dresden, Germany, Mar. 2011

F. Limbach, T. Gotschke, R. Calarco, T. Stoica, E. Sutter, J. Ciston, R. Cusco, L. Artus, S. Kremling, S. Höfling, L. Worschech, and D. Grützmacher, *Ivestigation of an InGaN - GaN nanowire heterstructure* (poster), Spring Meeting of the Deutsche Physikalische Gesellschaft (DPG), Dresden, Germany, Mar. 2011

F. Limbach, C. Hauswald, M. Wölz, J. Lähnemann, O. Brandt, R. Calarco, L. Geelhaar, and H. Riechert, *Steps towards a GaN nanowire based LED* (talk), Deutscher MBE-Workshop 2011, Berlin, Germany, Okt. 2011

F. Limbach, C. Hauswald, M. Wölz, J. Lähnemann, T. Gotschke, C. Pfüller, O. Brandt, A. Trampert, R. Calarco, L. Geelhaar, and H. Riechert, *Growth, processing, and microluminescence of green (In,Ga)N/GaN nanowire light-emitting diodes on Si substrates* (talk), Scientific Advisory Board Meeting of PDI 2011, Berlin, Germany, Okt. 2011

F. Limbach, T. Gotschke, R. Calarco, T. Stoica, R. Caterino, C. Pfüller, O. Brandt, X. Kong, A. Trampert, L. Geelhaar, S. Geburt, C. Ronning, and H. Riechert *Effects of doping profile on the optoelectronic properties of GaN nanowires* (talk), Material Research Society (MRS) Fall meeting, Boston, MASS, USA, Nov. 2011

F. Limbach, C. Hauswald, M. Wölz, J. Lähnemann, O. Brandt, M. Ramsteiner, R. Calarco, L. Geelhaar, and H. Riechert, *GaN based nanowire LEDs on Si* (poster), HIOS Kick-off meeting, Berlin, Germany, Dec. 2011

Abbreviations

ABE	acceptor bound exciton
BEP	beam equivalent pressure
BSE	back scattered electron
CL	cathodoluminescence
CMOS	complementary metal-oxide-semiconductor
DBE	donor bound excition
DAP	donor-acceptor pair
DP	diffraction pattern
EBIC	electron beam induced current
EBL	electron-blocking-layer
EDS	energy dispersive x-ray spectra
EELS	electron energy loss spectroscopy
EL	electroluminescence
FE	free exciton
FFT	fast Fourier transform
Fig.	figure
FSNW	free standing nanowire
FWHM	full width at half maximum
FZ	Forschungszentrum
HRTEM	high resolution transmission electron microscope
HSQ	hydrogen silsesquioxane
ITO	indium-tin-oxide
L-D	length versus diameter
LED	light emitting diode
LO	longitudinal optic Raman mode
LS-QMS	line-of-sight quadrupole mass spectrometer
MBE	molecular beam epitaxy
MOCVD	metalorganic chemical vapor deposition
MOSFET	metal-oxide-semiconductor field effect transistor
MQW	multi quantum well
NBE	near-band-edge
ND	Nanodraht
NW	nanowire
PDI	Paul-Drude Institut für Festkörperelektronik
PL	photo luminescence
RDF	radial distribution function
RF	radio frequency
RHEED	reflection high-energy electron diffraction system
RIE	reactive ion etching
SAG	selective area growth
SE	secondary electron
SEM	scanning electron microscope

SF	stacking fault
SIMS	secondary ion mass spectrometry
STEM	scanning transmission electron microscope
TEM	transmission electron microscope
TO	transverse optic Raman mode
UHV	ultra high vacuum
UV	ultra violet
VLS	vapor-liquid-solid
VS	vapor-solid
QW	quantum well
XRD	x-ray diffraction
ZPL	zero phonon line

List of basic symbols

Symbol	Name	Unit
A	area	m^2
a	lattice parameter along the [11$\bar{2}$0] direction	Å
BEP_{Xy}	beam equivalent pressure of element Xy	mbar
c	lattice parameter along the [0001] direction	Å
c_{Xy}	doping concentration of element Xy	cm^{-3}
d	nanowire diameter	nm
$D_{n,p}$	electron / hole diffusion constant	$\frac{m^2}{s}$
D^*	critical nucleus diameter	m
e	elementary charge	C
E_F	Fermi energy	eV
E_g	bandgap energy	eV
$E_{C,V}$	Conduction band maximum / valence band minimum energy	eV
ΔG_{des}	free activation energy for desorption form a substrate	eV
ΔG_{sd}	free activation energy for surface diffusion on a substrate	eV
ΔG^*	critical Gibbs free energy	eV
h	Planck constant	Js
$\hbar$	Planck constant divided by 2π	Js
I	current	A
I_{LED}	current of a light emitting diode	A
I_S	saturation current of a diode	A
I_{SD}	source-dain current of a MOSFET	A
I^*	nucleation frequency	s^{-1}
k	carrier wave number	m^{-1}
k_B	Boltzmann's constant	$\frac{J}{K}$
l	nanowire length	nm
$m^*_{e,h}$	effective mass of electrons / holes in a semiconductor	kg
$N_{D,A}$	donor / acceptor concentration	cm^{-3}
n_i	intrinsic carrier concentration of a semiconductor	cm^{-3}
n_{ideal}	ideality factor	
n^*	concentration of nuclei with critical size D^*	cm^{-2}
ν	photon frequency	s^{-1}
$\eta_{extract}$	extraction efficiency	
η_{int}	internal quantum efficiency	
η_{WE}	wallplug efficiency	
P	optical power emitted info free space from a diode	W
P_{int}	optical power emitted from the active region of an LED	W
P_{RF}	radio frequency power of the N-plasma source	W
P_{sp}	spontaneous polarization	$C\,m^{-2}$
r	nanowire radius	nm
R_P	parallel resistance of a diode	Ω

Symbol	Name	Unit
R_S	series resistance of a diode	Ω
T	temperature	°C
T_S	substrate temperature	°C
T_{Xy}	effusion cell temperature of element Xy	°C
τ	time needed for the LS-QMS signal to drop to a certain level	s
τ_a	mean resistance time of an adsorbed atom	s
$\tau_{n,p}$	electron / hole minority-carrier lifetime	s
u	internal parameter of the wurtzite structure	
U	voltage	V
U_{SD}	source-drain bias	V
ν_0	desorption attempt frequency	s^{-1}
V_D	diffusion voltage	V
V_f	applied forward bias for operation	V
V_g	gate voltage applied to a MOSFET	V
V_{th}	threshold voltage	V
W_D	depletion region width	nm

Contents

1. Introduction

In the past four decades, micro and nanoelectronics have asserted themselves as established research fields ever trying to push the performance of integrated devices. The initial driving force for this development was the miniaturization of well-tested concepts and devices leading to Moore's Law.[1] This miniaturization or top-down approach of shrinking conventional devices is not viable much longer as dimensions of molecular proportions are reached. In this regime novel concepts, for structuring and designing devices need to be developed, as the costs involved in further miniaturization increase drastically with each step.[2,3] One possible way to overcome this problem is the bottom-up approach of device production.
Bottom-up approaches make use of self-assembly techniques driven in most cases by thermodynamics to form the desired objects.[4] With this method nanostructures such as Quantum Dots, Fullerenes, Carbon Nanotubes and semiconductor nanowires (NWs) can be produced at relatively low cost using laboratory size equipment.[4,5] Especially semiconducting NWs allow access to a wide range of opto-electronic and electronic devices.[6] The production as well as the control of morphology and composition of such NWs has been demonstrated for several material systems.[7–11]
The conventional way of producing semiconductor heterostructures is the deposition of films. Yet, due to the lattice mismatch between the used materials, strain and defects may be introduced.[12] These deviations from the perfect crystalinity cause in turn a deterioration of the optoelectronic properties. Defects for example can be the cause for non radiative recombinations in light emitting diodes (LEDs).[13] The small footprint of the NWs on the substrate is beneficial for relaxing issues related to the structural mismatch between substrate and epitaxial layer. Strain can be relaxed within the NW at the heterointerface by contraction or expansion due to the limited diameter.[14–16] Extended defects develop only at the interface with the substrate and bend towards the nearest surface instead of propagating along the crystal.[17] These properties might even allow integration in standard silicon based technology as NWs can be grown as single nano-crystals with high crystalline perfection on Si(111) and (100), as well as on amorphous SiO_2 substrates.[7,16,18,19] Furthermore, NWs might prove to have an enhanced out-coupling efficiency of light compared with planar layers.[20,21]
In the past two decades the Al-Ga-In-N material system, also called group III-nitrides, has revolutionized solid state light emitters[22] and has impacted photovoltaics as well as high-power and high-temperature electronics.[23,24] The InGaN ternary system offers band gap tunability covering the whole visible spectral range.[25–27] Moreover, III-N nanostructures and NWs, in particular, may provide a pathway to integrate optoelectronic devices and standard Si technology.[28]

It is the aim of this thesis to describe the control of GaN/InGaN NW growth, the creation of an LED structure within such NWs and their integration with standard Si technology. Each chapter will focus on a particular component needed for the fabrication of an LED prototype.
In chapter 3 the basics of GaN NW growth are investigated and discussed using either

data generated for this thesis or published by other authors during the past years.
Doping of the semiconductor material is essential for creating an LED and will be discussed in chapter 4. For p-type doping of GaN Mg is frequently used.[28] The implications of a Mg supply to the NW growth is presented in section 4.1. Likewise the effect of Si on the growth of NWs, which acts as a donor in GaN,[28] is investigated in section 4.2. The chapter on doped GaN NWs also includes the growth of nominal p-i-n junctions within GaN NWs using both doping species (section 4.3).
Chapter 5 focuses on the incorporation of In into the GaN matrix which allows the control of the bandgap in the active region of the LED. Direct growth of InGaN NWs on Si, growth of InGaN segments on GaN NW and quantum well (QW) structures within GaN NWs are discussed.
Finally, chapter 6 describes the combination of the insights gained from the growth analysis discussed so far, in order to synthesize an LED structure within single NWs. Furthermore the processing of these wires into a working device and its characteristics are presented. The chapter ends with the discussion of an experiment designed to integrate the light generation through III-N NW LEDs with the well established technology of Si based metal-oxide-semiconductor field effect transistors (MOSFETs) on one and the same wafer.
The last chapter is dedicated to the summary of the results obtained and an outlook describing possible future experiments and challenges which still need to be overcome.

2. Basic information on materials, devices and concepts

This chapter provides the background information needed for the understanding and the classification of the experimental results described in chapters 3 to 6 in light of the knowledge to date and the concepts used in their interpretation. Section 2.1 focuses on the properties of the group-III-nitride material system. The basics of an LED are presented in section 2.2 followed by a brief introduction into the growth of nanowires in general in section 2.3. This chapter ends with section 2.4 describing the main aspects of the experimental technique used for the syntesis of the samples discussed through out the remainder of the thesis.

2.1. The III-nitride material system

This section will give a brief overview of the Al-Ga-In-N material system. GaN along with the ternary and quaternary compounds using Al and In is considered to be one of the most important semiconductors besides Si. It is found in many applications which is a result of the excellent electrical and optical properties of the nitrides. As native substrate for III-nitrides are only available in very small sizes and at extremely high cost, heteroepitaxy is a basic necessity in the syntesis of these materials. Therefore many of the parameters discussed in this section originate from measurements of thin films and are subject to the influence of the used substrate.[28]
While III-nitrides can exist in wurtzite, zinc blende and rocksalt crystalline structures only wurtzite will be discussed here. It is the thermodynamically most stable configuration and the one found in all the NWs that are subject of this thesis. The calculated and experimentally observed structural parameters for GaN, AlN and InN are summarized in table 2.1. Many GaN-based devices employ heterostructure interfaces with ternary III-nitride alloys. In particular InGaN is of importance for LEDs and lasers. Through alloying the lattice constants gradually change from those of GaN to InN.[29]

$$a_{\mathrm{In}_x\mathrm{Ga}_{1-x}\mathrm{N}} = 3.1986\,\text{Å} + 0.3862x\,\text{Å} \quad \text{and} \quad c_{\mathrm{In}_x\mathrm{Ga}_{1-x}\mathrm{N}} = 5.2262\,\text{Å} + 0.574x\,\text{Å}. \tag{2.1}$$

The use of these ternary alloys originates in most cases from the desire to shape the bandgap of the semiconductor material and therefore its luminescence properties. Also

	GaN		AlN		InN	
	Ideal	Exp.	Ideal	Exp.	Ideal	Exp.
a [Å]	3.199	3.199	3.110	3.110	3.585	3.585
c/a	1.633	1.634	1.633	1.606	1.633	1.618

Table 2.1: Calculated and experimentally determined structural parameters of GaN, AlN and InN.[28]

the bandgap energy of InGaN changes gradually from that of GaN (3.4 eV) to the one of InN (0.7 eV) depending on composition. $E_g^{In_xGa_{1-x}N}$ at 300 K is given by:[30]

$$E_g^{In_xGa_{1-x}N} = (0.7x + 3.4(1-x) - 1.43x(1-x))\text{eV}. \tag{2.2}$$

The wurtzite structure of the III-nitrides lacks a center of inversion symmetry which is the cause for a nonzero spontaneous polarization and the possible existence of piezoelectric polarization due to strain along the [0001] direction.[29,31,32] This is particularly relevant in the case of heterointerfaces between two nitride semiconductors with varying electronegativity of the metal atoms. For a detailed description see Vanderbilt[33] and Resta *et al.*[34]. The ball-and-stick diagram presented in Fig. 2.1 shows the two polarities for GaN.

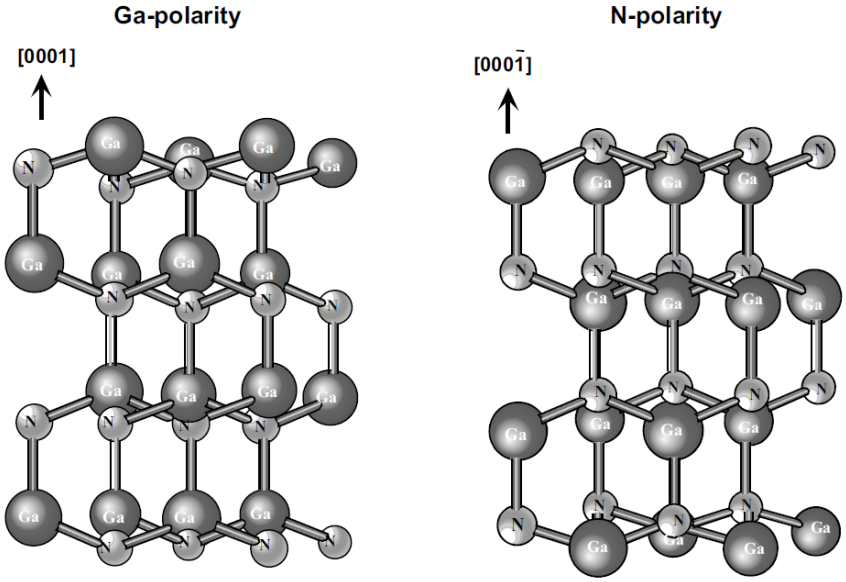

Figure 2.1: Ball-and-stick figure of the two polarities of wurtzite GaN.[28]

The values for the spontaneous polarization, deduced from a 32-atom supercell calculation by Bernardini,[35] are given in table 2.2. The value of P_{sp} for InGaN can be calculated according to Bernardini and Fiorentini[36,37] via:

$$P_{sp}^{In_xGa_{1-x}N} = -0.042x - 0.034(1-x) + 0.0378x(1-x). \tag{2.3}$$

For an InGaN QW (thickness 20 nm and $\approx$ 15% In content) in between two GaN layers these polarization effects results in an internal field on the order of $\frac{\text{MV}}{\text{cm}}$.[38,39] Such a strong field changes the shape of the QW from a rectangular shape to a triangular one. This results in a red shift (Stark shift) of the transition energy observed when electrons

	AlN	GaN	InN
P_{sp}	-0.0897	-0.0336	-0.0434

Table 2.2: Spontaneous polarization for III-nitrides determined by 32-atom supercell calculation by Bernardini.[35]

Energy position [eV]	Nomenclature	Doping
3.478	free exciton (FE)	Undoped
3.471	donor bound exciton (DBE)	O, Si, undoped
3.42	stacking fault induced (SF)	undoped [49,50]
3.466	acceptor bound exciton (ABE)	Mg
3.1 - 3.26	electron to acceptor (e-A) or / and DAP	Mg

Table 2.3: List of the luminescence lines and bands at low temperatures (4 K) in GaN which are of importance for this thesis. Except for the value of the stacking fault induced luminescence all other entries were taken from Reshchikov *et al.* [48].

and holes recombine in such a QW.[28] Apart from this shift in transition energy, the electric field in a QW also causes a spatial separation of electrons and holes. This in turn leads to a smaller spatial overlap of the two wave functions and therefore decreases the recombination probability. The effect is referred to as quantum confined stark effect.[28,40]
Doping is an important topic for any semiconductor as many device functionalities relay on the specific doping profile. Growing GaN without any intentional dopants leads to n-type material. The carrier density can be significantly increased by supplying additional doping atoms which act as donors in the GaN matrix. Si substitutional on a Ga site is the most efficient and most commonly used element.[41,42] By incorporating a Si atom on a Ga site an energy level is created 30 meV below the conduction band.[43] The solubility of Si in GaN is in the order of 10^{20} cm^{-3}. Several different elements can act as reasonably shallow acceptors when placed on a Ga site,[44] yet Mg is the one most commonly used. The acceptor level for a Mg atom on a Ga site is at around 220 meV above the valence band.[45,46] In GaN:Mg grown by metal-organic-vapor-phase-epitaxy a free hole concentration of 10^{18} cm^{-3} was found for Mg concentrations of $3 \cdot 10^{19}$ cm^{-3}.[47]
Both cathodoluminescence (CL) and photo luminescence (PL) measurements can reveal the presence of a doping atom. Table 2.3 summarizes the most relevant transitions for this thesis, their energetic position in acquired spectra and their origin. For further details on defect luminescence in GaN the reader is referred to Reshchikov *et al.*[48].
Donor bound exciton (DBE) and free exciton (FE) transitions can be observed in almost any GaN NW sample of reasonable quality. The absence of an intense emission caused by the presence of stacking faults (SFs) is an indication that coalescence of NWs is limited.[50] In n-type GaN the donor-acceptor pair (DAP) transition can be used as a measure of active Mg. Due to the high background level of donors it is directly proportional to the number of acceptors.[28]
In the past, much attention has been payed to metal-semiconductor interfaces.[51,52] For GaN, as for many wide-bandgap semiconductors, achieving good ohmic contacts is rather difficult. Nevertheless some viable options have come up. For the NW-LED as it is presented in chapter 6 only p-type GaN needs to be contacted, as the n-type base of the NWs will be contacted via a heterojunction with n-type Si. Two very widely used methods to contact p-type GaN are Ni/Au and indium-tin-oxide (ITO) contacts. Ni/Au contacts are easy to produce through electron beam evaporation but absorb light. ITO contacts on the other hand need some expertise as one needs both, good electrical contact with p-GaN and high transparency. For this reason Ni/Au contacts were used as they required a minimum of process optimization.[28]
InGaN/GaN based blue and ultra violet (UV) LEDs are now commercially available. In the spectral range between 550 nm and 590 nm, they are not competitive, yet. This re-

gion is known as "the green gap" in which the efficiency of InGaN-based LEDs decreases significantly.[53] This efficiency loss, also called "droop", is at present under investigation and may have several possible origins: phonon or defect-assisted Auger recombination,[54,55] tunneling leakage of carriers to defects[56] or carrier overflow.[57–59]
In addition, InGaN/GaN LEDs with MQWs having an In composition greater than 20% can suffer from the formation of defects that lead to low radiative efficiency.[60] Furthermore, the incorporation of In atoms into InGaN is limited. This is caused by a large lattice mismatch between InGaN and GaN.[61] To circumvent the problems inherent to the InGaN MQW approaches, alternate active layers such as InGaN NWs[62–67] and quantum dot structures[22,60,68] have been suggested as light emitters in the green gap spectral range.[53] The pursuit of one of these proposed alternatives is the goal of this thesis. A full LED structure within a GaN NW might overcome the "green gap" problematics.

2.2. Light emitting diodes

The first report of an LED by H. J. Round was published in 1907. He discovered electro luminescence (EL) from SiC crystallites which emitted a yellow glow at voltages above 10 V and had rectifying qualities.[69] Further investigation of this luminescence effect in SiC rectifiers led to the conclusion that this emission was not based on heat glow (incandescence).[70] Before the 1950s, investigation of LEDs was based on devices made from SiC or II-VI semiconductors.[13,71] This changed with the postulation and demonstration of III-V compound semiconductors by H. Welker.[72,73] These new man-made materials proved to be optically very active due to their direct bandgap. First infrared LEDs and lasers based on GaAs and GaAsP were reported in 1962.[74–79] Also around this time research on GaN as a candidate for blue EL was initiated and the first commercial LED based on GaAs was offered by the Texas Instruments Corporation.[80]
Even though the EL from GaN was reported by a team at Radio Corporation of America (RCA) quite early,[81,82] the lack of efficient p-type doping of GaN was a problem. The first true p-type GaN was demonstrated only in 1989 by using activated Mg acceptors.[83] Soon after the first p-n junction and GaN based LEDs were demonstrated.[13] They were followed by LEDs of up to 10% efficiency[84] and even an electrically pumped blue laser operated at room temperature.[85] The interest in the InGaN material system remains, as it is suited to be an active medium for white-light emitting LEDs.[27]

Electrical properties

In this subsection, the electrical characteristics of an abrupt p-n junction with an acceptor concentration N_A and donor concentration N_D will be described according to Schubert.[13] For the sake of brevity no detailed derivation is presented. All dopants ($N_{D,A}$) are assumed to be ionized which results in the free electron (n) and hole (p) concentrations:

$$n = N_D \qquad p = N_A. \tag{2.4}$$

In the vicinity of the p-n junction the so called depletion region forms due to diffusion of electrons to the p-type and holes to the n-type material. Their recombination with the respective majority charge carriers leaves only the charges of the ionized donors and acceptors in the depletion region which form a space charge region. These charges produce

a potential called the diffusion voltage V_D

$$V_D = \frac{k_B T}{e} \ln\left(\frac{N_A N_D}{n_i^2}\right) \tag{2.5}$$

where n_i is the intrinsic carrier concentration of the semiconductor, k_B is Boltzmann's constant, T is the temperature and e is the elementary charge. The diffusion voltage represents the barrier that carriers must overcome in order to reach the opposite side of the junction (see Fig. 2.2).

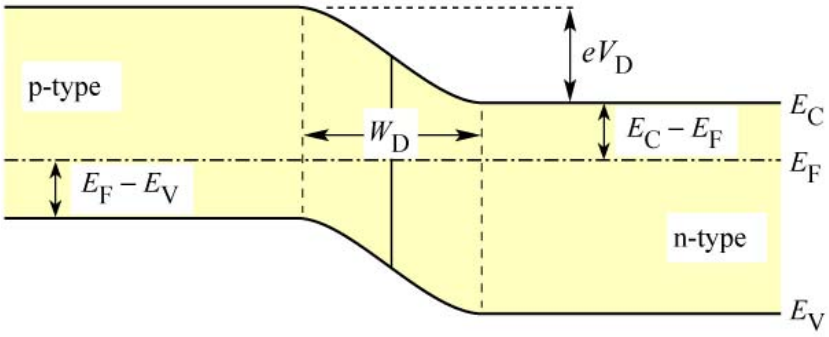

Figure 2.2: Band diagram of a p-n junction under zero bias.[13]

When applying a bias the voltage is going to drop across the depletion region. Under forward bias, electrons and holes are injected from their native region into the region with the opposite majority carriers, where they recombine and thereby emit a photon. The formula describing the current-voltage (I-U) characteristic of a p-n junction is the so called Shockley equation. It describes the current I through a diode with a cross-sectional area A:

$$I = eA\left(\sqrt{\frac{D_p}{\tau_p}}\frac{n_i^2}{N_D} + \sqrt{\frac{D_n}{\tau_n}}\frac{n_i^2}{N_A}\right) \cdot \left(\exp\left(\frac{eU}{k_B T}\right) - 1\right) \tag{2.6}$$

where $D_{n,p}$ and $\tau_{n,p}$ are the electron and hole diffusion constants and carrier lifetimes, respectively.
Under reverse bias the diode current saturates. This saturation current I_S is given by the factor preceding the exponential function:

$$I_S = eA\left(\sqrt{\frac{D_p}{\tau_p}}\frac{n_i^2}{N_D} + \sqrt{\frac{D_n}{\tau_n}}\frac{n_i^2}{N_A}\right). \tag{2.7}$$

Under typical forward bias conditions $U \gg \frac{k_B T}{e}$ is true and thus:

$$\left(\exp\left(\frac{eU}{k_B T}\right) - 1\right) \approx \exp\left(\frac{eU}{k_B T}\right). \tag{2.8}$$

Therefore the Shockley equation can be rewritten using equation (2.5), as

$$I = eA\left(\sqrt{\frac{D_p}{\tau_p}}N_A + \sqrt{\frac{D_n}{\tau_n}}N_D\right) \cdot \exp\left(\frac{e(U - V_D)}{k_B T}\right). \tag{2.9}$$

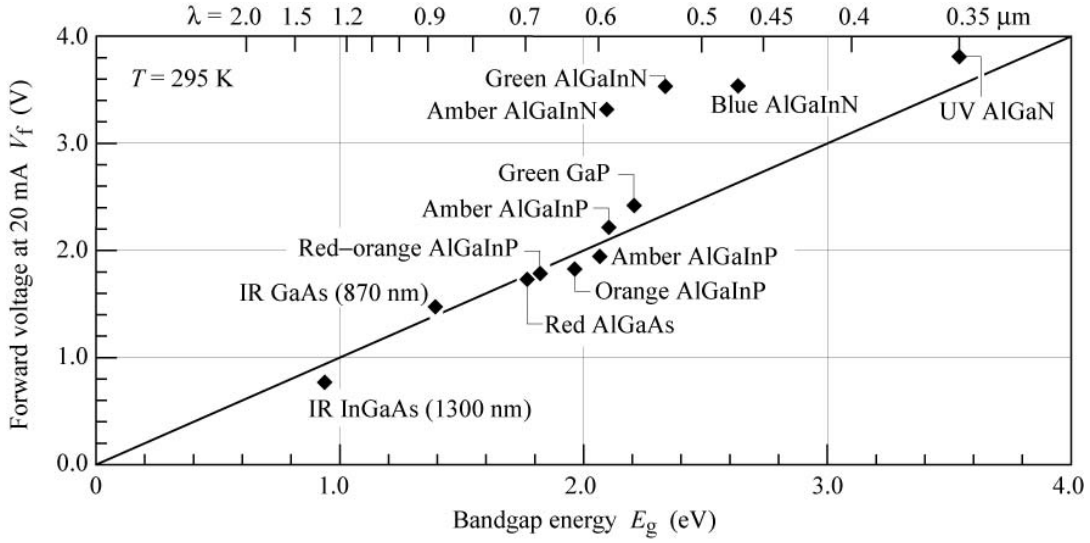

Figure 2.3: LED forward voltage versus bandgap energy for LEDs made from different materials.[13]

The exponent of the exponential function illustrates that the current strongly increases as the applied bias approaches V_D. This voltage is also called threshold voltage V_{th} and is given by $V_{th} \approx V_D$.
The following summation can be extracted from Fig. 2.2:

$$eV_D + (E_F - E_V) + (E_C - E_F) - E_g = 0, \tag{2.10}$$

with E_F, E_C, E_V and E_g denoting the Fermi energy level, the conduction band minimum energy, the valence band maximum energy and the bandgap energy, respectively. In highly doped semiconductors diodes the following approximations are valid for the n- and p-type region, respectively:

$$(E_C - E_F) \ll E_g \qquad (E_F - E_V) \ll E_g. \tag{2.11}$$

Thus the second and third term in equation (2.10) can be neglected and the threshold and diffusion voltages can be approximated with:

$$V_{th} = V_D \approx \frac{E_g}{e}. \tag{2.12}$$

This relationship holds true for most semiconductor LEDs with the exception of the III-nitrides (see Fig. 2.3). This is due to several reasons. Large bandgap discontinuities occur in the nitride material system, the contact technology is not mature yet, p-type conductivity is low and/or a parasitic voltage drop can occur in n-type buffer layers. Each of these factors leads to additional voltage drops increasing the operation voltage V_f above $\frac{E_g}{e}$.
The Shockley equation represents the theoretically expected current-voltage characteristic of an ideal p-n junction. In order to accommodate for characteristics, measured in

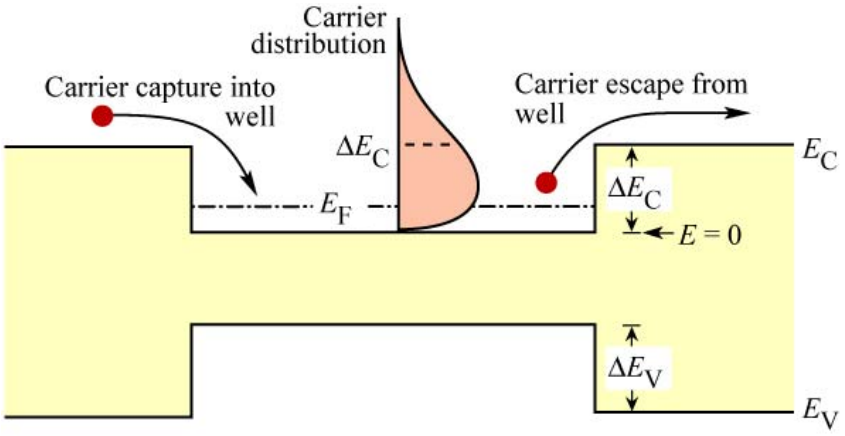

Figure 2.4: Diagram of a double heterostructure with the energy distribution of the captured carriers.[13]

experiments, the so called ideality factor n_{ideal} is introduced into the equation:

$$I = I_S \exp\left(\frac{eU}{n_{ideal} k_B T}\right). \tag{2.13}$$

For a perfect diode the value of n_{ideal} is one. Measured values of diodes range from $n_{ideal} = 1.1$ to values as high as $n_{ideal} = 7$ for some GaN/InGaN diodes. In addition, the diodes performance can suffer from additional parasitic resistances. Contact resistances or resistance of the neutral regions can cause a series resistance R_S. Current carrying channels that bypass the p-n junction will result in a shunt with a parallel resistance R_P. Accounting for these resistances results in a modification of equation (2.13):

$$I = I_S \cdot \exp\left(\frac{e(U - IR_S)}{n_{ideal} k_B T}\right) + \frac{(U - IR_S)}{R_p}. \tag{2.14}$$

The parallel resistance R_P can be evaluated in the reverse bias regime:

$$R_P \approx \left.\frac{dU}{dI}\right|_{\text{reverse bias}}. \tag{2.15}$$

For diodes that exhibit a high value in R_P equation 2.14 can be approximated to:

$$I = I_S \cdot \exp\left(\frac{e(U - IR_S)}{n_{ideal} k_B T}\right). \tag{2.16}$$

Solving and differentiating for U with respect to I yields:

$$\frac{dU}{dI} = R_S + \frac{n_{ideal} k_B T}{e} \cdot \frac{1}{I}. \tag{2.17}$$

Multiplying by the current I enables the identification of R_S and n_{ideal} by determining the slope and y-axis intercept of a $(I \cdot dU/dI)$-versus-I plot, respectively.

Double heterostructures are employed in LEDs in order to enhance the recombination rate of electrons and holes in a p-n-junction through their spatial confinement. In such designs the area of recombination (active region) is made of a smaller bandgap semicon-

ductor that is sandwiched on both sides by a semiconductor with a larger bandgap, the confinement regions. The material surrounding the active region acts as a barrier for captured charge carriers. The volume of the active region is defined by the thickness of the small-bandgap material which acts as a well (see Fig. 2.4). This in turn causes a much higher concentration of electrons and holes in the recombination zone and therefore enhances the recombination rate significantly.
A significant loss mechanism is the overflow of carriers from the active region into the confinement regions. This effect occurs at high injection currents. The active region is flooded with carries resulting in a rising Fermi energy level. This can lead to a rise up to the barrier height. A further increase in the injection current will not result in a higher charge carrier density in the active region and therefore the optical intensity saturates. The problem is inherent to single-QW and quantum-dot structures due to their small volume. This can be avoided by enlarging the active region of the double heterostructure or by creating several QWs to form a MQW active region.[86]
Even though the barrier height is significant (typically several hundred meV) the Fermi distribution nature of the captured charge carriers allows some of them to escape (see Fig. 2.4). Typically the leakage current caused by electrons is the dominant factor due to the large diffusion constant of the electrons compared with that of the holes. In order to reduce the leakage, electron-blocking-layers (EBLs) are employed in many LED structures. An EBL is an interlayer with a large bandgap energy E_g located between the active region and the p-type confinement region and is typically also p-doped (see Fig. 2.5). This results in an increased barrier for the electrons on the p-type confinement side while at the same time the barrier for holes to enter the active region is virtually zero.

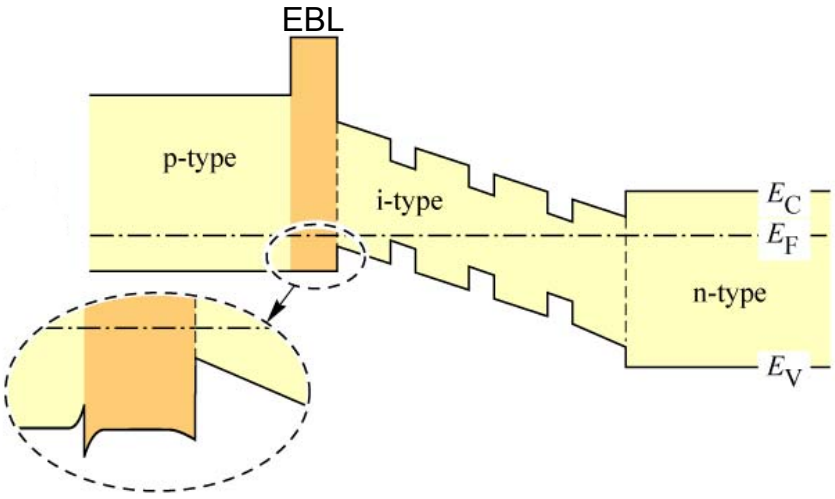

Figure 2.5: Diagram of a MQW heterostructure with an EBL.[13]

Optical properties

In this subsection, the elementary optical properties of an LED are discussed according to Schubert.[13] The scope of this discussion will be very limited and focuses only on those aspects relevant for LEDs in general.
The basic physical principle underlying the luminescence of LEDs is the spontaneous annihilation of electron-hole pairs and the simultaneous emission of a photon. Fig. 2.6 illustrates the recombination of an electron-hole pair. Electrons and holes are assumed to

have parabolic energy dispersion relations described by

$$E = E_{C,V} \pm \frac{\hbar^2 k^2}{2m^*_{e,h}} \tag{2.18}$$

with the effective mass of electrons or holes respectively $m^*_{e,h}$, $\hbar$ being Planck's constant divided by 2π and the carrier wave number k. Energy conservation requires that the

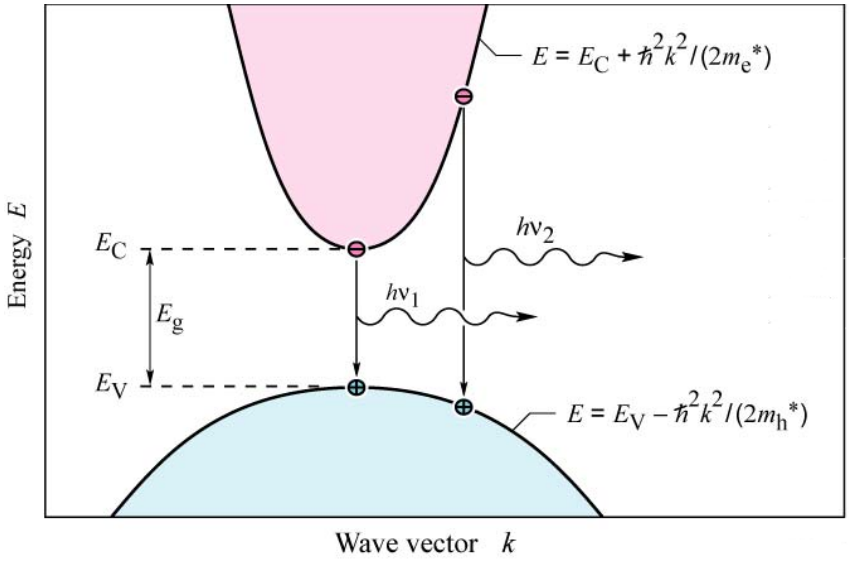

Figure 2.6: Energy dispersion of electrons and holes in a semiconductor showing electron-hole recombination and emission of a photon.[13]

energy of the photon generated in the annihilation process is given by the difference between electron energy E_e and hole energy E_h:

$$h\nu = E_e - E_h \approx E_g. \tag{2.19}$$

The photon energy is approximately equal to E_g if $k_B T \ll E_g$ is true. Therefore the desired wavelength of emission from an LED can be tuned by choosing an appropriate semiconductor with the desired bandgap. This makes the In-Ga-N material system very interesting for visible light emission as its bandgaps can span the entire visible spectrum.[13,28]
LEDs are deemed to be efficient light sources since in an ideal LED a photon is created for every electron that is injected into the active region. Yet, in practice this is not the case and a measure for the efficiency of an LED is needed. Typically, the internal quantum efficiency η_{int} is used to describe the efficiency with which photons are created in the active region. It is defined as

$$\eta_{int} = \frac{P_{int} e}{I h\nu} \tag{2.20}$$

with the injection current I and the optical power P_{int} emitted from the active region of an LED. Not all photons created in the active region escape the LED. The extraction efficiency may be lower due to reabsorbtion or total internal reflection of the light, it is defined as

$$\eta_{extract} = \frac{P}{P_{int}} \tag{2.21}$$

with the optical power P emitted into free space. The product of these two efficiencies is called the external quantum efficiency. Finally, the most important efficiency for LEDs is the wall-plug efficiency which is the ratio of extracted light power and injected electrical power, defined as:

$$\eta_{WE} = \frac{P}{IU}. \tag{2.22}$$

State-of-the-art LED system designs of efficacies greater than 100 lumens-per-watt are routinely achieved by leading lighting manufacturers today. This corresponds to a wall-plug efficiency of about $\eta_{WE} = 0.148$ or 14.8%.[87]

2.3. Nanowires

The research field of nanotechnology is rapidly expanding and has gained much attention during the last decade. Much of this excitement is due to the fact that quantization effects can be observed in nano-size structures. These appear when the sizes of the structures are comparable with the wavelength of the charge carriers. These are thus confined in one, two or even all three spatial dimensions. An example of confinement in one dimension are the two dimensional electron gases that can form in semiconductor heterostructures such as an AlGaN/GaN interface.[28] NWs are an example of structures confined in two dimensions, while quantumdots are zero dimensional objects, in which charge carriers are confined in all three spatial dimensions.

NWs have the potential to revolutionize broad areas of nanotechnology[88]. They represent the smallest structures that can efficiently transport charge carriers and thus are suited to move carriers in integrated nano-systems. At the same time, NWs can exhibit device functions themselves. In this regard especially semiconductor NWs are promising.[89,90]

In general there are two approaches to produce NWs. One is the "*Top-Down*" approach which starts with a three dimensional crystals from which wires are defined, for example, by etching.[91] The other is the "*Bottom-Up*" approach that builds the wires from single atoms or molecules.

The "*Top-Down*" fabrication uses as starting material a thin film which may contain grain boundaries or other structural defects. Therefore, the crystal quality of the wires can only be better than that of the film, if defects are removed preferentially. Another disadvantage of this method is, that the wires might be contaminated due to the use of chemicals. In the case of reactive ion etching (RIE) additional radiation induced defect can occur.[92] For these reasons the wires, being discussed in this scope, were produced by a "*Bottom-Up*" process. There are two important categories of this process. One is the "*Vapor-Liquid-Solid*" (VLS) growth which uses liquid catalyst droplets. The catalyst absorbs the material for the NW growth from the gas phase. A supersaturated liquid is formed and solid material is precipitated below the droplet.[93,94] This technique has the principal disadvantage that the catalyst may contaminate the NW.[95] The other possible technique is the "*Vapor-Solid*" (VS) growth method, during which the wires form by self organization from the gas phase. The wires used in this scope were grown by employing this second method.

There is a wide range of possible applications for NWs in technology. Since semiconductor NWs are the subject of this thesis the examples of applications are limited to applications that have been published for other semiconducting NWs.

Nanoelectronics is a field in which the low dimensionality of NWs can be employed to

develop devices that probe fundamental physical properties and aid in developing quantum information technology.[96] A principle device for this technology is a quantum dot whose charge and spin state can be controlled by a gate voltage. In NWs even double quantum dots with tunable coupling via gates have been realized in various material systems.[90,97,98]
Another set of devices aims to achieve higher integration densities of basic logic elements than those achievable with current technology. For this purpose, such elements need to be assembled and tested. Examples for such basic elements are a NOR-gate,[99] a NW field effect transistor[100] or a p-n junction.[101]
Due to their large aspect ratios, the physical properties of NWs are, to a great extent, influenced by their surfaces. This property opens up the possibility of employing NWs as sensors. When exposed to a substance that influences their surface, properties such as the resistance of the wire might change drastically even if the concentrations of these substances are in the range of a few parts per million (ppm).[102] The nano-scale size of these devices allows a drastic shrinkage of chemical detectors.[103] NWs can be assembled into a regular array and then selectively functionalized, in order to sense chemicals when introduced into a micro-fluidic channel.[104]
Nanophotonics address the broad spectrum of optics on the nanometer scale where spatial dimensions are well below the wavelength of light. In this regime, NWs can be employed in various manners such as waveguides,[105] point-like light emitters[89] and even single photon emitters.[106]

2.4. Molecular beam epitaxy for nanowire growth

While in general the growth of NWs is dominated by the VLS mechanism, the synthesis of the GaN NWs discussed in this scope was achieved via the VS growth mode. Metalorganic chemical vapor deposition (MOCVD) and molecular beam epitaxy (MBE) are both used for the VLS approach using a metal catalyst droplet, yet the use of MOCVD reactors is dominant for this growth method.[107] On the other hand MBE dominates in the field of VS growth of GaN NWs were the MOCVD approach has had little success up to now.[66,108] This section will give an overview of the hardware used and the growth mechanism of the GaN NWs synthesised in the VS growth mode through MBE. In particular nucleation, steady state growth and shadowing aspects will be discussed. This will be done through the review of recent publications which set the stage for the investigations conducted within this thesis.

Molecular beam epitaxy

MBE is a method that allows the synthesis of very clean material through the deposition of material on a heated substrate inside a ultra high vacuum (UHV) chamber, using atomic or molecular directed beams. Usually rather slow growth rates compared to MOCVD are employed which enables a high degree of controllability. The details of MBE will not be discussed in this thesis as it could not give the full description that is best found in textbooks.[109,110]
The machines used for the synthesis of the GaN NWs discussed in this thesis were: A custom designed system manufactured by "Createc" at the Paul-Drude-Institut in Berlin and a VG80M manufactured by "VG" at the Forschungszentrum (FZ) Jülich. Both sys-

tems have a base pressure of below 10^{-9} mbar in standby and 10^{-5} mbar in operation. The low base pressure ensures that the incorporation of unwanted elements is limited to a minimum. The high pressure of 10^{-5} mbar during operation is caused by the N source. In both cases an radio frequency (RF) plasma source that creates a beam of atomic N is used. Nevertheless, the mean free path of 10 m of an atom or molecule is well above the chamber dimensions. In addition to the N sources the chambers are equipped with Knudsen effusion cells for Ga, In, Al, Mg and Si. The substrate is located about 30 cm away from the sources and heated through the radiation of a filament near the backside of the substrate.
Furthermore, the system at the Paul-Drude-Institut features a reflection high-energy electron diffraction system (RHEED) and a line-of-sight quadrupole mass spectrometer (LS-QMS) for *in-situ* analysis. RHEED, unlike the LS-QMS, is a rather common *in-situ* method used in MBE systems. For a detailed description the reader is referred to Ichimiya.[111] The working principle of the LS-QMS will be discussed below. Both systems used are equipped with a pyrometer facing the substrate for the *in-situ* temperature calibration. Detail descriptions of the two systems can be found in the PhD. thesis of Dr. Ralf Meijers[112] and Dr. Tobias Gotschke.[113]
The LS-QMS technique has demonstrated great potential for enhancing the understanding of the growth and surface kinetic processes of GaN. Obtained data, for example, helped in determining a growth mode diagram for GaN[114] and enabled a precise understanding of the GaN decomposition processes.[115] This technique is thus very promising for providing information concerning the NW nucleation and growth.[116–118] The LS-QMS method relies on the measurement of the desorbing atomic and molecular species during growth. By a precise calibration during the full desorption of a known incident flux of the same species on a substrate brought to high temperature, the LS-QMS signal of the impinging flux is obtained and can be converted into growth units.[117]
Fig. 2.7 illustrates the geometry of the LS-QMS device. By restricting the acceptance angle through the use of an aperture plate, local mass spectrometry of atoms or molecules desorbing from the substrate can be carried out. The mass to charge ratio determines which species are enabled to pass along the four electrode rods all the way to the Farraday Cup used for current detection. This detected current is converted into an equivalent partial pressure. Using the aperture minimizes the background signal related to the desorption from the manipulator and the chamber walls.[117] The LS-QMS used allows the detection of ions in a mass range of 1 to 300 atomic mass units (amu) with a resolution better than 0.5 amu at 10% peak height. This device is equipped with a Continuous Dynode Electron Multiplier in order to detect partial pressures down to $5{\cdot}10^{-14}$ mbar with a maximum time resolution of 2 sec.[117] The isotopes monitored for this thesis are ^{69}Ga and ^{115}In, Mg could not be observed due to the high background pressure of N with a similar mass to charge ratio.

GaN nanowire nucleation

Nucleation is the initial stage of the NW growth and ranges from the opening of the cell shutters until NWs with an aspect ratio on the order of one have developed. It needs to be viewed as a separate issue to the NW growth itself. This section introduces some basic nucleation theory and concludes with the description of the NW nucleation phase.
Nucleation itself is a rather old topic and already quite well discussed by Maissel and Glang (1970)[119] and Anderson (1978)[120] on which the following discussion is based.

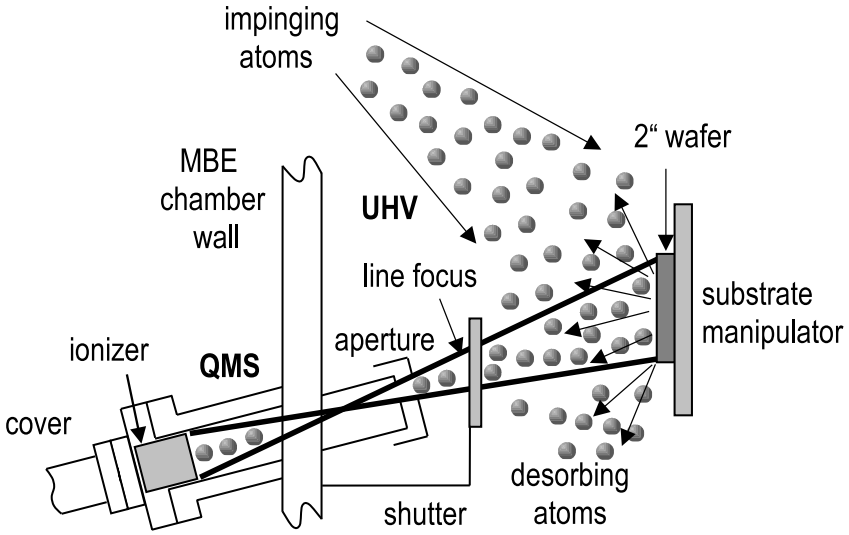

Figure 2.7: Schematic of a LS-QMS in operation for the monitoring of desorbing atoms. An appropriate aperture plate limits the angle of acceptance to the size of the sample.[117]

The initial step, in all theories on nucleation, is the impingement of vapor atoms or molecules on a substrate. After impingement, the vapor atoms can either adsorb and stick permanently to the substrate (substrate temperature T_S very low), they can adsorb and reevaporate in a finite time, or they can fail to bond to the substrate at all and directly disappear into the vacuum. For nucleation, only those that adsorb on the substrate, be it for a finite time or for good, are of interest. Once the adsorbed vapor atoms have reached a particular number density, a steady state is obtained, in which the flux of reevaporating atoms equals the impinging flux. The mean residence time τ_a of an adsorbed atom before reevaporation is given by:

$$\tau_a = \frac{1}{\nu_0} \exp\left(\frac{\Delta G_{des}}{k_B T_S}\right). \tag{2.23}$$

With ν_0 being the desorption attempt frequency and ΔG_{des} being the free activation energy for desorption form a substrate. Nucleation can take place if the number density of atoms at any given time is high enough for aggregates to form. The capillarity model[121,122] predicts that the free energy of formation of a condensed aggregate goes through a maximum. This maximum in free energy arises from the large surface-to-volume ratio of small aggregates. The dependence of the Gibbs free energy of an aggregate is shown schematically in Fig. 2.8. Assuming a metastable equilibrium between the adsorbed monomers and aggregates of various sizes, the concentration n^* of nuclei with critical size D^* is given by:

$$n^* \propto \exp\left(\frac{-\Delta G^*}{k_B T_S}\right) \tag{2.24}$$

with ΔG^* being the corresponding critical Gibbs free energy. Critical nuclei can grow to supercritical size by direct impingement or through incorporation of adsorbed atoms diffusing on the surface. Taking into account their reevaporation energy barrier ΔG_{des} and the surface diffusion energy barrier ΔG_{sd} one can find the proportionality for the

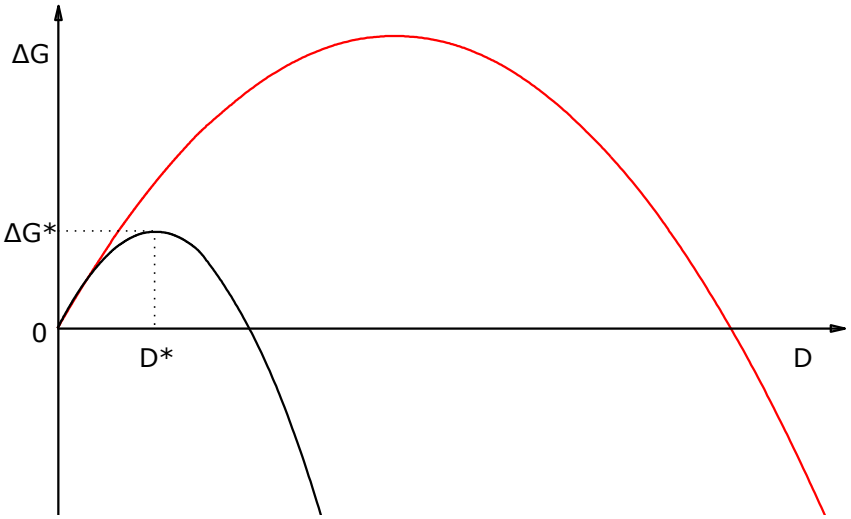

Figure 2.8: Schematic plots of the formation energy ΔG of two different adatom material compositions. The energy barrier for formation is significantly lower for one type of nuclei. The maximum in the Gibbs free energy ΔG^* is reached when a nucleus reaches the critical diameter D^*.[95]

nucleation frequency I^*:

$$I^* \propto \exp\left(\frac{\Delta G_{des} - \Delta G_{sd} - \Delta G^*}{k_B T_S}\right). \tag{2.25}$$

$\Delta G_{des} - \Delta G_{sd} - \Delta G^*$ denotes the energy barrier to nucleation, one of the fundamental physical parameters accessible to growth experiments.[123] In this framework, in particular the comparison between the behavior of GaN NW nucleation with and without supply of Mg will be described in section 4.1.1.[118] Very well described is the incubation phase that follows immediately after the opening of the shutters of the effusion cells in GaN NW nucleation.[116,118,123–128] Its origin is the formation of the initial subcritical aggregates that eventually grow to critical size. Once the critical size is reached and GaN growth starts, spherical caps are formed that grow to a certain size and then, through plastic relaxation of the strain, form the NWs which continue to grow predominantly along the c-axis afterwards.[19,129,130] It is worth to note here that NW density, degree of coalescence, tilt and twist are determined or influenced during the nucleation stage. One can manipulate the nucleation through several growth parameters available in MBE (T_S, III/V ratio, growth rate, substrate preparation, growth interruptions, supply of additional atomic species) and therefore try to influence the final shape and density of the wires in a desired way.[118,123,124,128]

GaN nanowire growth mechanism

After the nucleation phase, several mechanisms influence the growth of the NWs. Adatoms on the surfaces of the substrate and the NWs can diffuse or desorb, NWs can coalesce if they touch each other during their individual growth, at elevated temperatures decomposition of already formed material might occur and due to the high number density of the NWs on the substrate geometrical effects can lead to shadowing. All these effects are addressed in this section.

Atoms that are adsorbed on the substrate or the NW can either diffuse or desorb again. The desorption properties of Ga atoms on GaN are well studied. The conclusion of these studies is that, even under N-rich condition, a Ga-bilayers can form without the formation of droplets. Desorption of Ga is favored if the layer is not closed but can also takes place directly from the bilayer.[131–134] In the case of the NWs it is questionable whether the supply of Ga is sufficient to form an ad-layer or not. The mean residence time τ_a may also differ significantly on the different surfaces of the NW. A difference in this sticking property was proposed to be the driving mechanism behind the NW growth by Bertness *et al.*[135]. Between adsorbtion and desorbtion, the atoms can diffuse along the surface they are attached to. This diffusion process is widely excepted to be a major contribution to the growth of GaN NWs.[136–140] As the NWs are grown in N-rich condition, an oversupply of N is assumed and therefore only the diffusion of the Ga ad-atoms is taken into account for the following considerations. The diffusion takes place along the substrate surface, on the NW sidewalls and also on the top facet of the wires, see Fig. 2.9. It was found experimentally that the axial growth rate of the NWs is higher than the Ga-flux would allow for a two-dimensional layer. This means that apart from the Ga impinging on the top of the wire a diffusion from the side walls of the NW towards its tip takes place. Thus the incorporation rate at the tip is higher than the Ga-flux would normally allow and therefore the growth rate is increased.[138]

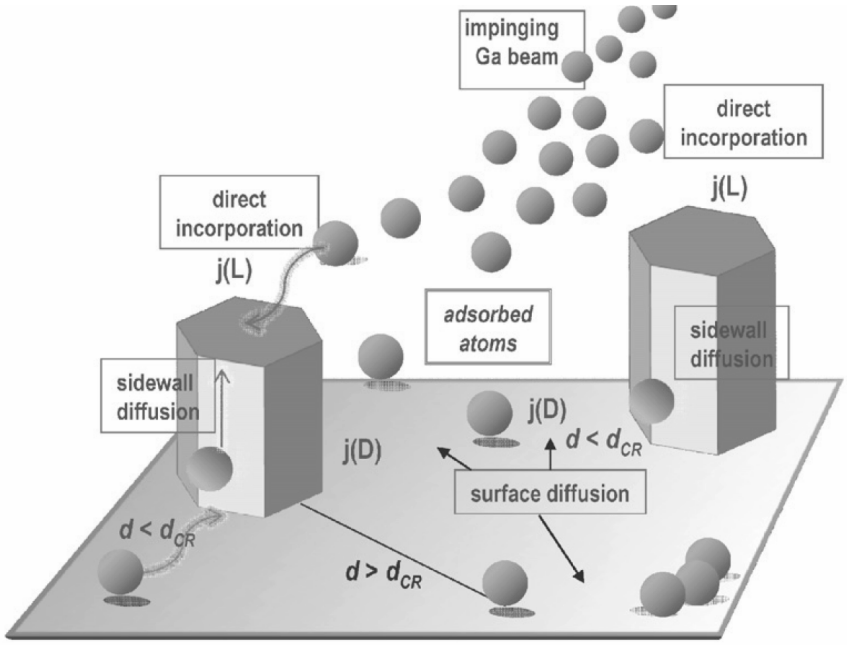

Figure 2.9: Diffusion processes during the growth of GaN NWs.[136]

The introduction of an AlN marker layer into the GaN NWs was used to determine the difference in growth rate of axial and radial growth and it was found that due to the favored incorporation at the NW tips the axial growth rate is 33 times higher than the radial one.[126] This type of growth mechanism leads to an enhanced growth rate for wires with a small diameter d, compared with their thicker counterparts. As the top surface area is proportional to d^2 and the perimeter through which diffusion to the top can occur is proportional to d, the axial growth rate turns out to be proportional to d^{-1}. In addition, this allows the determination of the diffusion length on the side facets and a

value of 40 nm was found.[139] This diffusion length can of course be influenced by the growth parameters, especially the substrate temperature T_S has a significant influence on the exact value. As the diffusion is such an important part of GaN NW growth, detailed theoretical studies have been performed to model this system and to gain insight into the microscopic processes.[141,142]
Coalescence is an effect which takes place if two or more neighboring NWs touch each other and from there on form a single entity. Tensions (strain, stress) in the crystal will be present, if the crystalographic orientation is not exactly the same. These tensions are in some cases relaxed via the introduction of structural defects.[49,50,143] This results in a degradation of the optical properties and is therefore in most cases not desired. On the other hand, for some applications it is deliberately enhanced, e.g. to create high quality strain free layers of GaN on foreign substrates.[144]
The decomposition is a thermally activated process which separates the compound crystal into its atoms. At the used growth temperatures, this effects does play a significant role. This is in particular the case for the InGaN growth described in chapter 5. In this case, T_S is well above the decomposition temperature of the In-N bond of around 470 °C.[145,146] Here, as well as in most cases of self-induced NW growth, the equilibrium between the formation of bonds and their thermally activated breaking influences the morphology, growth rates and in the case of InGaN the composition (see chapter 5).[147]
The geometry of the growth chamber is also of importance for GaN NW growth. In particular the inclination angle under which the cells are mounted, with respect to the substrate can have a significant influence (see Appendix B).[148,149] The directed molecular beams are usually not perpendicular to the substrate and therefore the growing NWs do not only shadow one half of their own surface but, at sufficient densities and NW length, also their neighbors. This can lead to a deficiency in material supply of the NWs which are shadowed and can result in a decreased growth rate for that particular wire. Lagging behind the other wires in height enhances the shadowing effect and finally some wires stop to grow altogether.[150]

3. GaN nanowires

GaN NWs grown in a self-assembled fashion by MBE exhibit very good crystal quality.[7,18,151,152] They can be grown on a variety of surfaces. Besides the growth on a thin SiN_x or AlN layer on Si(111), both of which are used in this framework, also the possibility to grow on Al_2O_3 [153,154] and even thick SiO_x [19] layers has been demonstrated.
In order to be able to exploit their superior material quality it is necessary to create a device made of GaN NWs. A device such as an LED involves p- and n- type doping as well as alloying with another element to form QWs (see section 2.2). As the additional supply of these elements can change the growth behavior of GaN NWs it is worth to take a look at the unperturbed GaN NW growth. The goal of this chapter is to get an overview of GaN NW growth. In particular the time evolution of the geometrical parameters of the NWs is of interest. In addition, some further observations will be discussed which are typical for GaN NWs. These will act as a basis for comparison with NWs which are exposed to additional atomic species for doping and alloying purposes, described in chapter 4 and 5.

3.1. Growth via MBE

In Fig. 3.1 two scanning electron microscope (SEM) images of a typical GaN NW ensemble are displayed. The image Fig. 3.1a) was taken at an angle of 45° with respect to the substrate normal. These kinds of images will be called birds-eye images throughout the remainder of this thesis. Fig. 3.1b) was acquired with the view parallel to the surface normal (top view image). A third common image geometry which is not shown here is the cross section image in which the view is parallel to the substrate surface.
Fig. 3.1a) shows many NWs with different length and also diameters. This is a major drawback for the self assembled growth of GaN NWs, as this makes processing all of them at once difficult. A solution for this might be the selective area growth of NWs [113,155–158] discussed in the outlook (chapter 7). Some effort will be undertaken in

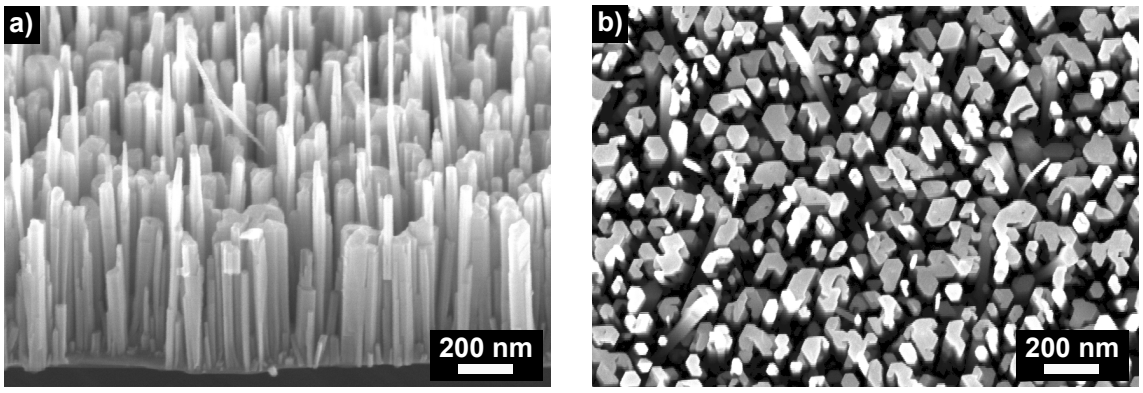

Figure 3.1: SEM birds-eye a) and top view b) images of a typical GaN NW ensemble.

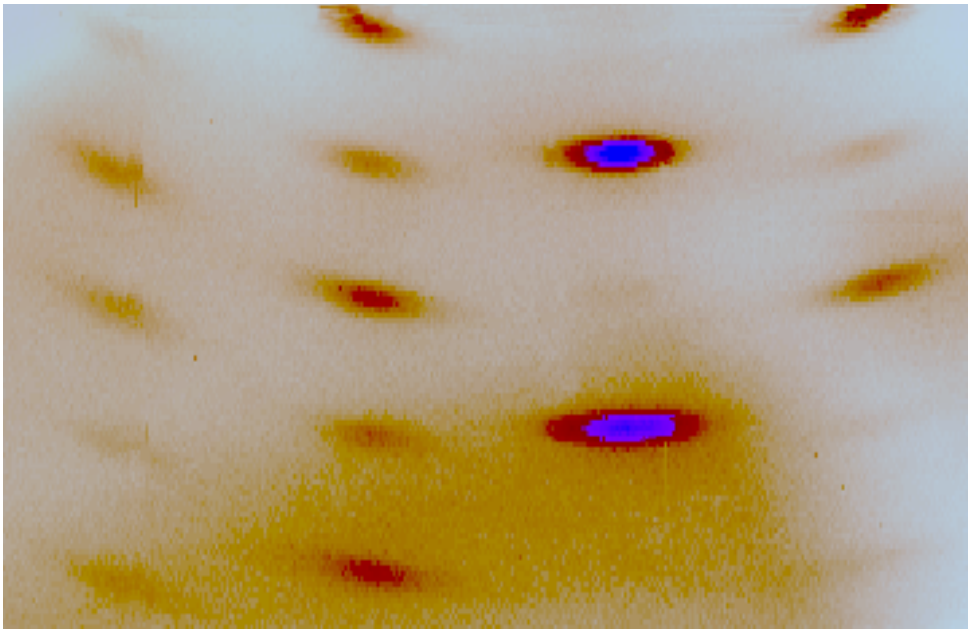

Figure 3.2: RHEED image of well developed GaN NWs at the end of the growth run.

this chapter to try to understand the geometrical properties of the GaN NW ensemble. In Fig. 3.1b) the hexagonal nature of the wurtzite GaN crystal structure can be recognized through the cross section of the NWs. Also, their side facets are aligned along three preferential directions, indicating an epitaxial relationship with the substrate. The existence of this relationship has been proven through x-ray diffraction (XRD) reciprocal space maps.[143] In addition, one can see that several NWs have coalesced, while others have a rather small diameter indicating that they grew undisturbed by their neighbors until the growth was terminated. Several very small NWs are visible in Fig. 3.1a), these can not be seen in the top view imaging mode.

The wurtzite structure of the GaN NWs can be directly observed with RHEED. The patterns produced by the GaN NWs correspond to the hexagonal wurtzite structure of GaN with the c-axis parallel to the substrate normal. However, the spots appear as broken rings (see Fig. 3.2) as reported in[117,159] which indicates a misorientation of the NWs in the form of a twist with respect to the Si substrate. The patterns in the two azimuths are different as is expected for growth on Si(111).[117] This indicates a preferential orientation with respect to the substrate and is another indication that some crystallographic information is passed from the substrate to the NWs in spite of the presence of an amorphous Si_xN_y interlayer caused by the reactive N used for the growth (please find more on this topic below).

Top view images also allow the determination of the NW density on a given sample. For most samples densities in the order of 10^{10} cm^{-2} are commonly found. This results in an average distance of around 40 nm - 100 nm between the NWs. The self organized growth of the NWs raises question about the interaction of neighboring NWs during growth and especially during the nucleation phase. The 2-dimentional radial distribution function (RDF) allows to check for long range coordination between the NW nuclei. It describes the density as a function of distance from a reference point, in this case the center of a NW. The RDF of a NW sample with 10 min growth time and a density of $4 \cdot 10^{10}$ NW/cm^2 is shown in Fig. 3.3. The vertical line indicates the mean distance of 50 nm between the

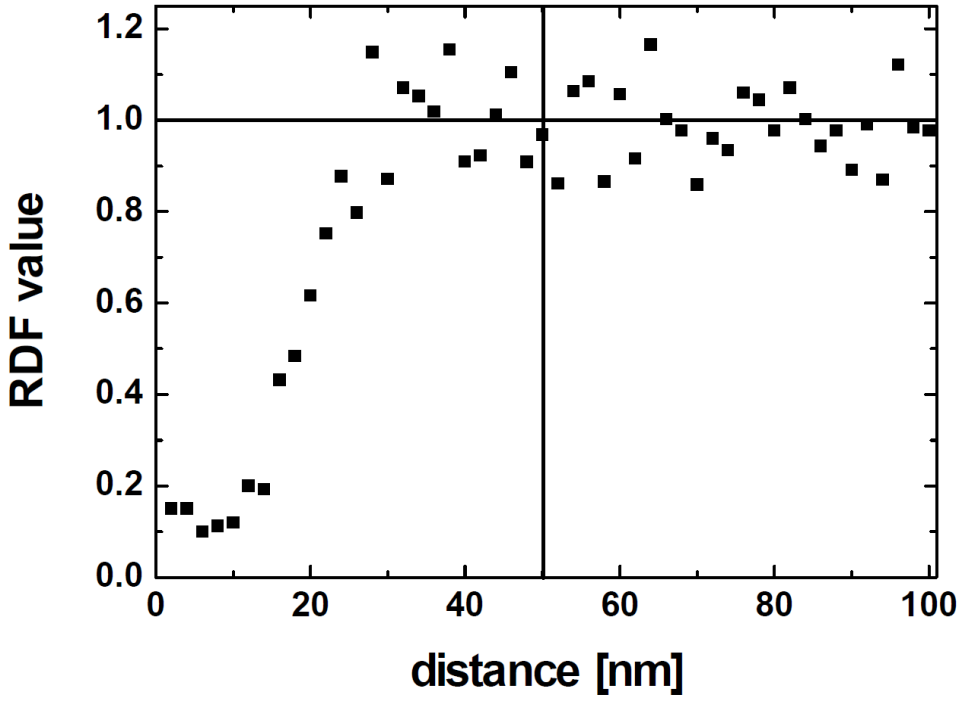

Figure 3.3: Plot of the radial distribution function (RDF) of a GaN NW ensemble with a density of $4 \cdot 10^{10}$ NW/cm^2. The vertical line indicates the mean distance between the NWs. The horizontal line repersents the expected value for a random distribution.

NWs. The horizontal line represents the expected value for a random distribution. The result shows no oszillation around the value 1 and therefore no long range correlation of the NWs. Only a minimum distance of 28 nm $\pm$ 4 nm can be extracted from the initial rise of the signal. This value is also found for a NW ensemble with only half the density. Considering that this distance is measured from the center of one wire to the center of all others, their finite size need to be taken into account. This leads to the conclusion that the GaN NW nucleation sites are randomly distributed.

Length versus diameter (L-D) plots were created, in order to gain insight into what governs the GaN NW ensemble composition with respect to the different geometries of the NWs. A plot typical for GaN NWs can be see in Fig. 3.4. For the creation of such a plot, both length and diameter of a large number of NWs needs to be determined from cross section images, such as the ones of the left hand side of Fig. 3.5. Special care needs to be taken that only the NWs in the first row (the ones that can be seen in full) are counted. Counting NWs which are partly covered by others in front of them, will result in an over estimation of the long NWs. Another cautionary note must be made with regard to the diameters. Several NWs do not have a perfect hexagonal symmetry, as can be seen in the top view image Fig. 3.1b). This leads to an error in the determination of the diameter, as the cross section images only allow to see a projection of the NWs. Nevertheless, this is the only way of measuring both length and "diameter"at the same time for a large number of NWs.

In the plot three different types of NWs are identified and distinguished by the different colors. Data point marked in black represent small NWs which are most likely not seen in top view images. They have suffered from shadowing caused by their neighbors

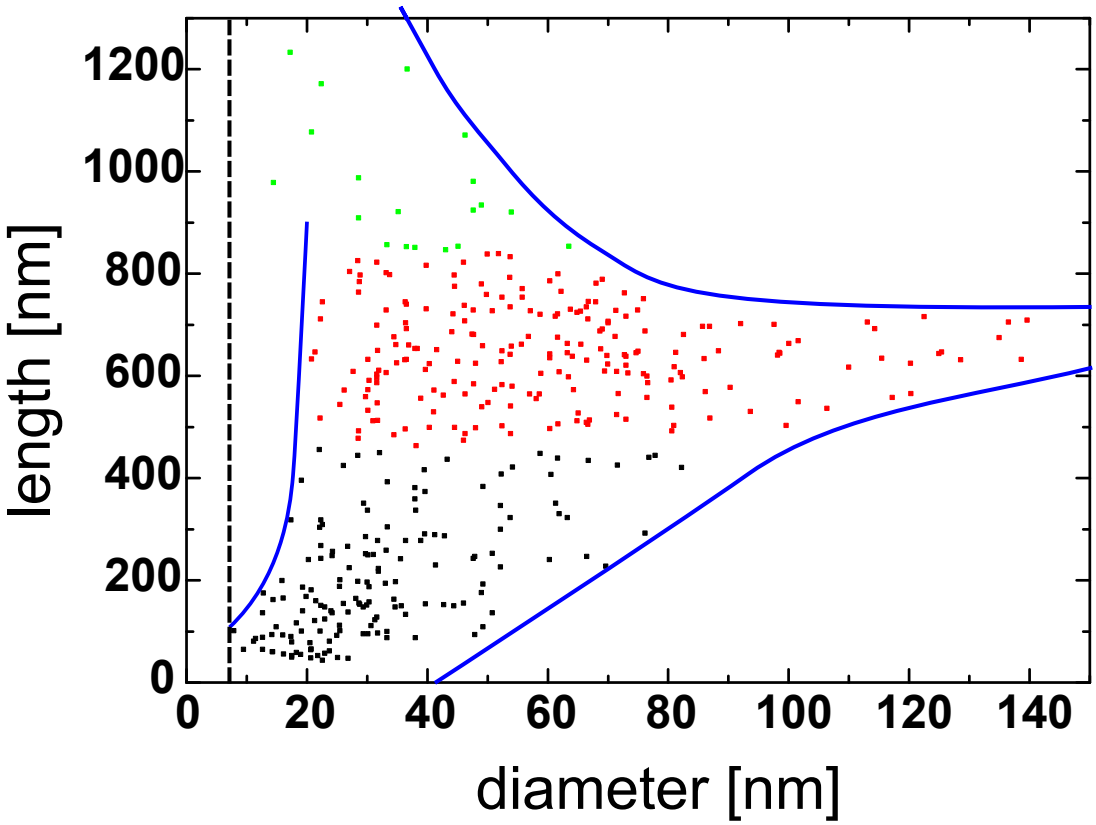

Figure 3.4: Length versus diameter plot of a typical GaN NW ensemble. The dashed and blue lines serve a guide to the eye only and are intended to point out the region of the diagram where NWs can be found. The three colors of the data points allow the identification of different NW classes.

and were cut off from the material supply at some stage during growth. Therefore, their growth stopped while the NWs around them continued growing. See the time evolution series in Fig. 3.5, for further comparison. The red data points mark the NWs that fall in a rather narrow length window (in this case between 500 nm and 850 nm) but have a fairly broad diameter distribution. These NWs represent the majority of the ones which actively took part in the growth at the moment the experiment was stopped.
The large diameter distribution is due to coalescence of neighboring NWs, which continued to grow as one entity after coalescence. Data points marked in green represent the few NWs with very high aspect ratios. The length growth of these NWs benefits from the fact that they do not suffer any shadowing and were also not subject to coalescence in the early stages of the growth. Due to the nature of the GaN NW growth in which diffusion plays a significant role, thin NWs exhibit an enhanced length growth.[139]
The dashed line in Fig. 3.4 marks the lower limit for the diameter. No NW with a smaller diameter can be found on this sample. Throughout the investigation of L-D plots the value found for the minimum diameter is 7 nm $\pm$ 2 nm, which is consistent with earlier findings on the estimation of the critical diameter for NW nucleation.[19]
The blue lines serve as guides to the eye only and are intended to point out the region

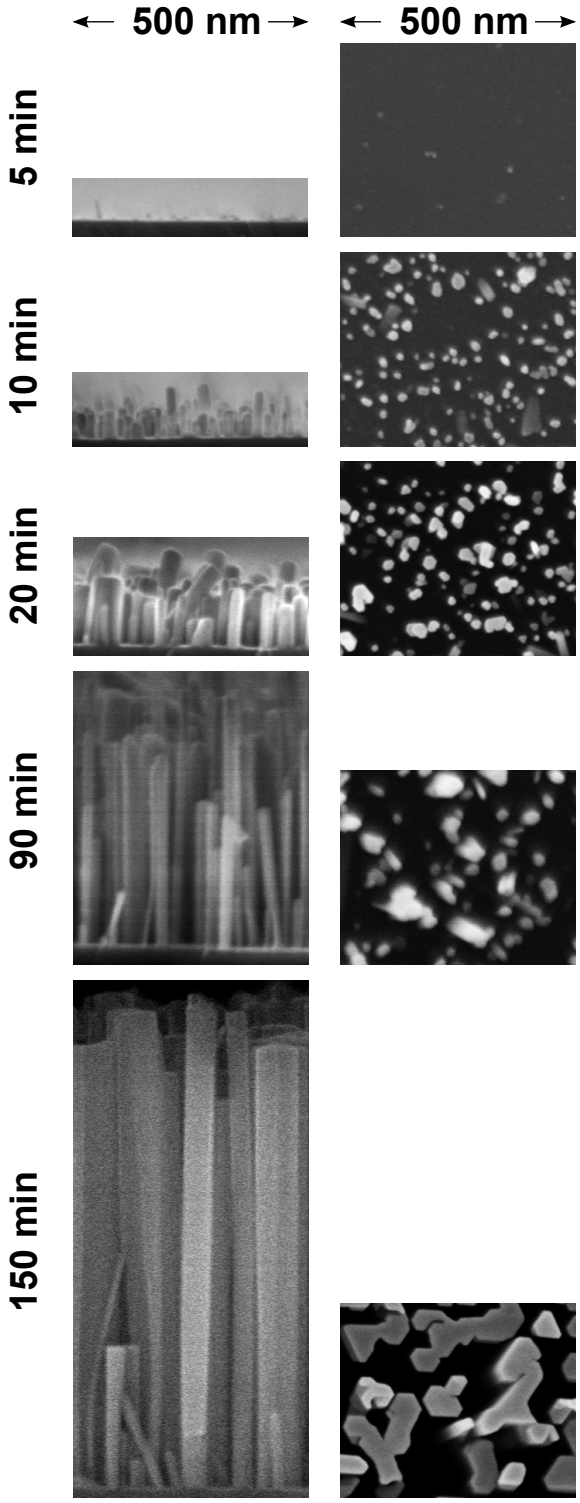

Figure 3.5: SEM cross section and top view images of a GaN NW growth time series.

of the diagram where NWs can be found. The shape of the top right line is again due to diffusing Ga atoms, which move towards the NW top, where they contribute to the

growth (see section 2.4). This growth dynamic causes a proportionality

$$l \propto \frac{1}{d} \tag{3.1}$$

for well developed NWs, which are only slightly or not at all disturbed by the neighboring NWs.[139]

The bottom right line in Fig. 3.4, is the one which defines that NW growth is occurring. To the right of this line aspect ratios would get smaller and smaller. A compact layer would have an infinite diameter at any height. Island like nano structures have typically aspect ratios in the order of one or below. All these structures would be found to the right of this line. A high aspect ratio, on the other hand, is inherent to NWs. If a NW like growth is dominant, a delimitation in the form of this line will always be present in such a kind of L-D plot.

The blue line towards the left in Fig. 3.4 shows that NWs also grow in diameter as they increase their length. Still, length growth is favored over diameter growth by far. This finding is in line with previous publications of a 33 times higher vertical growth rate compared to the radial one.[126]

In Fig. 3.5 both cross section and top view SEM images of NWs grown under the same conditions but for different durations are shown. This kind of representation gives insight into the evolution of GaN NWs during MBE growth. At the early stages hardly any growth takes place at all. After 5 minutes almost no structure with an aspect ration of one or grater can be found. Another 5 minutes later and therefore 10 minutes into the growth a multitude of NWs can be found. They have a rather large relative spread in both length and diameter. 20 minutes into the growth the first coalescence events have taken place and the nucleation process has most likely terminated. After 90 minutes a typical NW ensemble has developed with long and thin NWs, some large diameter NWs which have undergone coalescence, and some NWs where growth stopped as they were shadowed by their neighbors. 180 minutes into the growth the degree of coalescence has increased and of course also the overall length of the NWs. Yet, the general observation of the existence of three types of GaN NWs in an ensemble, discussed before, also applies here.

The development of the NWs with time can also be very well appreciated by looking at the corresponding L-D plots. These are displayed along side with histograms of the NW length in Fig. 3.6. The development of the NW class, which has undergone coalescence, can be observed especially well in the L-D plots. Looking at the histograms for 90 and 180 minutes one can also observe a narrowing of the length distribution for the most frequently found NW length. This narrowing might be explained by the influence neighboring NWs have on each other due to Ga ad-atom desorption, re-adsorption and shadowing processes. A model describing such kinds of events and growth dynamics is currently in preparation.[160]

Transmission electron microscope (TEM) cross section images, like the ones shown in Fig. 3.7a) and b), consistently show the formation of an amorphous Si_xN_y layer between the substrate and the NWs. This layer develops due to the exposure of the Si surface to the highly reactive species of the N-plasma needed for nitride NW growth. It can be avoided by the deposition of Al prior to the ignition of the plasma source. Yet, GaN NWs also grow on this nominally amorphous Si_xN_y layer in a good relationship with the underlying Si substrate.[143]

Also in high resolution TEM (HRTEM) images, such as Fig. 3.7b), the wurtzite crystal

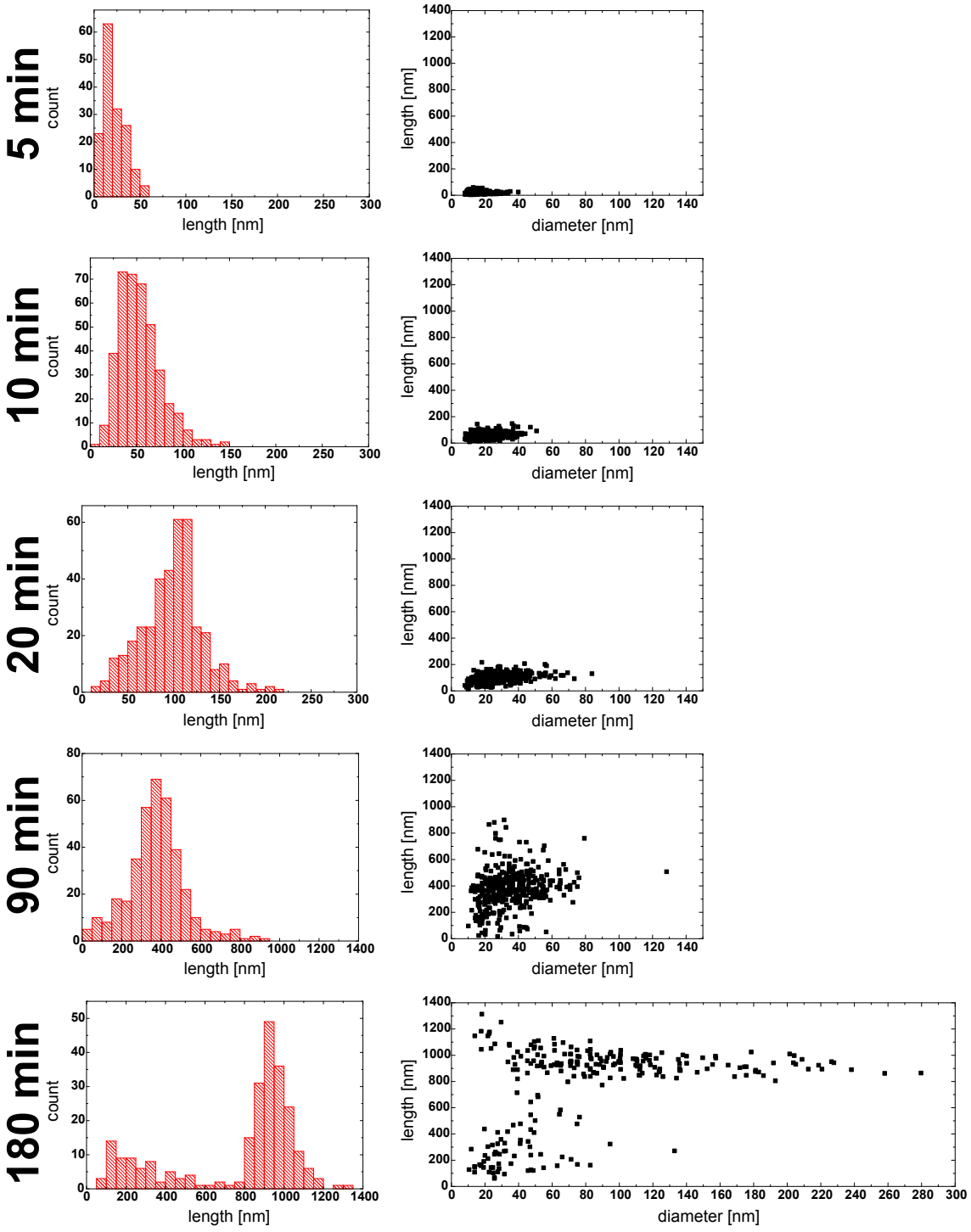

Figure 3.6: Histograms of the length development of GaN NWs over time and the corresponding L-D plots. Note the change in scale of the histograms from 20 to 90 minutes. SEM images for the plotted data can be found in Fig. 3.5

structure of the NW can be identified. The c-axis is found to be parallel with the substrate normal, in both the real space images as well as the diffraction images (not shown here). Therefore the top facet of the NWs is the c-plane of the wurtzite crystal while the

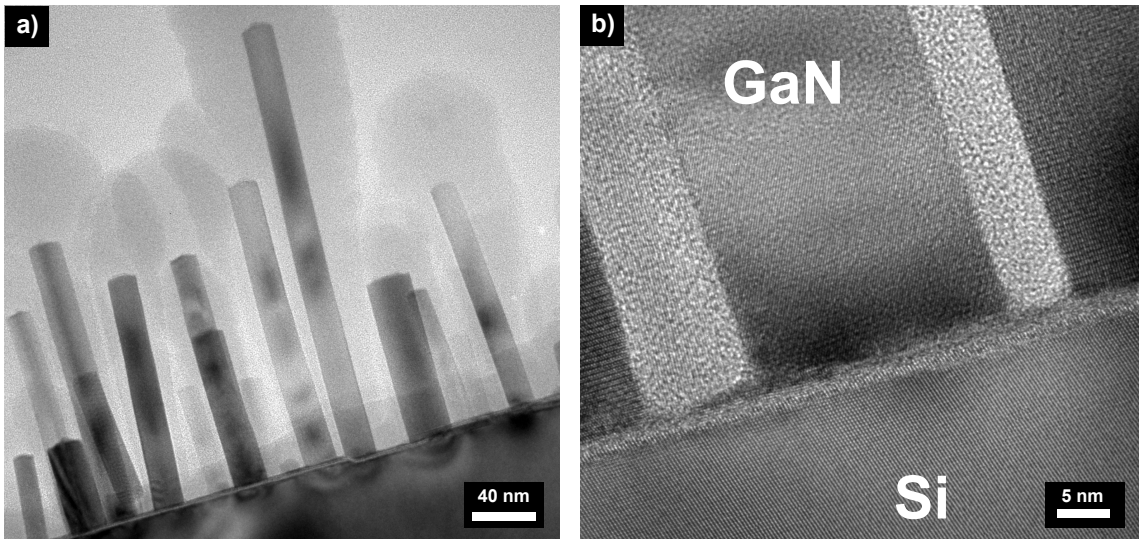

Figure 3.7: TEM cross section images of GaN NWs on a Si(111) substrate. The gray shadow surrounding the NWs at their top in a) is SiO_2, subsequently deposited for preparation reasons. The data was acquired by E. Sutter, Brookhaven National Laboratory.

NW side facets are a-planes.

3.2. Optical properties

Throughout this thesis, photo- and cathodoluminescence experiments will be used to characterize the synthesized samples. Both relay on the creation of free charge carriers and their recombination. The light emitted by this recombination process, carries information about the electronic structure of the material which can be extracted through a measurement of its wavelength. PL and CL differ only in the excitation source used which in both cases have their advantages and disadvantages.
A typical PL spectrum of GaN NWs is displayed in Fig. 3.8. The very prominent feature which can be seen in the linear scale PL spectrum of Fig. 3.8a), is the near band edge (NBE) peak of the GaN. It consists of donor and acceptor bound excitons as well as free excitons.[21] Both DBE and ABE can be resolved clearly in logarithmic representation (see Fig. 3.8b)). It is noteworthy, that no significant luminescence in the region between 1.9 and 3.0 eV is detectable. GaN films suffer frequently form defects which cause traps at these energies and are associated with a bad crystal quality.[28,48]
Another feature can be spotted in the logarithmic plot of Fig. 3.8b). The broad emission between 3.0 eV and 3.3 eV is associated with a DAP transition caused by Mg which acts as an acceptor in GaN.[13,28] This is a recurring feature in the PL even though no Mg was supplied during growth. It is most likely caused by a property of Mg commonly known as the "memory effect"of Mg, which is frequently found in growth chambers.[161]
Another feature which is frequently observed, but appears here only as a shoulder of the NBE peak, is the transition at 3.42 eV (SF). This transition is associated with excitons bound to stacking faults which usually occurs in NWs when coalescence is involved.[50]
For a more detailed analysis of the general luminescence properties of GaN NWs, the reader is referred to the Ph.D. thesis of Carsten Pfüller.[21]

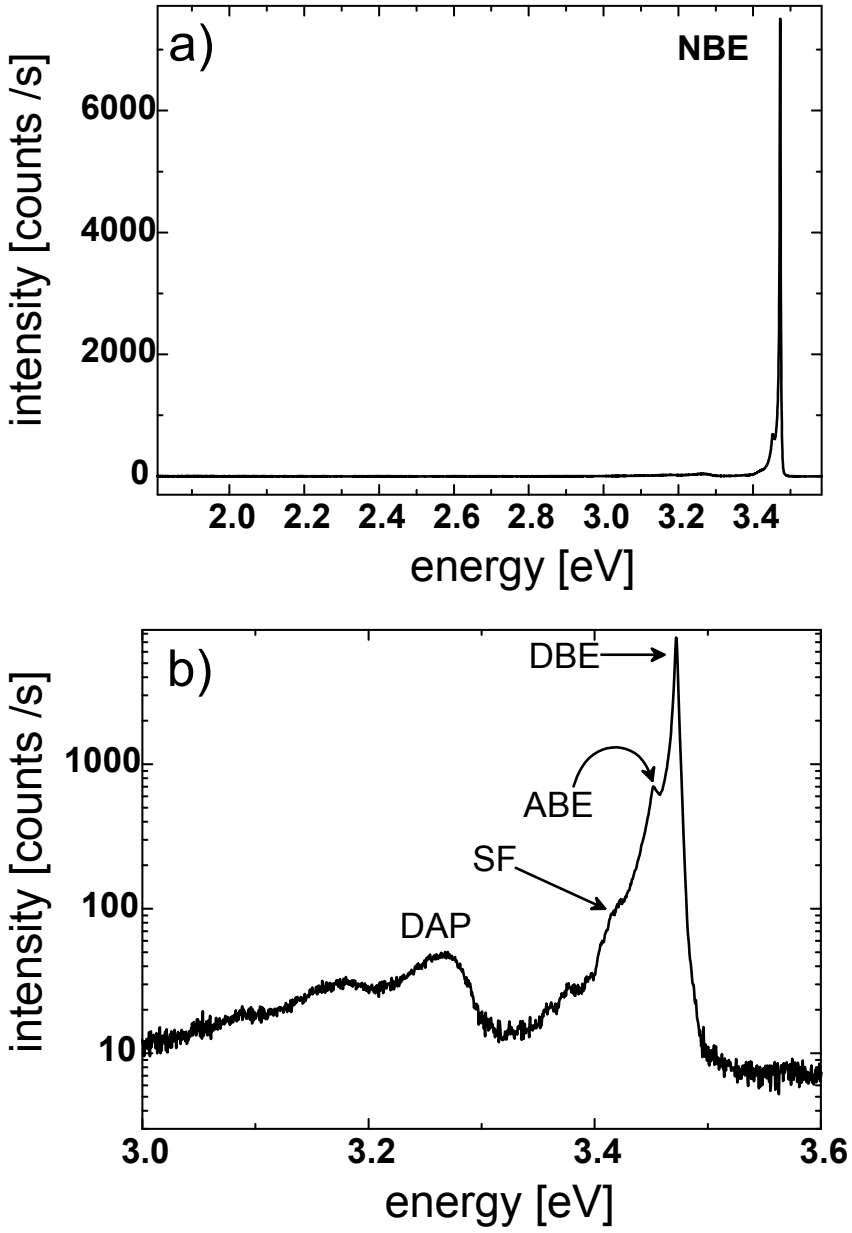

Figure 3.8: PL of a typical GaN NW ensemble in a) linear and b) logarithmic scale measured at 5 K.

Conclusion

The general properties of MBE grown GaN NW have been presented. Especially the time evolution of the NWs was investigated. L-D plots were presented and used to connect the experimental findings with the growth model favored in contemporary literature on the topic. The luminescence properties of GaN NWs were discussed.

4. Doped GaN nanowires

The control of the electrical properties of GaN is the first obstacle which needs to be overcome in device development, as is the case for any semiconductor. This chapter focuses on p- and n-type doping of GaN.
The aim of this chapter is to investigate the changes in growth behavior and morphology which occur when doping species are supplied to the MBE growth of GaN NWs.
At first, section 4.1 will look into doping GaN NWs with Mg. The subsequent section 4.2 highlights the effects of supplying Si. Implications for the growth as well as the optoelectronic properties of GaN NWs will be discussed respectively.
Finally, in section 4.3, the knowledge gained regarding the influence of the two doping species will be combined to form nominal p-i-n and n-i-p junctions in GaN NWs.

4.1. Magnesium doped GaN nanowires

Controlled p-doping in a wide concentration range is very difficult for wide bandgap semiconductors. Unintentionally doped GaN is typically n-type. The reason for this background doping are O and Si impurities. Native point defects such as vacancies, antisite or interstitial defects, were found to be less likely to cause the high n-type background.[28,162] Initial efforts in the 1990s to obtain p-type doping resulted in heavily compensated, highly resistive films. Therefore, the topic was of prime interest in GaN research for many years.[28] In GaN NW growth, the self-purification effect[163] or the peculiarities of the growth mechanism might hamper the incorporation of the p-type doping species. Thus it is challenging to overcome compensation and reach true p-type material. In this chapter, the effects of an additional supply of Mg, which acts a p-type doping species,[28,164] to GaN NW growth will be discussed. Initially, a nucleation study will give insight into the chemical activity of Mg during this growth phase. This is followed by the general morphological and optoelectronical changes observed by doping GaN NWs with Mg.[150]

4.1.1. Nucleation

This subsection reports on how a supply of Mg effects the duration of the incubation time and the nucleation speed. The incubation time and its evolution with the growth temperature are monitored by RHEED and by a LS-QMS to detect the Ga desorbing from the substrate.[116] Subsequent to the growth, SEM top view and cross section images were taken. These results are also correlated with the statistical analysis of samples grown for only very short times.
The N/Ga flux ratio of 6.5 was kept constant for all samples. Prior to the growth, the native Si oxide was removed *in- situ* by the deposition of a Ga layer. The Ga reacts with the O of the native SiO_x layer on the substrate to form Ga_xO_y. This Ga_xO_y can then be desorbed by raising the temperature until the Si(111) 7×7 reconstruction is observed by means of RHEED. Subsequently the Si surface was nitridated for 5 minutes. Two sets

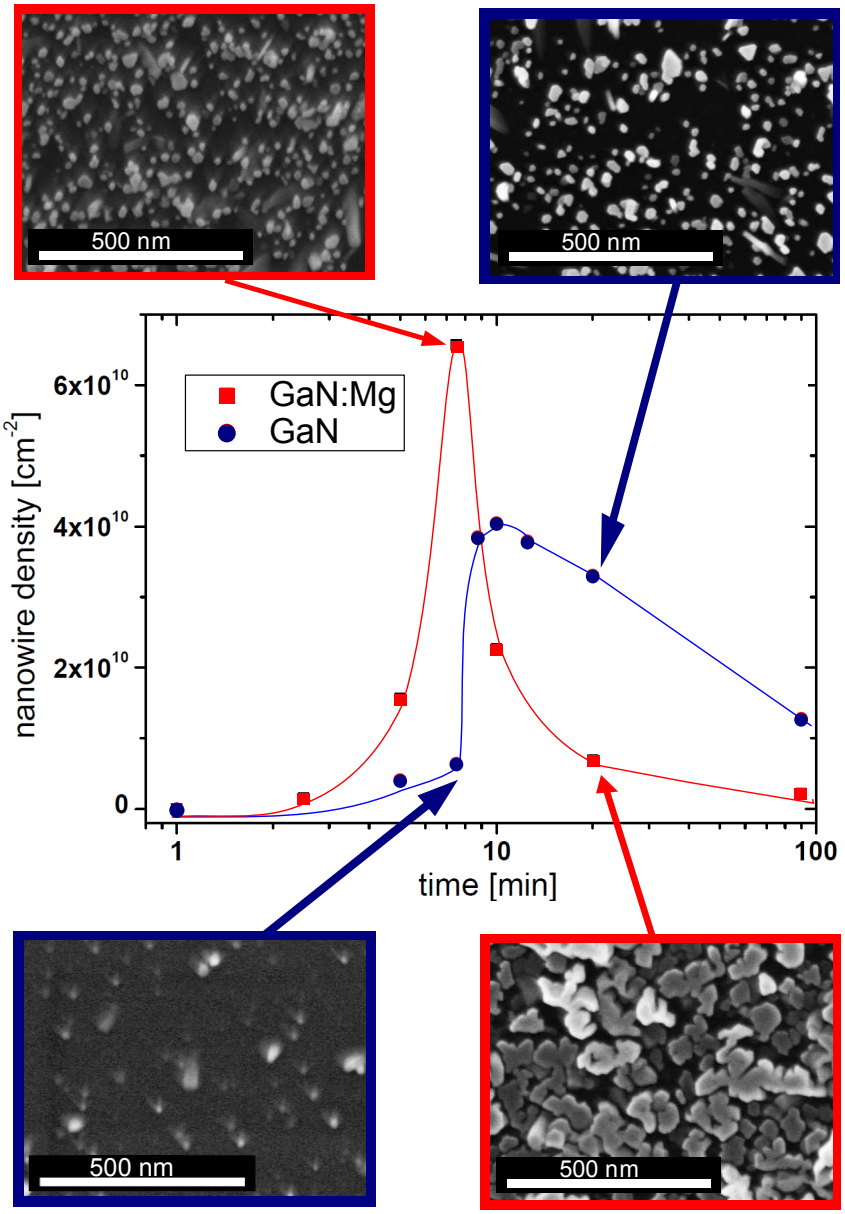

Figure 4.1: The density of NWs per unit area is plotted against the growth time for both Mg doped and undoped samples. The insets show SEM top view images of the indicated samples. The red and blue solid lines serve as a guide to the eye only.

of GaN NW samples were grown. The first set was a time dependence series for the investigation of the nucleation phase with the following growth parameters: T_S of 790 °C, nominal growth rate of Ga of 2 nm/min and N of 13 nm/min.[165] For the second set of samples, T_S was varied between 760 °C and 806 °C using the same Ga and N rates employed for the first set. Both series were grown twice, once with Mg supply and once without. The Mg source was set to 300 °C which yields a beam equivalent pressure (BEP) of $BEP_{Mg} = 2.5 \cdot 10^{-8}$ mbar.

Based on the SEM top view images of as grown samples obtained for different growth durations, a statistical analysis of the areal density of the NWs was carried out. In Fig. 4.1, the NW density on the samples grown under Mg supply (red squares) and the ones with

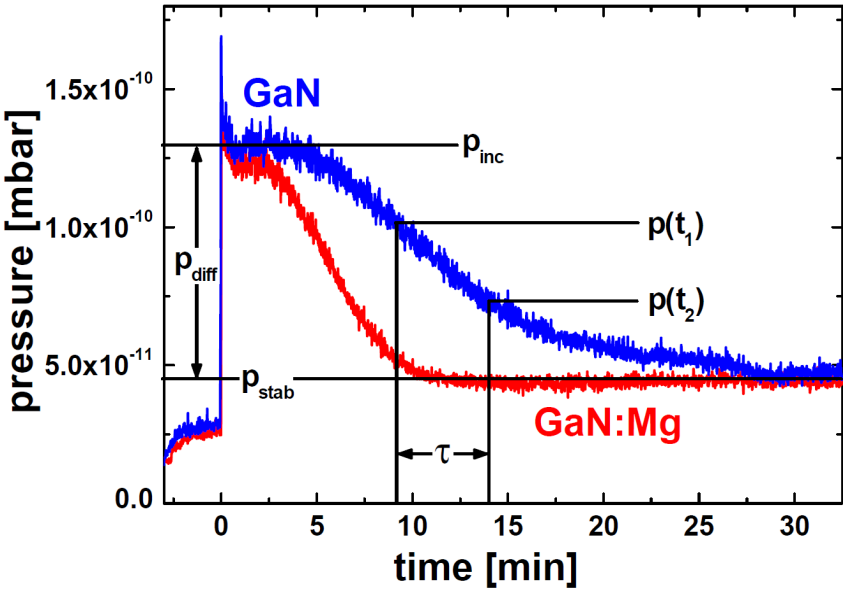

Figure 4.2: The partial pressure of ^{69}Ga as detected by the LS-QMS in the growth chamber is plotted versus the growth time for two samples, one with (blue) and one without (red) Mg supply.

undoped GaN (blue circles) is plotted versus the growth time. Both, the series with Mg supply and the one without show the characteristic behaviour of GaN NW growth described by other authors.[116,123–127] In the initial phase, an incubation time can be observed during which no NW growth takes place. Subsequently, the nucleation phase follows, which causes a rapid jump in NW density on the substrate surface to values above $4 \cdot 10^{10}$ cm^{-2} in both cases. For longer deposition times, the NW density decreases due to coalescence of closely spaced NWs.[50,126] Widely spaced wires, however, continue to grow separately.
Comparing the results of the two series, it is evident that the nucleation under Mg supply is more rapid. In fact, the maximum NW density is reached earlier than it is the case for the undoped samples. This is underlined by the SEM top view images of the samples grown for 7.5 minutes shown in Fig. 4.1. At the same time, the tendency to coalesce is much stronger for the Mg doped wires (GaN:Mg) compared to their undoped counterparts (GaN). This tendency of stronger coalescence has been previously observed and has been linked to an enhanced lateral growth rate[150,166] (see also section 4.1.2). The observation is confirmed by SEM top view images shown in Fig. 4.1 associated with the samples grown for 20 minutes. The higher absolute NW density during nucleation implies also that the NW nuclei are more closely spaced in case Mg is supplied. This phenomenon, along with the higher lateral growth rate, drives the enhanced coalescence as NWs touch each other much earlier during growth.

Fig. 4.2 shows the typical LS-QMS signal observed for ^{69}Ga during the nucleation of GaN NWs. The origin of the time axis was chosen to be at the moment of the opening of the Ga shutter. Prior to this, the signal settles on a background value that is determined by the N supply to the plasma source and its stabilization. Upon opening of the shutters, the ^{69}Ga signal increases rapidly and settles again at a value which we define as p_{inc}, in this case at $1.3 \cdot 10^{-10}$ mbar. The growth stage in which the signal stays con-

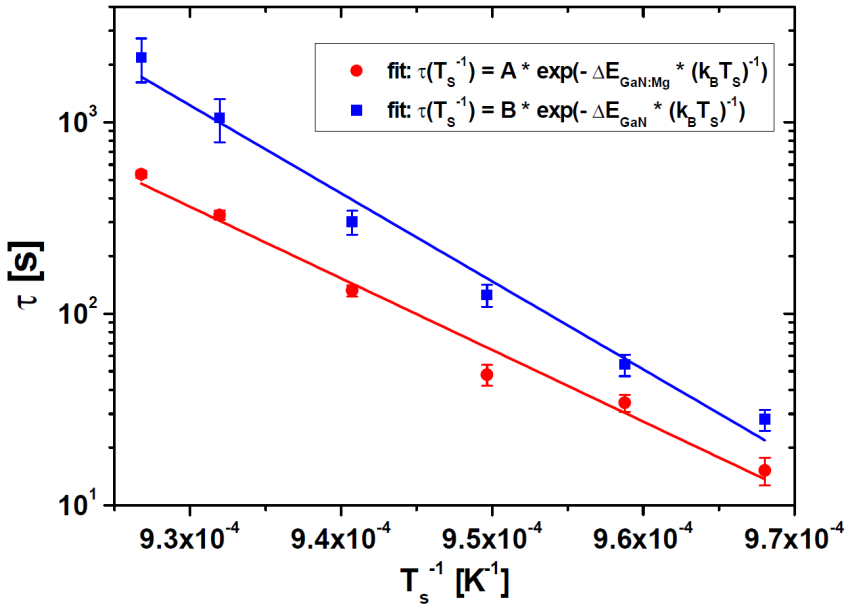

Figure 4.3: Arrhenius plot of τ. Both data sets were fitted with an exponential function.

stant, can be associated with the incubation time, as no RHEED pattern indicating GaN is observed.[116] The absolute level of this signal and the duration of the incubation time depend strongly on the growth temperature, as well as the Ga flux. Subsequently, the nucleation phase takes place, evidenced by a decrease in the ^{69}Ga signal. The reason for the decrease of the signal is the incorporation of Ga atoms into the nuclei which form GaN. The rate at which this process occurs strongly depends on the number of already formed nuclei. A RHEED pattern typical of GaN NWs starts to appear at the same time the decrease begins. Its intensity steadily increases for the duration of this nucleation phase. Finally, once nucleation has finished, the Ga desorption measured by the LS-QMS and therefore also the incorporation rate of Ga stabilizes at values which remain constant throughout the remainder of the entire growth run. For the samples presented in Fig. 4.2, this level, which we define as p_{stab}, is at around $4.5 \cdot 10^{-11}$ mbar. At this stage, the amount of incorporated and desorbed Ga does not depend on whether Mg is supplied or not.

While the qualitative behavior of the LS-QMS signal is quite the same for GaN and GaN:Mg, a striking difference in the speed with which nucleation occurs. In the case of GaN:Mg, the nucleation phase is much shorter. In order to quantify this nucleation speed, the LS-QMS signal was analyzed in more detail. In particular, the slope of the ^{69}Ga desorption decrease is of interest. In the intermediate stage between saturation and incubation time, this decrease is almost linear. As the absolute values of the saturation level may vary due to differences in background pressures, the pressure difference (p_{diff}) defined as:

$$p_{\text{diff}} = p_{\text{inc}} - p_{\text{stab}} \tag{4.1}$$

is introduced (see Fig. 4.2 for comparison).
This value is determined for each growth run. With this information, the times t_1 and t_2,

when the LS-QMS signal reaches a partial pressure level of,

$$p(t_1) = \left(p_{\text{stab}} + \frac{2}{3} \cdot p_{\text{diff}} \right) \tag{4.2}$$

and

$$p(t_2) = \left(p_{\text{stab}} + \frac{1}{3} \cdot p_{\text{diff}} \right) \tag{4.3}$$

are extracted. Between these pressure levels, the LS-QMS signal decrease is almost linear in all cases. The difference in time τ

$$\tau = t_1 - t_2 \tag{4.4}$$

between these two times gives an indication on the steepness of the signal slope. The bigger τ is, the longer it takes to form nuclei and to get into a stable growth regime where supply and incorporation/desorption of Ga do not change anymore over time.
This determination of τ was carried out for all doped and undoped samples grown at different T_S. In Fig. 4.3, the data is presented in an Arrhenius plot in order to determine the nucleation energy as discussed in more detail by Consonni *et al.*[123]. Throughout the whole T_S growth window (760 °C − 806 °C), the nucleation speed of the GaN:Mg samples is consistently higher. Moreover, the exponential fit of the respective Arrhenius plot yields a lower nucleation energy barrier for GaN:Mg of 3.2 ± 0.3 eV compared to the one for GaN of 4.0 ± 0.3 eV (see section 2.4).
It is evident from the difference in the nucleation energy that GaN:Mg is less sensitive to temperature change than pure GaN. This observation and the enhanced nucleation rate suggest that Mg acts as a stabilizer for the forming nuclei. Lymperakis *et al.* asserted that stoichiometric non-polar GaN surfaces are intrinsically unstable against atomic N and therefore Ga ad-atom incorporation events are more probable on the c-plane surface.[141] This balance might shift with Mg acting as a stabilizer for N atoms allowing a higher lateral growth rate and more rapid nucleation. Such an effect could also explain the enhanced lateral growth rate observed in this study and elsewhere.[150,166]

4.1.2. Growth

This subsection reports on the effect of Mg on the morphology of GaN NWs as well as on the effects that an additional variation of T_S has on such NWs. In general an additional supply of Mg to the growth of GaN NW results in an enhanced radial growth rate which in turn causes more coalescence compared with NW grown without Mg supply (compare previous section 4.1.1).[150,166] This effect can be seen in Fig. 4.4.
Due to the fact that the growth of GaN NWs takes place in N-rich conditions their growth rate is Ga limited for longer growth times. Thus, the enhanced radial growth has also an influence on the axial growth rate through the consumption of Ga. Mg doped GaN NWs grown for 3 h were found to be 150 nm smaller than their 1.31 µm long undoped counterparts. Apart from the Mg supply the growth conditions were identical.
The coalescence caused by Mg doping is an undesired effect, as it can lead to structural defect in the NWs, which are otherwise free from extended defects.[50] This is always a concern when dealing with Mg doping. The problem becomes even worse when relatively low T_S are chosen. These lower T_S might enhance the Mg incorporation as it is less likely to re-evaporate from the surface again, giving it more time to be included in the

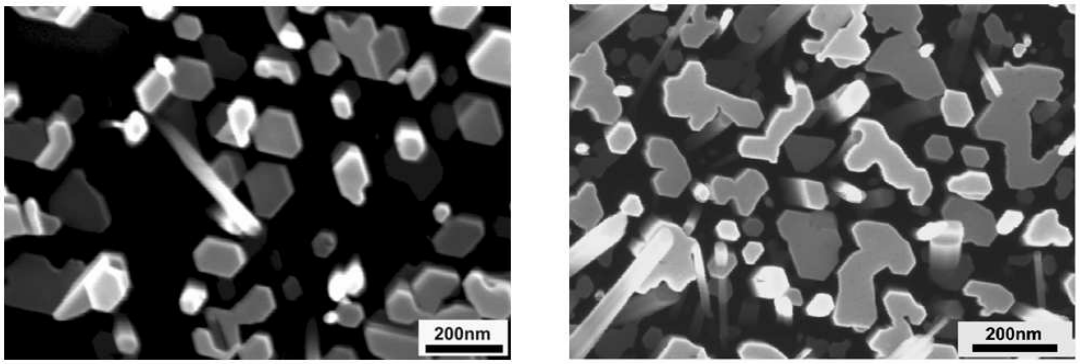

(a) (b)

Figure 4.4: SEM top view image of GaN NWs a) grown without an additional Mg supply (coverage $\approx$ 50%) and b) with Mg supply (coverage $\approx$ 77%).

GaN matrix.

The GaN NWs used for this study were grown on Si(111) substrates in nitrogen rich conditions (Ga/N $\ll$ 1). The silicon substrates were cleaned before epitaxy by a standard ex-situ chemical cleaning procedure and by in-situ annealing in ultra-high vacuum at 925 °C for 15 min, in order to obtain an oxygen-free surface with a 7 $\times$ 7 reconstruction. A low Mg doping level was chosen in order to minimize the impact of doping on the NW morphology and the structural properties.[167] The Mg cell temperature was T_{Mg}=185 °C resulting in a BEP of $\mathrm{BEP_{Mg}} = 1 \cdot 10^{-9}$ mbar. An Ga equivalent growth rate of 0.7 nm/min, a growth duration of 2h, a nitrogen flow rate of 4 sccm and an RF-power of 500 W (N equivalent growth rate: 15 nm/min) were used. The influence of the substrate temperature on the morphology was investigated for samples grown at different T_S between 665 °C and 785 °C.

SEM birds-eye view images of the as grown samples were used to determine diameter and length distributions. Top view images were used to evaluate the density of the NWs. In Fig. 4.5 SEM birds-eye view images are presented for four of the Mg doped samples. The NW samples exhibit roughly four distinguished morphology regimes. At lower growth temperatures (665 °C to 685 °C), an almost compact layer with a height of approximately 570 nm is formed. It is not clear whether this layer consists of coalesced NWs or actually grows directly as a layer. Out of it, a few rather long wires emerge (Fig. 4.5a)). In the intermediate temperature range from 725 °C to 755 °C a trimodal NW growth mode is observed (compare section 3.1). The length of most wires was found to be around 600 nm with an average diameter of about 60 nm. A number of thin NWs are observed that exhibit a much higher aspect ratio. A third class of NWs is present, these wires have a length below 400 nm and small diameters below 40 nm. This can be seen in the histogram of Fig. 4.6a) where the peak around 600 nm in length (shaded in red) represents the first class of wires, while the counts at 850 nm and above originate from the wires with an increased aspect ratio (shaded in blue). At elevated T_S (785 °C) the NWs are well separated and show a narrow quasi-cylindrical shape and no obvious faceting. At even higher temperatures a significant decrease in diameter, length as well as density (results not shown here) is observed, due to an increased Ga desorption as well as GaN decomposition.[115]

The average length for each class of the trimodal NW distribution has been calculated

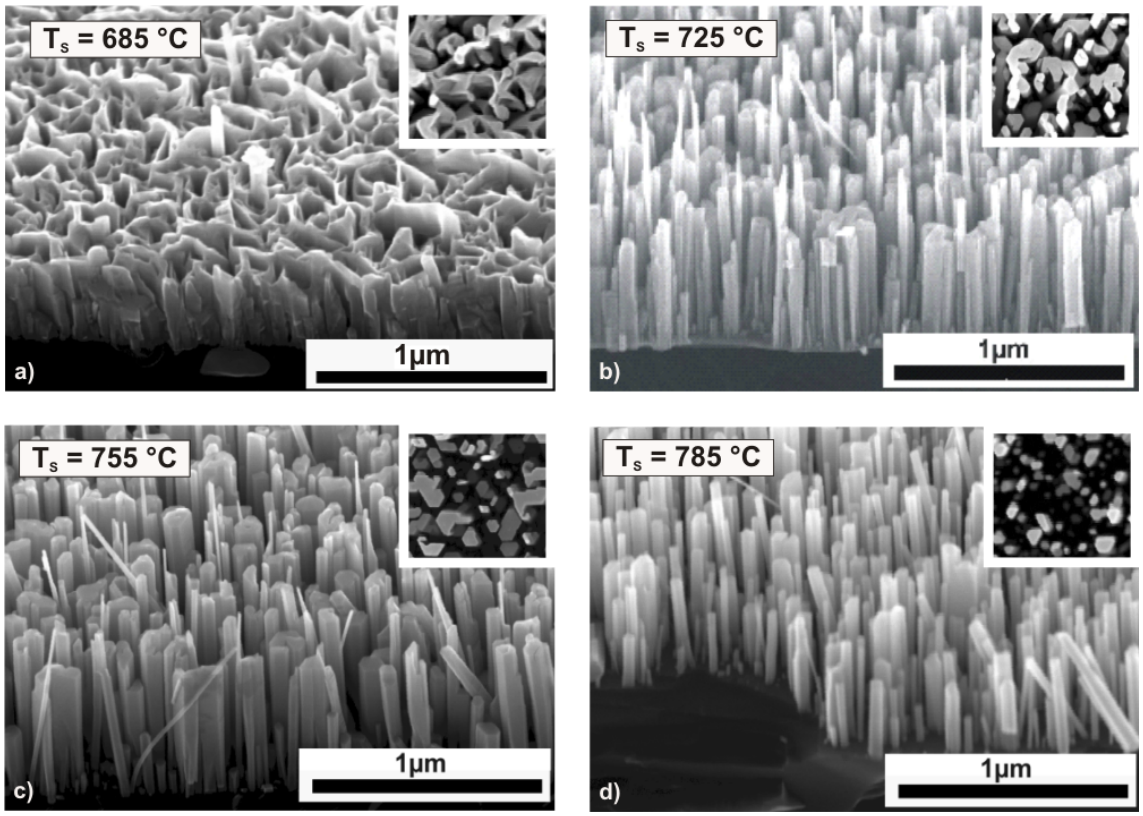

Figure 4.5: a) – d) SEM birds-eye view images (tilt = 45°) of GaN:Mg NWs grown at different temperatures T_S. The insets are top view SEM images of the corresponding samples at the same magnification containing 26, 32 and 46 wires for the insets b), c) and d), respectively. The number of wires in the inset of a) cannot be evaluated as it is an almost compact layer.

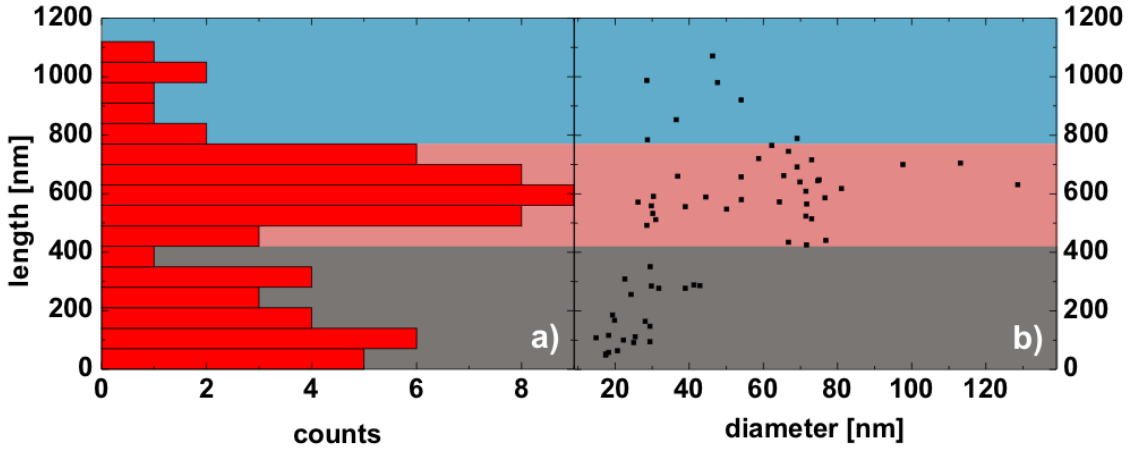

Figure 4.6: a) Histogram of the length of NWs found for T_S = 725 °C. b) Diameter and length correlation for the same data set. The color code indicates the trimodal distribution.

for all the samples (shown in Fig. 4.6a)). The length of the wires in the different classes is slightly decreasing as a function of substrate temperature as can be seen in Fig.4.7a). This

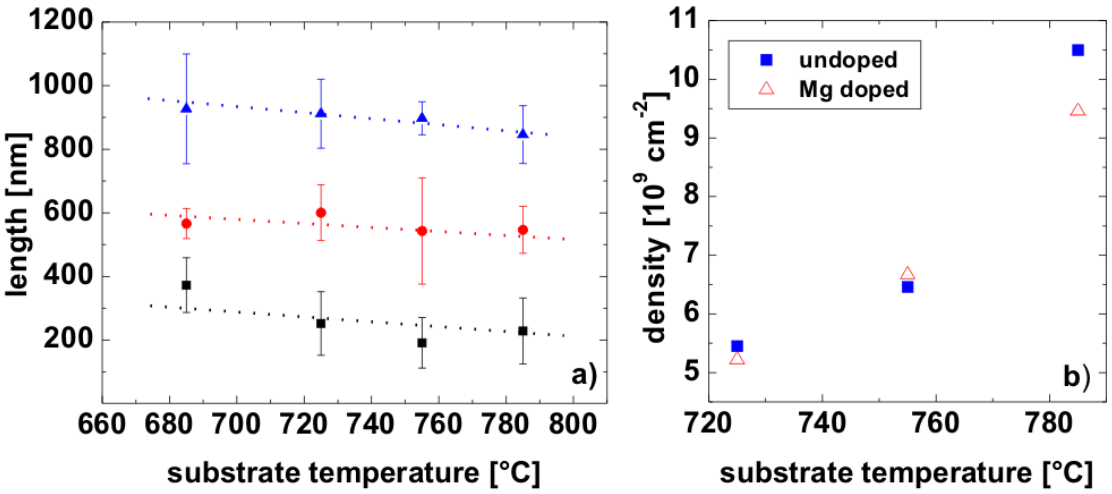

Figure 4.7: a) Average length for each wire class as a function of temperature. The error represents the standard deviation, the dashed lines are guides to the eye. The colors used represent the three wire classes in their respective shadings which can be seen Fig. 4.6. b) Density of wires as a function of substrate temperature. The data points are calculated from SEM images showing an area of 4 μm^2.

behavior might be explained by the increase of the Ga desorption rate at higher growth temperatures.
We can identify a suitable temperature window (725 °C − 785 °C) for the growth of Mg doped GaN NW, using as the only criterion the best quasi-cylindrical morphology. The lower limit of the substrate temperature for the used growth parameters is defined by the formation of an almost compact layer at $T_S \leq 725$ °C, and the upper limit is determined by the Ga desorption rate which becomes the dominating process at $T_S > 800$ °C.
The NW density increases with T_S within the temperature range of 725 °C − 785 °C, as can be observed in the top view SEM images shown as insets in Fig. 4.5a)−4.5c) and is numerically shown by the statistical data in Fig. 4.7b) calculated from SEM images of 4.0 μm^2 areas. The density amounts to $5.5 \cdot 10^9$ cm^{-2} at T_S = 725 °C, whereas it increases to $9.5 \cdot 10^9$ cm^{-2} at T_S = 785 °C. This effect is due to a reduction of the NW coalescence at higher temperatures because of the enhanced diffusion of Ga ad-atoms toward the NW top, and results in a reduction in lateral growth rate with respect to the vertical one.[126] While at lower temperatures the difference in density between doped and undoped samples is negligible, it is more pronounced at T_S = 785 °C. This is caused by a stronger tendency of coalescence for doped wires (see also Fig. 4.1). Thus at this high temperature not only the best morphology but also the highest NW density can be reached.
TEM measurements were performed, in order to investigate the effect of coalescence on the structural properties of the GaN:Mg NWs. These NWs show few extended defects. The TEM image in Fig. 4.8 shows the bottom of a typical Mg-doped nanowire. Those defects which are observed are induced by the coalescence of wires and are present close to the base of the NWs, but once the coalescence is complete (within 20−30 nm) the wires grow without visible morphological defects.[50] Stacking faults or zincblende type insertions, as reported in the case of higher Mg supply,[167] were not observed in our samples.

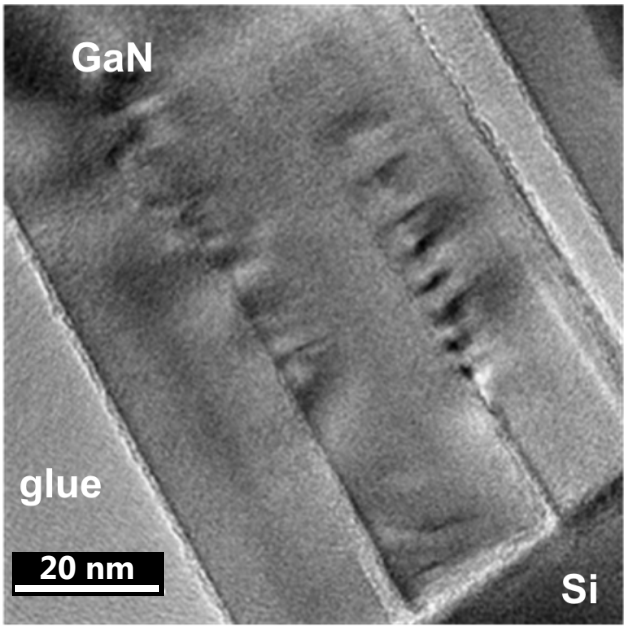

Figure 4.8: TEM image of the bottom part of a Mg-doped GaN NW. The coalescence of formerly three wires is completed within a few 10 nm and the strain caused by the interfaces is relaxed at a similar length scale. The data was acquired by E. Sutter, Brookhaven National Laboratory.

4.1.3. Optical properties

Optical investigations, such as Raman measurements and PL, can yield insights into the crystal quality, defects and even the electronic properties of a material. Especially for doping investigations these are powerful techniques as a dopant is a perturbation of the ideal crystal. In this section, both Raman and PL investigations of the samples described in the previous section are conducted. In order to gain a Raman signal free from the influence of the Si(111) substrate, the NWs were mechanically removed from the growth substrate and transfered to a glass substrate. NWs prepared in this way are named free standing NWs (FSNW) as they are not influenced by the growth substrate anymore. In fact the wires are not entirely free standing as they have a tendency to form clusters of a few 10 NWs aligned in parallel. An additional benefit is the reduction of the number of selection rules, which need to be fulfilled, as the NW clusters are randomly oriented. Raman spectra for Mg doped FSNW are shown in Fig. 4.9a) together with peak positions of different vibrational phonon modes in GaN taken from Harima.[168] An intense and sharp E_H^2 peak with a full width at half maximum (FWHM) of $3.15\,cm^{-1} - 4.15\,cm^{-1}$ can be seen in all spectra, as well as a strong A_1(TO) peak. The E_1(TO) peak is weakly pronounced as a shoulder of the E_H^2 peak.

Besides these phonon modes of GaN two additional broad peaks of unclear origin can be observed within the range of $400\,cm^{-1} - 500\,cm^{-1}$. The peak around $420\,cm^{-1}$ might be attributed to a vacancy related defect mode.[168,169] Furthermore, a weak Raman signal is present in the spectra of FSNWs from the Mg doped samples grown at 785 °C and 725 °C (peak at $520\,cm^{-1}$). This signal originates most likely from Si particles which have remained attached to the NW clusters despite their removal from the growth substrate.
The Raman spectra of the undoped reference samples are given in Fig. 4.9b). They show the same characteristics as the spectra of the Mg doped samples described above. Addi-

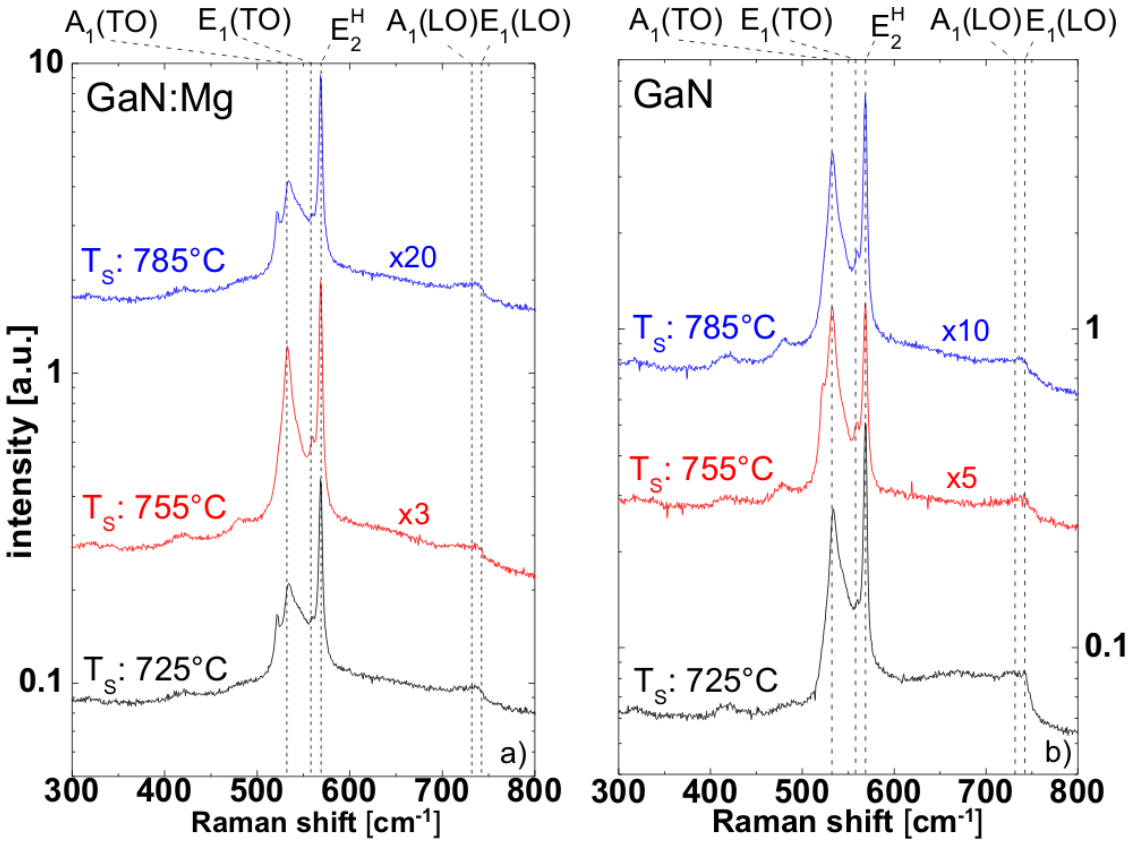

Figure 4.9: Raman graphs of a) Mg-doped and b) undoped GaN NWs grown at three different temperatures. The positions of the Raman peaks shown here as vertical dotted lines were taken from Harima.[168] The data was acquired by E. O. Schäfer-Nolte, Forschungszentrum Jülich.

tionally, a broad peak can be found close to the position of the longitudinal optic Raman modes (LO). However, quantitative differences between Raman spectra of doped and undoped NWs can be detected. The A_1(TO) peak intensity normalized to the E^2_H mode is reduced for the doped sample compared to their undoped counterparts. This is due to the polar character of the A_1(TO) mode, therefore it is more sensitive to changes in the carrier concentration. The sharpness of the E^2_H which gives information about the crystalline quality is enhanced by Mg doping as will be discussed later on associated with the PL results.

Harima studied Mg doped GaN films and found significant changes in the Raman spectra for increasing hole concentrations.[168] They observed a low frequency (< 300 cm^{-1}) continuum band arising from light scattering of free holes and a vibrational mode at 657 cm^{-1}, which was attributed to a Mg−N vibration. The fact that none of these features could be observed in the spectra of our Mg doped NWs is a confirmation that the Mg concentration in these nanowires is low. Also in energy dispersive x-ray spectra (EDS), acquired from isolated NWs in a TEM with a 10 nm spot size, no Mg signal was found. This is expected though, as EDS is only sensitive to material content above a few atomic % and therefore only well beyond doping levels.

The PL spectra for doped and undoped GaN NWs grown under the same conditions at T_S =785 °C, 755 °C and 725 °C are shown in Fig. 4.10. The major difference that can

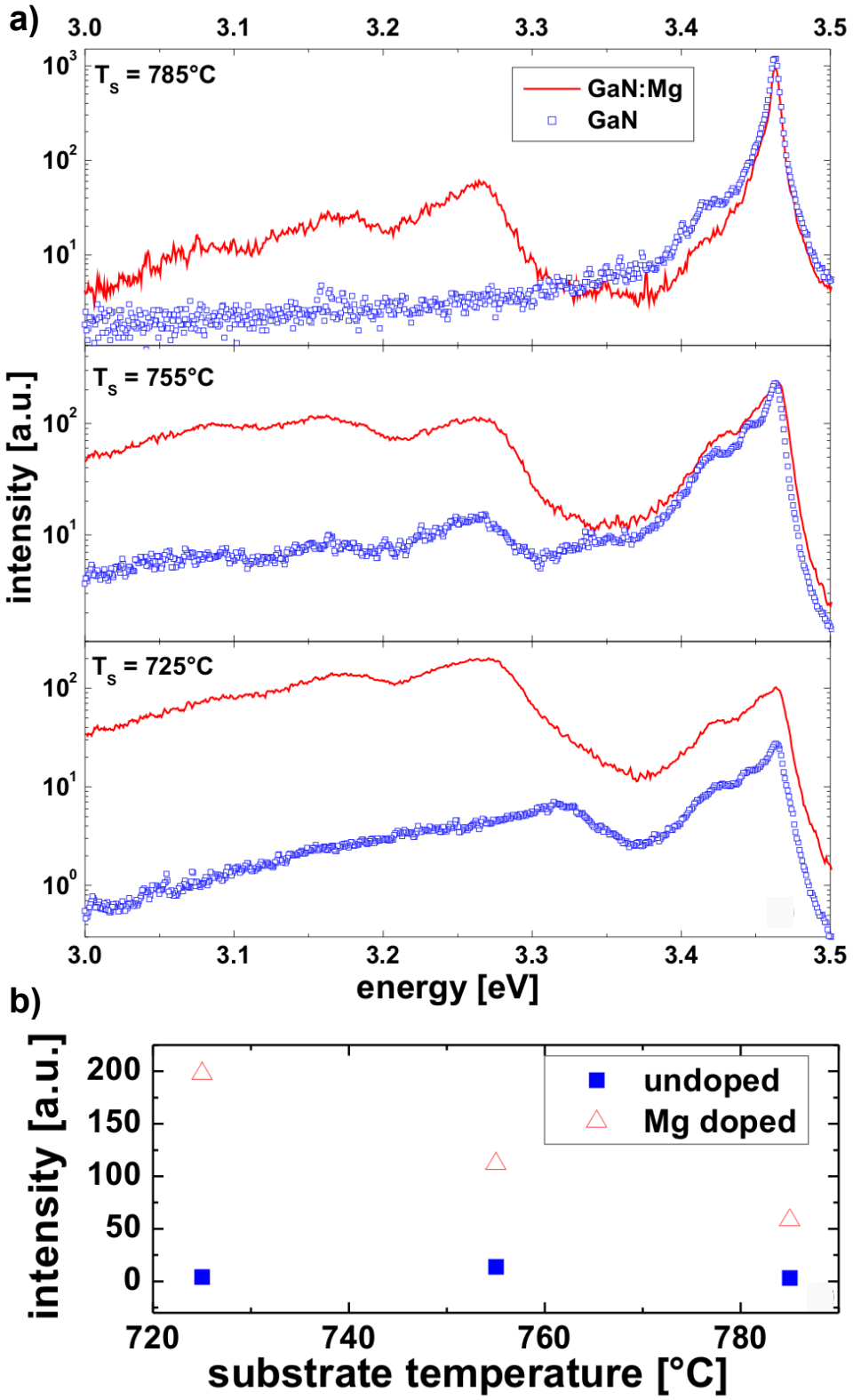

Figure 4.10: a) PL spectra of doped NW samples (red lines) and undoped NW samples (blue squares) at different T_S. b) PL intensity at 3.26 eV for all samples displayed in a).

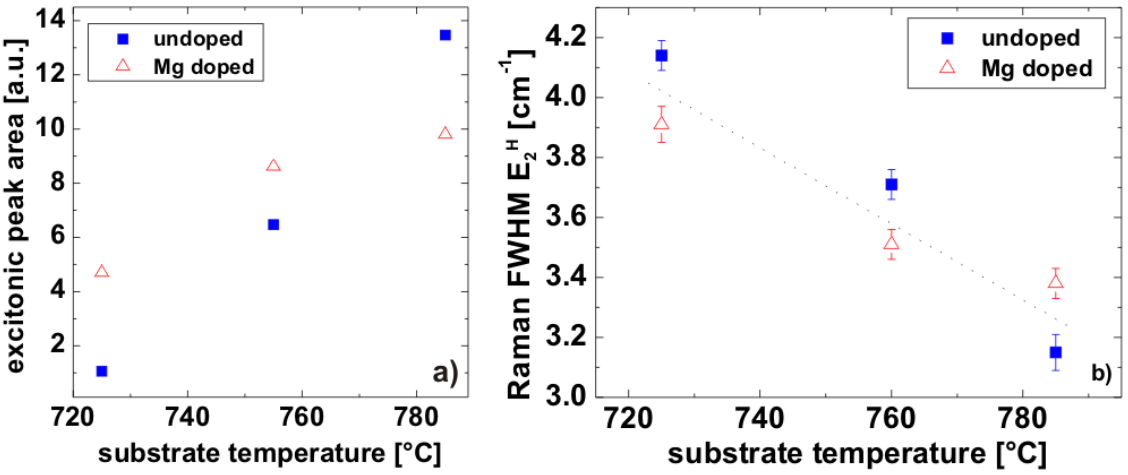

Figure 4.11: a) Integrated signal of the excitonic peak of doped and undoped NW samples between 3.37 eV and 3.55 eV at different substrate temperatures; b) FWHM of the E_H^2 Raman mode of doped and undoped NW samples at different T_S, the dashed line is a guide to the eye only. The Raman scattering data was acquired by E. O. Schäfer-Nolte, Forschungszentrum Jülich.

be observed between Mg doped and undoped NWs is a strong enhancement of the UV luminescence band between 3.00 eV and 3.26 eV. This luminescence is assigned to DAP transitions and their phonon replica (red shifted by 92 meV).[48,166,170]
The relative intensity of the UV band with respect to the near band edge peak, in the PL signal of the samples grown at different T_S, is increasing as T_S is decreasing. Since undoped GaN NWs show an unintentionally n-type doping[171] the increase in the UV-band ascribed to a DAP transition is most likely due to an enhanced concentration of acceptor states caused by the Mg dopant.[28] As pointed out by Reshchikov *et al.*[48] the PL spectra within the DAP range have also a contribution from a broad emission (peak at 2.95 eV) associated with defects. This broad peak is increased at lower deposition temperatures and partially covers the DAP contribution.
For a given T_S, the intensity of the onset peak of the UV-band at 3.26 eV with respect to the excitonic peak is significantly modified by Mg incorporation into the wires and can be used as a measure of Mg incorporation. However, the evaluation procedure proposed here using the DAP peak cannot be used to compare samples obtained at different T_S, because additional effects like for example the temperature dependence of the unintentional donor state formation and the defect band at 2.95 eV also effect the PL spectra in the DAP energy range. The luminescence intensity of the UV band as a whole in doped wires increases for lower T_S (see Fig. 4.10b)). Its relative intensity compared to the near band edge peak of both doped and undoped NWs behaves likewise. The reduction in T_S causes a broadening of the exitonic peak at 3.47 eV (Fig. 4.10a)) and a decrease in total luminescence efficiency (Fig. 4.11a)) due to degradation in material quality. As one can see from Fig. 4.11a), the efficiency of the excitonic emission is increased by Mg incorporation at low temperatures.
On the contrary, at high deposition temperatures, the efficiency is reduced in Mg doped samples. Therefore one can conclude that apparently the crystal quality of the NWs is improved at low deposition temperature by Mg doping and it is reduced for high tem-

peratures relative to the undoped case. The additional disorder due to doping could explain the reduction of the crystal quality at high temperature. At low temperatures, as discussed above, Mg doping results in a stronger coalescence,[166] and thus many bulk-like single crystal columns with bigger diameter are formed. The increase of the crystal size, which has a benefit for the optical efficiency, may overcome the effect of the doping-induced disorder. These results are in agreement with Raman measurements. The FWHM of the E_H^2 Raman peak decreases with T_S for both doped and undoped NWs, showing an increase of the crystal quality at higher temperatures (Fig. 4.11b), data extracted from Fig. 4.9). The effect Mg incorporation has on the FWHM of the E_H^2 Raman peak is similar to the one on the PL measurements (Fig.4.11b)). Resulting in lower FWHM values for doped samples at low temperatures, which corresponds to a better crystal quality, while at higher temperature a reverse effect is observed.
In summary one can say that PL holds the potential to give information on the Mg incorporation through the DAP transition, while the information gained by Raman measurements is very limited, especially regarding the Mg doping level.
Overall none of these optical measurements has the potential to confirm that true p-type material was achieved, this can only be proven by electrical measurements (see chapter 6).

4.2. Silicon doped GaN nanowires

Si is known to act as a donor in GaN when it is incorporated on a Ga site. It is therefore used for n-type doping. Unintentionally doped GaN has been observed to be n-type.[13,28] Additional Si doping can enhance the carrier densities to levels desired for a specific device application.[28] It is therefore necessary to investigate how to control Si doping and what its effects are on the NW growth mechanism. The optimal setting of the Si effusion cell for the creation of the n-type segment of a NW LED is determined.

4.2.1. Determination of the Si doping level

The first challenge of doping NWs in general lies in the determination of the doping concentration. Various methods have been developed for the characterization of thin films in this respect[51] but most of them are not applicable for NWs. To this day, no reliable and fast method has asserted itself. For this reason, an indirect approach to determine the doping level in the grown GaN NWs is initially chosen.
To calibrate the Si effusion cell a superlattice of planar AlGaN and GaN layers was grown. The Si concentration in the GaN layers was varied by supplying more Si during the growth of each GaN layer. The AlGaN acts as a marker layer (see Fig.4.12a)). In the cross section SEM images in Fig. 4.12b) and c), the AlGaN marker layers and the GaN:Si test layers can be differentiated by their different material contrasts.
This superlattice structure was investigated by secondary ion mass spectrometry (SIMS), a standard method for the determination of doping levels in semiconductor layers.[51] In the SIMS data plotted in Fig. 4.13, the Al signal clearly allows the identification of the position of the five AlGaN marker layers. The valleys of the Al signal represent the position of the GaN:Si probe layers. Each of these valleys in the Al signal coincides with a peak in the Si signal. This peak value is now taken as the Si concentration in the corresponding Si doped GaN layer being probed.
Plotting these values versus the Si effusion cell temperature in Fig. 4.14 one can fit the

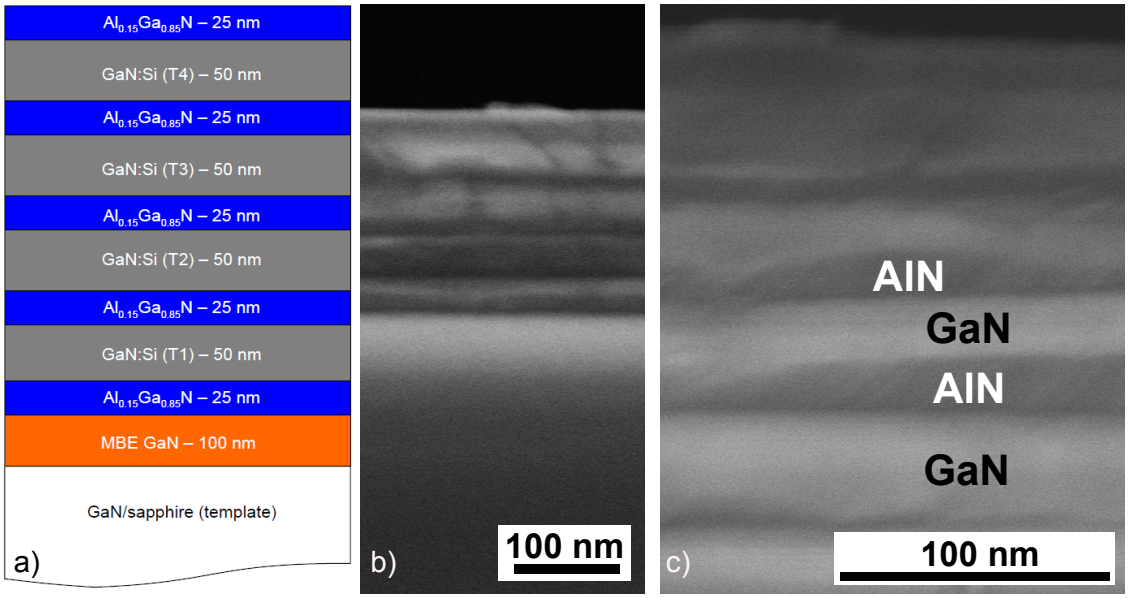

Figure 4.12: a) Sketch of the design of the structure with AlGaN marker barriers and GaN layers with different Si doping concentrations. Also, SEM cross section images of the grown superlattice in b) low and c) high magnification.

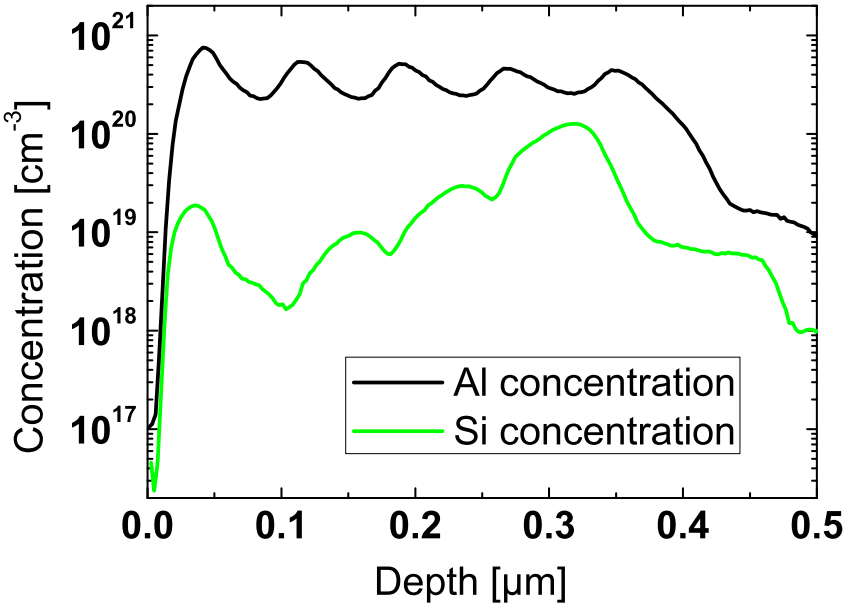

Figure 4.13: SIMS data for Al and Si plotted as a function of the sputtering depth. The data was acquired by RTG Mikroanalyse GmbH, Berlin

data with an exponential function. This is expected as the evaporation of Si from the cell is a thermally activated process. The best fit for the displayed data is achieved with the function:

$$c_{\mathrm{Si}}(T_{\mathrm{Si}}) = 1.2 \cdot 10^{10}\,\mathrm{cm}^{-3} \cdot \exp\left(\frac{T_{\mathrm{Si}}}{52\,^{\circ}\mathrm{C}}\right) + 4.7 \cdot 10^{16}\,\mathrm{cm}^{-3} \tag{4.5}$$

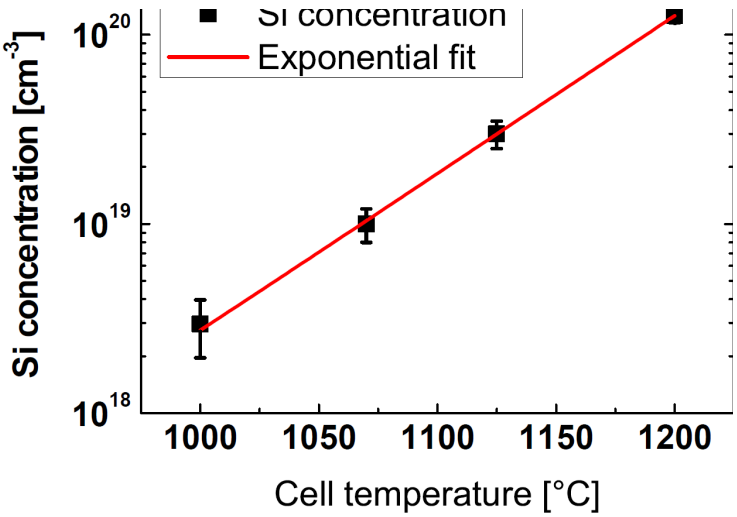

Figure 4.14: The Si concentrations of the GaN layers is plotted as a function of the Si cell temperature and fitted with an exponential function.

The slope of the log plot in Fig. 4.14 is $(0.0192 \pm 0.0004) \cdot T_{\mathrm{Si}}$. This allows the calculation of the supplied Si flux during NW growth at any given Si cell temperature T_{Si}. Taking into account that the NWs cover only roughly 55% of the substrate surface (compare for example Fig. 4.4a)), yet have a higher growth rate compared to GaN layers[138] one can calculate the volume of GaN grown in a given time unit. Assuming an incorporation of all the supplied Si into the NWs, the Si doping concentration c_{Si} can be estimated by comparing this volume to the volume of a GaN layer grown in the same unit of time. The estimates are presented in table 4.1. These values have to be understood as estimates

T_{Si} [°C]	c_{Si} [cm^{-3}]
1000	$4.5 \cdot 10^{18}$
1100	$3.0 \cdot 10^{19}$
1200	$2.0 \cdot 10^{20}$
1300	$1.4 \cdot 10^{21}$

Table 4.1: List of the nominal doping concentration in GaN NWs at a given Si cell temperature.

only, as there has been no verification by another direct measurement method. Also the assumption that all the supplied Si is incorporated is not necessarily valid. These values can only provide guidance on the order of magnitude at which the doping concentration may be found. Throughout the remainder of this section the cell temperature T_{Si} will be used to distinguish the doping concentrations of the NWs for these reasons, as the errors in providing a number for c_{Si} would be rather huge.

4.2.2. Growth behavior

The supply of an additional atomic species will influence the growth behavior of the NWs, due to the nature of the growth mechanism employed for the synthesis in this scope. In this section, the influence of an additional Si supply is discussed. The observa-

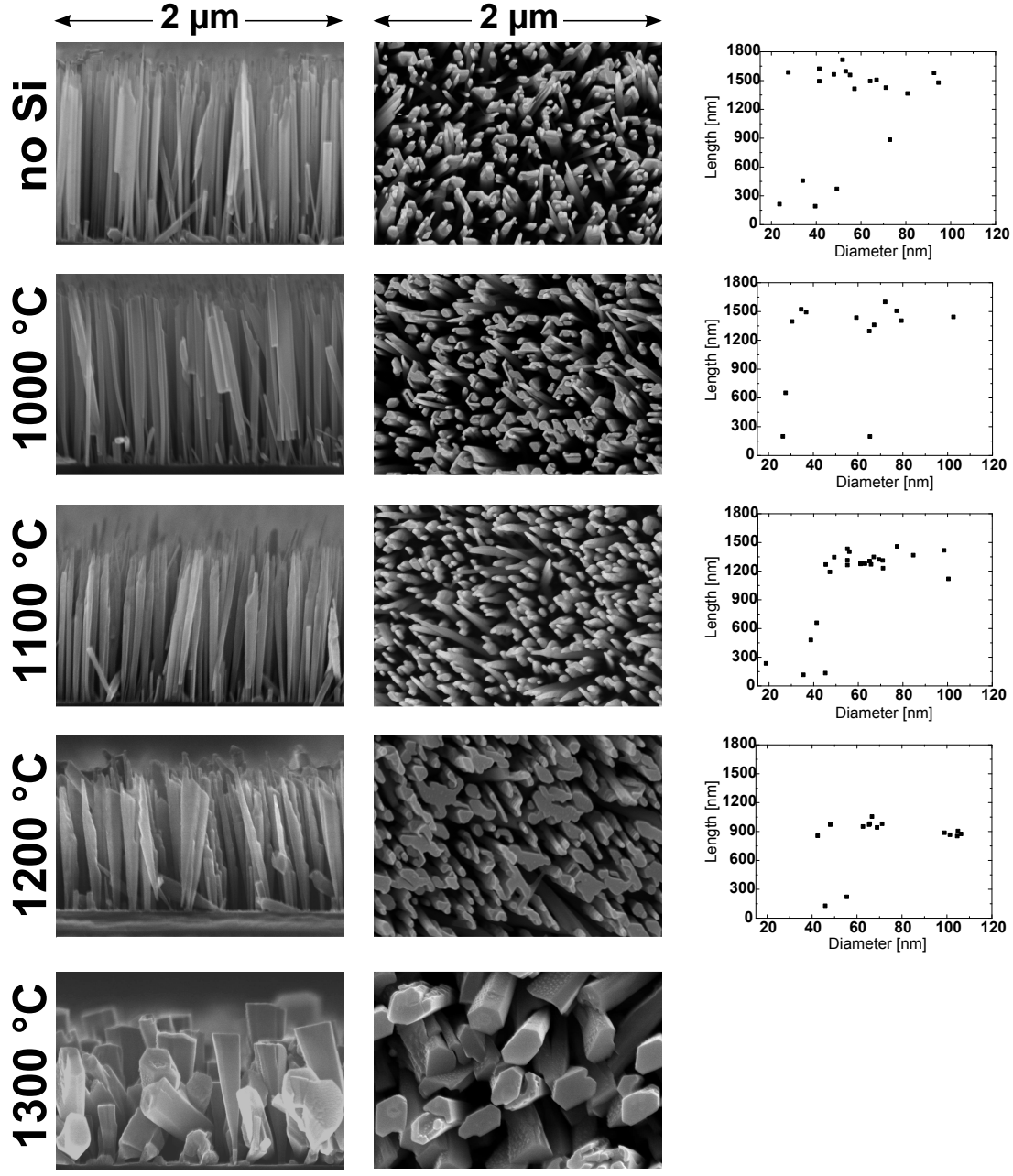

Figure 4.15: SEM cross section and top view images of NW with different doping concentrations are shown along with the L-D plots extracted from the cross section images.

tions are presented in Fig. 4.15. The first finding is the broadening of the NWs towards the top, which takes place as the Si flux is increased. This can be clearly seen from the SEM cross section images on the left hand side of Fig. 4.15. It is also obvious in the top view images where the wire top facets cover more area at high Si fluxes. In addition to this, the NWs lose their perpendicular orientation with respect to the substrate at the highest Si flux (T_{Si} = 1300 °C). At this T_{Si} also small drops can be seen on the wire side facets which may be agglomerates of Si or a mixture of Ga and Si.
As the Si flux increases the NW height decreases. This can be seen in the length versus diameter plots (L-D plots) as well as in the SEM cross section images (see Fig. 4.15). For

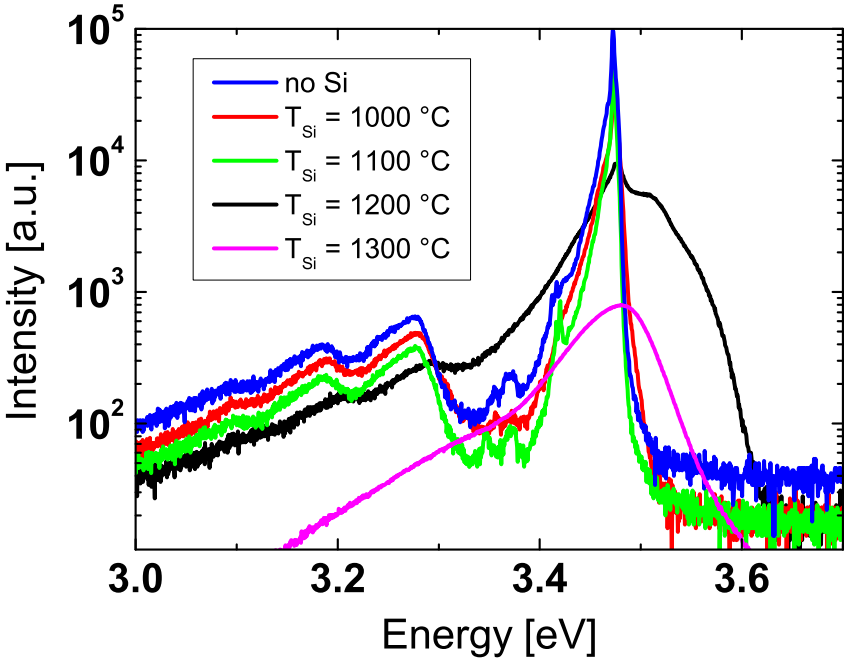

Figure 4.16: PL spectra of GaN NWs with different Si doping concentrations acquired at 10 K. The data was acquired by C. Pfüller, Paul-Drude Institut für Festkörperelektronik, Berlin.

the highest Si flux no L-D diagram was produced due to the difficulty of assigning a diameter for wires that show a strong broadening.
Overall, one can say that the wires grown with an addition Si flux of up to T_{Si}=1100 °C still retain their NW morphology and do not show significant tapering. At the same time, their doping concentration, as estimated in table 4.1, should already be significant.

4.2.3. Optical properties

In order to investigate the Si doped NWs further, PL and Raman scattering investigations were conducted. These two methods allow qualitative insight into the crystal quality and the effects of doping atoms.
In Fig. 4.16, the PL spectra of the samples presented in Fig. 4.15 are shown. The dominant feature at 3.47 eV is the NBE peak of GaN which in turn is dominated by DBE transitions (see also section 3.2).[48,172] In the range between 3.0 eV and 3.26 eV, the DAP signal is visible which is present in most NW samples synthesized in the machine at the Paul-Drude Institut due to the memory effect of Mg, used in previous growth runs.[173] This signal is generated by the Mg incorporation and does not yield information about the Si doping of the NWs (see section 4.1.3).
Initially, the FWHM of the NBE peak shrinks due to Si doping. This could be explained by an increased dominance of the DBE transition. Once T_{Si} is increased above 1100 °C a strong difference can be observed. The NBE peak is significantly broadened which can be assigned to tailing of the density of states, caused by potential fluctuations due to randomly distributed impurities.[174,175]
The Raman spectra acquired from the Si doped NWs are shown in Fig. 4.17. The very

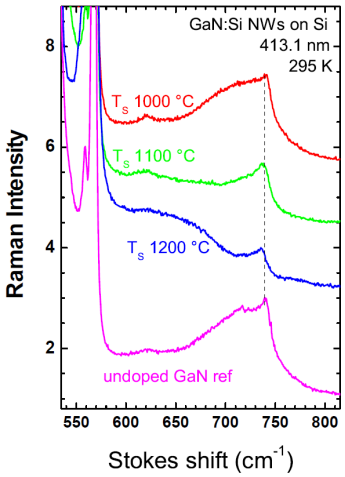

Figure 4.17: Raman spectra of GaN NWs with different Si doping concentrations acquired with 413 nm excitation at 295 K. The data was acquired by M. Ramsteiner, Paul-Drude Institut für Festkörperelektronik, Berlin.

intense peak at 568 cm^{-1} present in all spectra originates from the Si substrate and can be safely ignored. All sample have a peak at around 739 cm^{-1} which can be assigned to LO phonon transitions in GaN.[168,176,177] Both, the undoped reference and the sample with the lowest Si supply exhibit a broad peak between 680 cm^{-1} and 750 cm^{-1}. This transition is usually associated with surface optical phonon modes.[178–180] These modes appear frequently in NWs as they poses a high surface to volume ration. It is not clear whether the broad shoulder between 600 cm^{-1} and 690 cm^{-1} in the spectrum obtained for the NWs with T_{Si}=1200 °C is also associated to such surface modes. Begum *et al.*[178] describe a shift to lower wavenumbers with a decrease in correlation length (length describing the median distance from one defect to another). Such a decreased correlation length would be expected for higher doping concentrations. Yet, it is not clear why no such signal is found in the NWs grown with T_{Si}=1100 °C. In none of the spectra coupled plasmon-LO-phonon modes were found. These modes would give directly insight into the carrier concentration variation due to the different doping conditions.[181]
In summary, the PL data suggests that a Si cell temperature of T_{Si}=1200 °C is the level at which the optoelectronic properties of the GaN:Si NWs start to deteriorate significantly. Raman measurements signal little change in the properties of the NWs if T_{Si}=1000 °C is supplied. Higher Si fluxes clearly have an influence on the Raman spectra. The detailed interpretation of these changes are subject of ongoing investigations.

4.2.4. Electrical properties

In order to test the effectiveness of the Si doping on the electrical properties of the Si doped GaN NWs, two methods were employed. The first method (ensemble contacting) is oriented towards the final integration of the NWs into a working ensemble device. The other enables the extraction of data on a single wire basis (nanotip measurements). At first, the ensemble method and it results will be described followed by the discussion of the nanotip measurements on a few or even single wires.

For a measurement of the conductivity of the GaN:Si NWs, a piece of the as grown

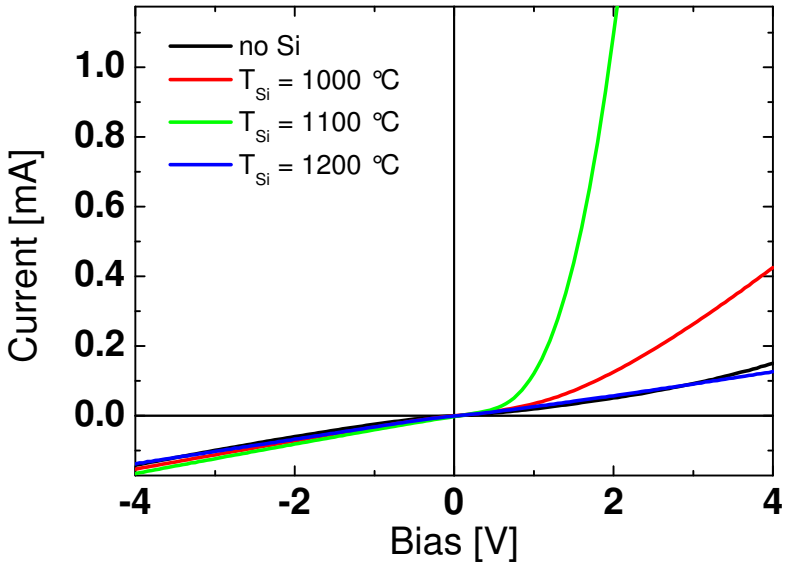

Figure 4.18: I-U characteristic of ensemble contacted GaN:Si NWs.

wafer was cleaved of and planarized by spin coating a solution of hydrogen silsesquioxane (HSQ) resin.[182] This solution is transformed into an amorphous SiO_x by thermal annealing in air at 350 °C for 30 min. This step was repeated several times, for a detailed description see section 6.2. After uncovering the NW tips by RIE, contact pads were lithographically defined through the metalization of the NW ensemble with a Ti/Al/Ni/Au (20 nm/ 20 nm/ 40 nm/ 80 nm) layer.[183,184] The Si substrate acted as a back contact. These samples were then contacted in a probe station and I-U characteristics were recorded. Several contact pad diameters were tested.
Some representative characteristics are displayed in Fig. 4.18. The Schottky diode formed between the wires and the metal contact displays a rectifying behavior with varying conductivity under forward bias for the differently doped NWs. The highest conductivity is obtained for the wires experiencing a Si flux from the 1100 °C hot effusion cell. Also in this analysis, the material with this doping concentration seems to be best suited for the use in a NW device.
Aside from the conductivity analysis, the photo sensitivity of the device was tested. All NW devices produced in this way did show a response to ambient light. In Fig. 4.19 the current I is plotted under various lighting conditions at a fixed forward bias of 1 V. As the top contact metalization is rather thick in these cases, the signal most likely originates only from the rim of the contact pads. For this reason, the signal is also rather weak and no spectrally resolved photo current measurements were conducted. Nevertheless, a photo response can be detected indicating carrier generation through the incoming light. This means that the semiconductor NWs are contributing in a significant way to the I-U characteristic.
The second method, employed was the contacting of a few or even individual NWs with tungsten nanotips (W-nanotips). The samples were introduced into an SEM chamber equipped with a piezo-stage for the control of the W-nanotips. One tip was approached to the NW top facet and finally brought into contact. This allowed to drive a current through the NWs and the Si substrate which again acted as a back contact. The corresponding I-U characteristics can be seen in Fig. 4.20.

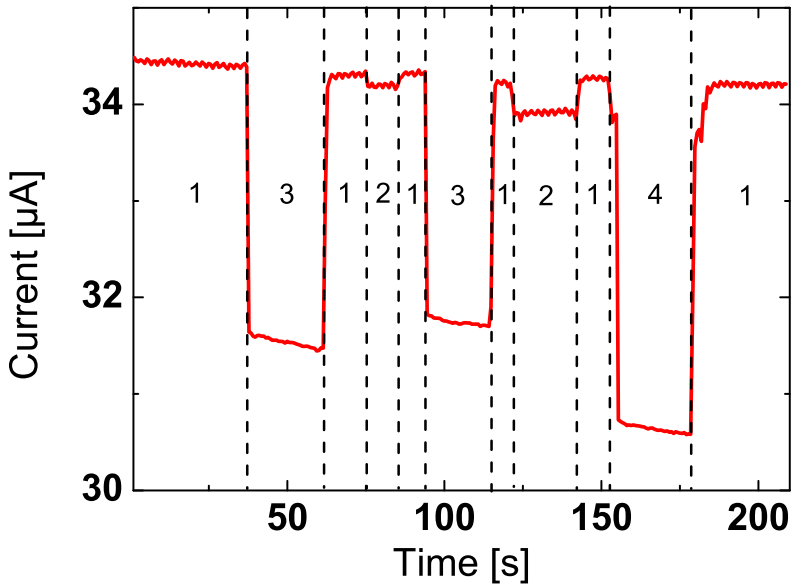

Figure 4.19: The current through the ensemble contacted GaN:Si NWs is plotted as function of time. The dashed lines mark the turning ON/OFF of surrounding light sources. State 1: Microscope light ON ceiling light ON. State 2: Microscope light OFF ceiling light ON. State 3: Microscope light ON ceiling light OFF. State 4: Microscope light OFF ceiling light OFF.

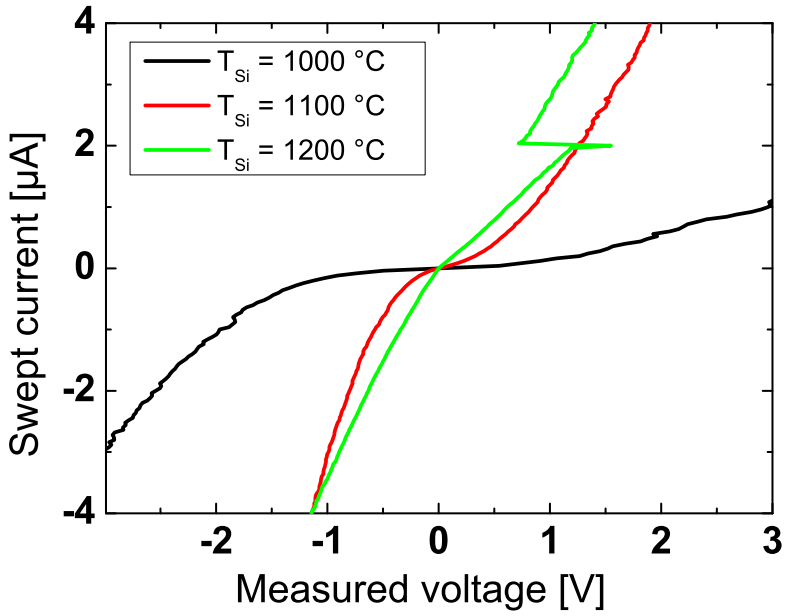

Figure 4.20: I-U characteristics of GaN:Si NWs contacted with a W-nanotip in an SEM. The data was acquired by J. Ledig, Technische Universität Braunschweig.

By determining the slope in the regime between -4 µA and -2 µA a resistance can be extracted (see Fig. 4.21). The smallest resistance is found for NWs grown with T_{Si} of 1100 °C.
Also this measurement confirms the previous results, namely the Si cell temperature of T_{Si}=1100 °C and the corresponding doping concentration, yield the best results with re-

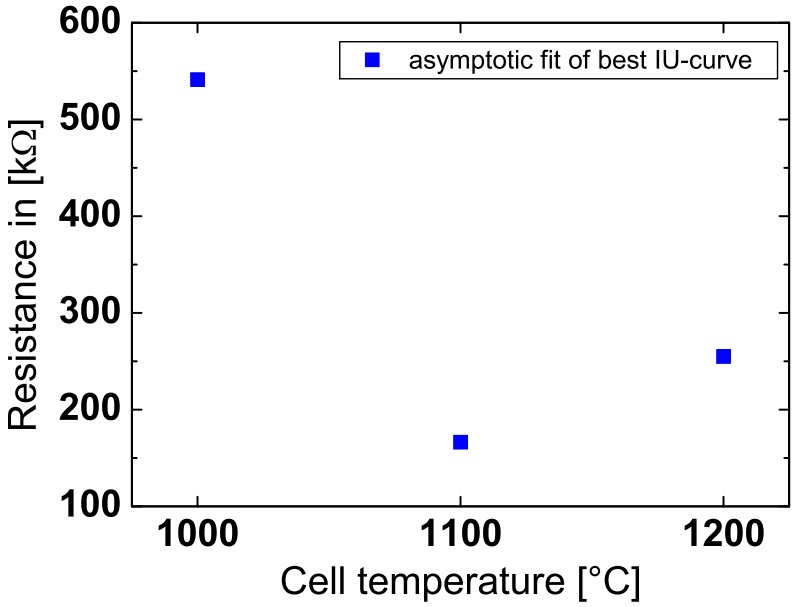

Figure 4.21: Resistances extracted from W-nanotip measurements. The data was acquired by J. Ledig, Technische Universität Braunschweig.

spect to the use in a NW LED structure. The morphology is not strongly influenced for this doping concentration. Also the optical properties are of similar quality as is the case for the not intentionally doped NWs and the electrical conductivity is the highest of all investigated samples.

4.3. P-i-n junctions

The utilization of NW structures in nano optoelectronics requires mastering both n- and p-type doping. The influence of Mg doping was discussed in section 4.1. Section 4.2 focused on the morphological, electrical and optical properties of GaN NWs doped with Si. Also other authors have been investigating effects related to Mg and Si doping in GaN nano structures.[118,150,164,166,170,171,185–187] Especially the p-type doping appears to be a crucial task and its careful control represents a major challenge. In this section, both n- and p-type doping will be combined to form nominal p-i-n juctions within single NWs. Si(111) substrates were cleaned before epitaxy by a standard ex-situ chemical cleaning procedure and by in-situ annealing in ultra-high vacuum at 925 °C for 15 min, in order to obtain an oxygen-free surface. An AlN buffer layer was fabricated prior to NW growth by nitridation of a thin Al layer deposited at a substrate temperature of T_S = 770 °C. Nitridation was performed for 4 minutes using an RF-power of P_{RF} = 500 W and a nitrogen flow rate of 4 sccm. Subsequently, T_S was ramped to the growth temperature of the GaN NWs (770 °C, 785 °C and 805 °C), which was performed using a Ga flux of 0.75 nm/min and the same nitrogen plasma conditions as for nitridation. For each T_S two doping sequences, one inverted with respect to the other, were fabricated: bottom GaN:Si (2 hours) / undoped GaN (30 min) / top GaN:Mg (2 hours) (samples denoted as type-A); upside down sequence: bottom GaN:Mg (2 hours) / undoped GaN (30 min) / top GaN:Si (2 hours) (samples denoted as type-B). For all samples, BEP_{Si} was set at $6.0{\cdot}10^{-10}$ mbar (T_{Si}=1050 °C) while both $0.5{\cdot}10^{-9}$ mbar and $2.0{\cdot}10^{-9}$ mbar were used as

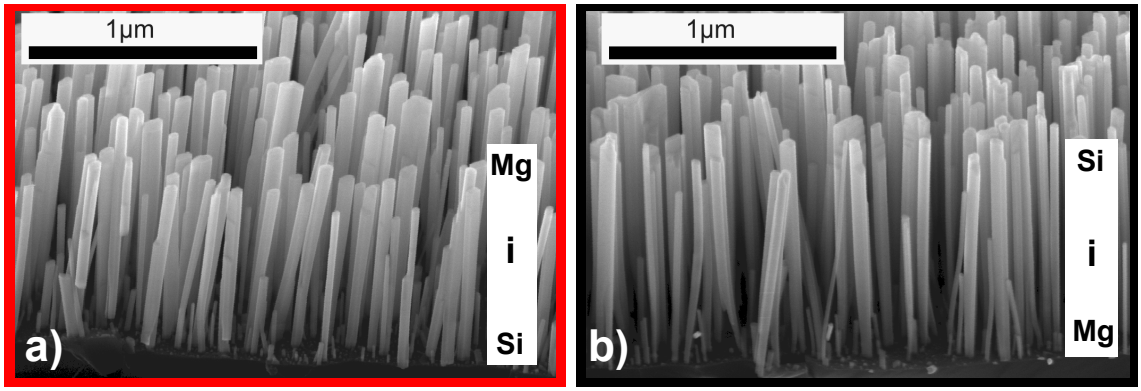

Figure 4.22: SEM birds eye images of GaN NWs with two different doping profiles a) type-A and b) type-B.

BEP_{Mg} (T_{Mg}=185 °C and T_{Mg}=230 °C).

The samples grown at T_S = 770 °C and T_S = 785 °C contain a dense ensemble of wires with fairly homogeneous sizes. Almost no wire growth could be observed for samples grown at T_S = 805 °C and higher, as it is also the case for undoped GaN NWs,[18,188] in contrast for instance to the growth of Si doped InN NWs for which a higher growth temperature, if compared to undoped NWs, was reported.[189] For both doping species (Si, Mg), changes in morphology have been observed by other authors[166] as well as within this thesis (see section 4.1 and 4.2).[118,150] Yet, the fluxes of the doping species used in the literature are much higher than the ones employed for fabrication of the samples discussed in this thesis. In fact the doping fluxes have been chosen as to promote almost untapered and well separated NWs. SEM images of two representative samples of each set can be seen in Fig. 4.22a) and b). In none of these samples a significant change in morphology can be detected.

Exemplary PL spectra of type-A and type-B samples are presented in Fig. 4.23a). The NBE peak of GaN was detected at around 3.47 eV in agreement with literature data.[28,48] The luminescence signal between 2.90 eV and 3.26 eV is ascribed to a DAP transition associated to Mg doping.[28,48,170] All type-B samples display a small and in some cases even negligible DAP signal intensity if compared to that of the NBE peak. In contrast, in type-A samples the DAP signal exceeds the NBE emission intensity by approximately one order of magnitude. The NBE transition of type-A samples (see Fig. 4.23b)) consists of two contributions, one centered at 3.467 eV associated with ABE and one located at 3.472 eV originating from DBE recombinations.[28,48] Both have approximately the same intensity and a similar FWHM of less than 3 meV. The NBE luminescence of type-B samples consists only of the DBE emission with a comparable FWHM of less than 3 meV. As GaN NWs usually display an n-type background doping, the DAP signal might be used as a measure of incorporated optically active Mg, leading at first sight to the conclusion that more Mg has been incorporated in type-A samples.[28,171,190] However, NW ensemble optical measurements can suffer from influences caused by geometric effects, for instance related to re-absorption of light by neighboring wires or a limited penetration depth of the laser light into the probed material.[164,177,191]

To confirm the existence of the measured effect, µ-PL measurements on single wires were carried out. Spectra were acquired of several single NWs. Two representative measurements are shown in Fig. 4.24. As observed for the ensemble case, the most obvious difference is the presence of a DAP transition in type-A samples. The difference in rel-

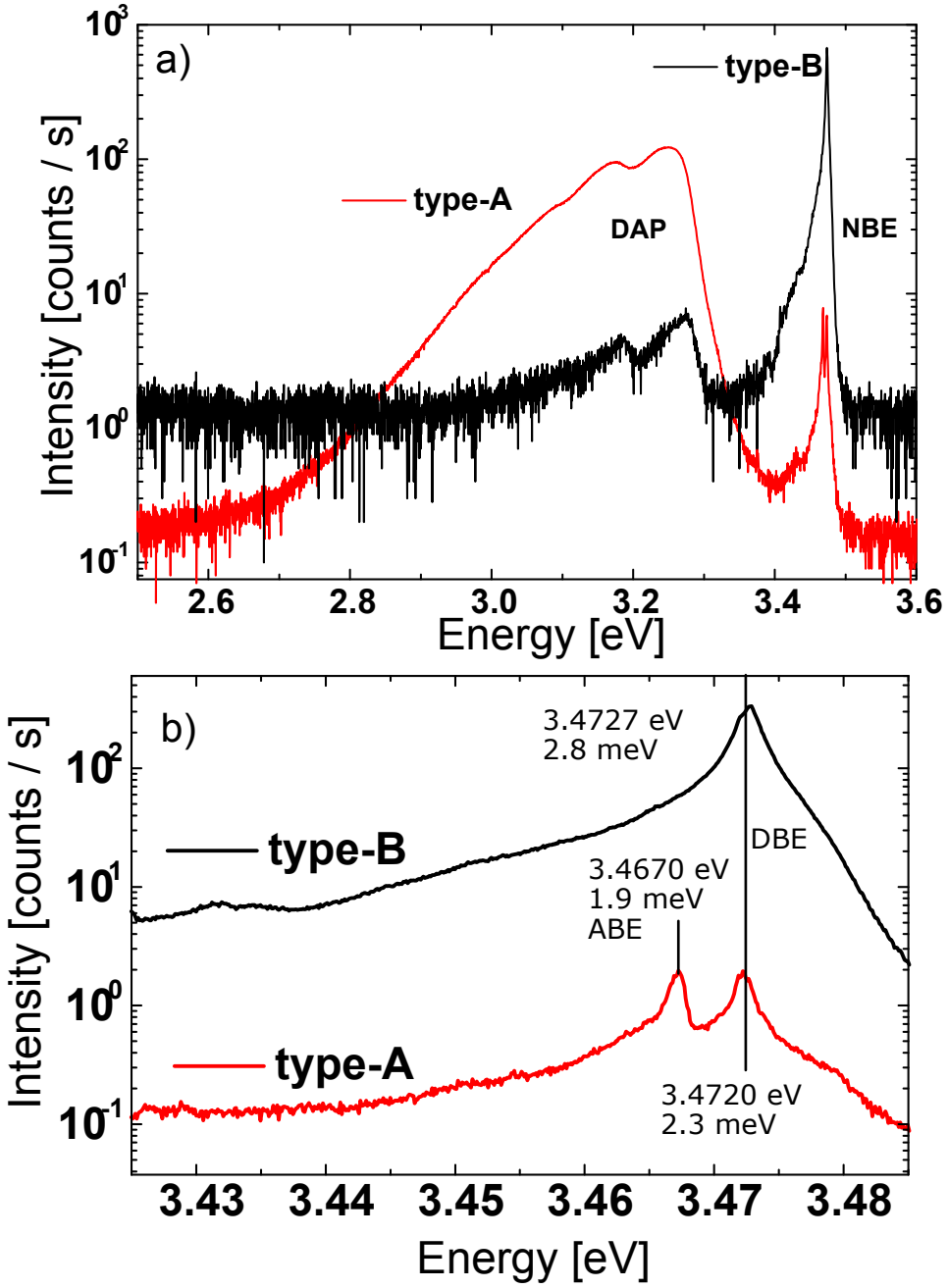

Figure 4.23: a) Ensemble PL data of the samples of type-A and B. b) PL signal of the NBE region at a higher spectral resolution. The vertical lines indicate the positions of DBE and ABE according to Reshchikov *et al.*[48]. The numbers next to the peaks are position and FWHM of the respective signal. The data was acquired by C. Pfüller, Paul-Drude Institut für Festkŕperelektronik, Berlin.

ative intensities of DAP and NBE, if compared to the ensemble measurements can be explained by the much higher excitation intensity required for the μ-PL measurements.

The μ-PL laser spot is larger than a single NW, therefore it does not allow to determine the spatial origin of the DAP luminescence. To this end, CL measurements were performed on cleaved samples in cross section with the electron beam parallel to the sub-

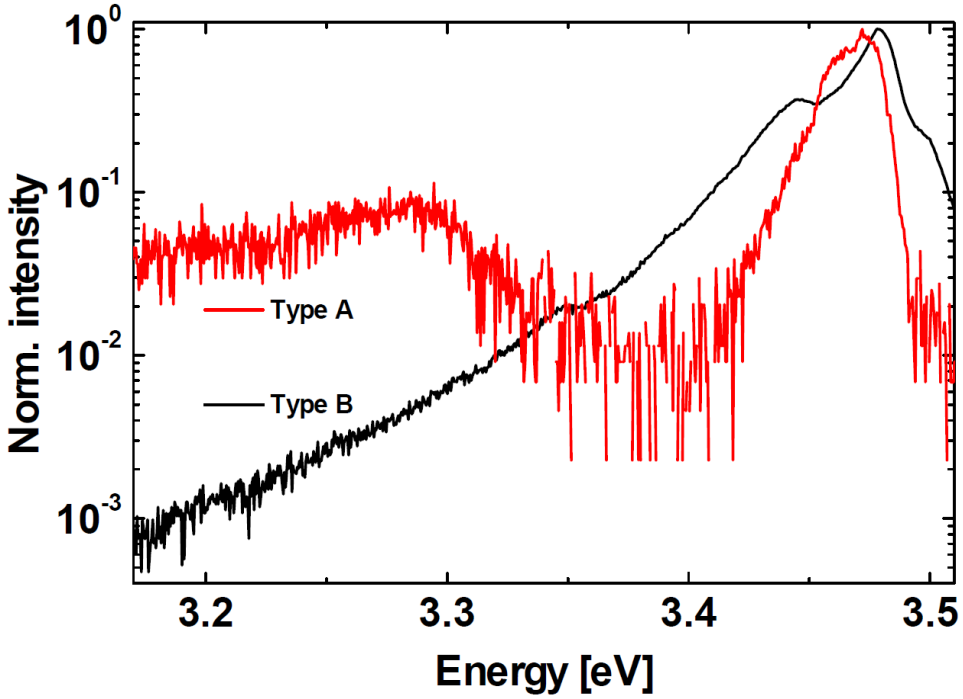

Figure 4.24: μ-PL spectra of single NWs dispersed on a SiO_2 substrate with different doping profiles. The data was acquired by C. Pfüller, Paul-Drude Institut für Festkörperelektronik, Berlin.

strate surface. The spectra acquired from the NW ensemble at low magnification resemble very well and thus further confirm the results of the ensemble PL measurements (see Fig. 4.25). The spacings of the three peaks in the spectral region between 3.1 eV and 3.3 eV of 92 meV each suggest, that these are phonon replica of the zero phonon line (ZPL) of the DAP transition at 3.26 eV.[28,48,166] The fact that the expected intensity decrease associated with phonon replica is not observed, suggests the presence of another broad emission in this spectral region (compare subsection 4.1.3).

In Fig. 4.26, SEM and two monochromatic images are presented for each sample type. The monochromatic images were recorded at 3.27±0.02 eV (DAP) and 3.46±0.02 eV (NBE). For type-A samples (Fig. 4.26a) - c)), the DAP clearly originates from the top half of the wires while the NBE emission is located predominantly in the bottom half. In the case of type-B samples (Fig. 4.26d) - e)), no spatial location of the DAP can be identified in contrast to the NBE emission which mainly originates from the top half of the NWs and is dominated by donor bound excitons.[50,192]

A flip of GaN polarity has been often reported for MBE grown layers at the onset of Mg co-deposition and it is well know that the polarity has a strong influence on the incorporation properties of Mg into the GaN matrix.[193,194] From this perspective, it is mandatory to explore the polarity issue.

Therefore, intensive TEM investigations of both samples were performed. The polarity of the wires was determined via electron energy loss spectroscopy (EELS), for details on this method see Kong *et al.*[195]. Several wires were investigated at multiple positions along the wire axis and in each case a nitrogen polarity was found. In addition, no other structural features that would distinguish the two types of samples could be found.

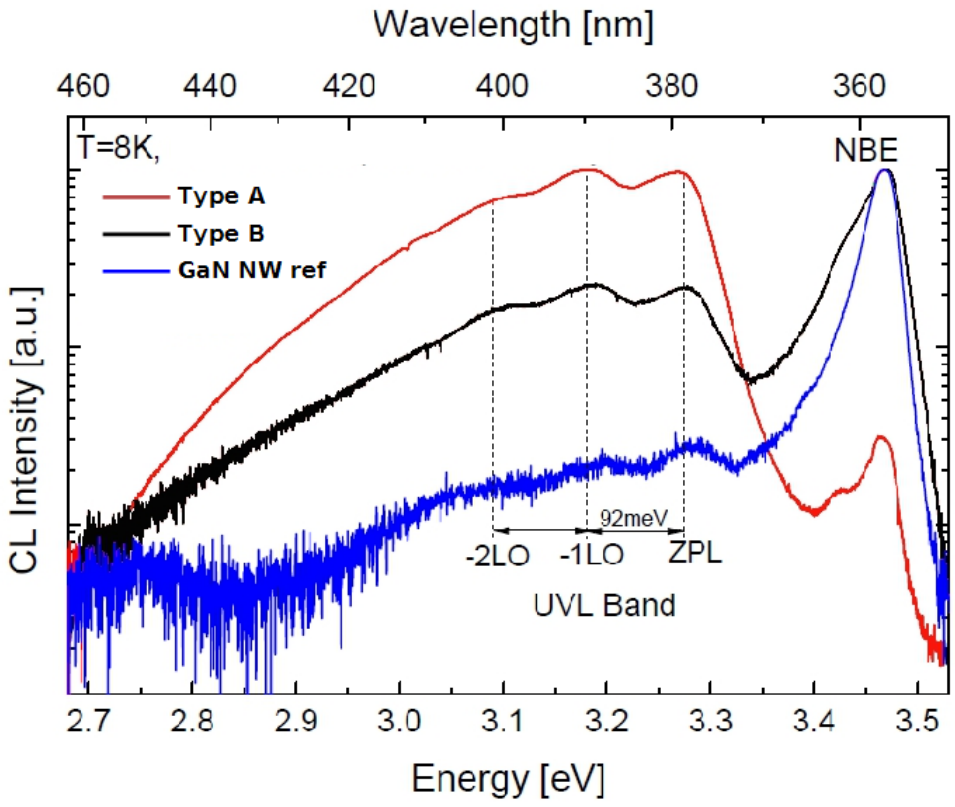

Figure 4.25: Ensemble CL spectra of GaN NWs with two different doping profiles and a GaN reference. The data was acquired by S. Geburt, Universität Jena.

The AlN buffer layer described above was intended to aid in the epitaxial orientation of the NWs and to prevent the formation of an amorphous Si_xN_y layer. TEM investigations show that instead small AlN islands are formed. The formation of the Si_xN_y was not prevented by the pre-deposition and nitridation of an Al film. Nevertheless, growth of AlN seems to aid in orienting the GaN NWs and fewer of them grow at an inclination angle other than $90° \pm 3°$.
Finding no closed AlN layer was a surprising feature. Instead most NWs are associated with one or two of these small AlN islands at their base (compare Fig. 4.27b)).
Considering PL, CL and TEM results, we conclude that during the first stages of the growth of GaN NWs, the incorporation of Mg is either hampered or it does not act as an acceptor, while in the latter phase of the growth, the Mg is more effectively incorporated and acts as an acceptor in the GaN matrix.
In general, it is reasonable to assume that the Mg incorporation takes place at the surface of the NW, either at the top or the sidewall. No further segregation into the NW is expected and thus a Mg atom, once incorporated, does not change its position. The Mg atoms are preferentially incorporated at the top of the NW, whereas incorporation at the sidewalls can safely be neglected since the wire diameter does not change significantly during growth under the used growth conditions (Fig. 4.22). Those Mg atoms impinging on the sidewalls can diffuse similar to Ga adatoms[139] either to the NW top or bottom. We assume that the Mg atoms reaching the bottom can be passivated, desorb or incorporate into the Si or Si_xN_y matrix. Such an incorporation or in-diffusion mechanism is hinted at in SIMS measurements of Mg doped NW. In Fig. 4.28 an increase in the $^{40}MgO^+$

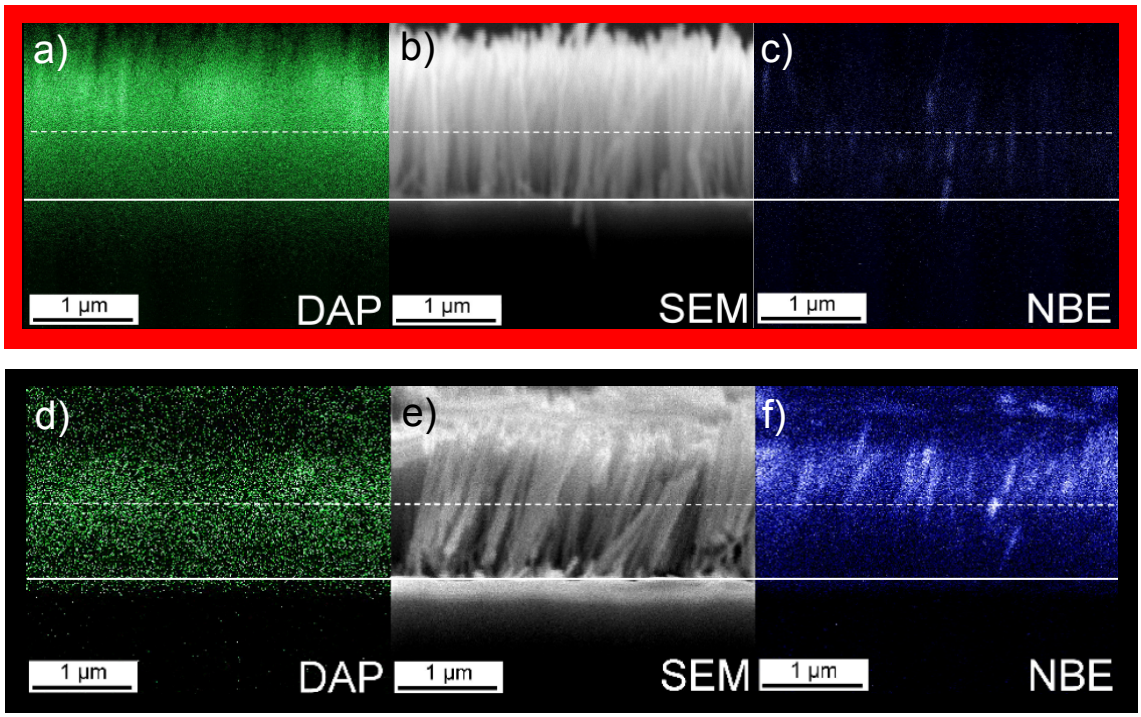

Figure 4.26: a) and d) monochromatic CL images of light emitted at 3.27(2) eV of samples of type-A and B respectively. Luminescence from this energy range originates from DAP transitions. b) and e) SEM micrograph of samples of type-A and B respectively. c) and f) monochromatic CL images of light emitted at 3.46(2) eV of samples of type-A and B respectively. Luminescence from this energy range originates from the NBE peak. The dashed line in each image indicates roughly half the height of the NWs. The data was acquired by S. Geburt, Universität Jena.

signal can be observed between 50 s and 100 s of sputtering time, well into the decrease of the $^{71}Ga^{+}$ signal and the simultaneous increase of the $^{30}Si^{+}$ signal. This suggests that Mg was integrated into the Si matrix during growth. These Mg atoms on the other hand would not have been available for the NWs anymore.

The final Mg concentration is thus given by the number of Mg atoms reaching the top facet of the NW (either by direct impingement or by sidewall diffusion). An upper limit can be given by assuming that all Mg atoms diffuse instantaneously to the top and get incorporated there. Since the total number of Mg atoms deposited on the sidewalls is linearly dependent on the NW length, the Mg concentration increases linearly if the NW length does not exceed the diffusion length (limited e.g. by desorption from side walls) of the Mg atoms. For longer NWs, the incorporation saturates resulting in a constant Mg concentration. The same behavior is expected when shadowing effects are considered to be relevant, for instance in case of high NW densities.

We further know, that the incubation time during the initial nucleation phase plays an important role in the determination of the growth rate as the total growth time should be reduced by the nucleation time (compare section 4.1.1).[118,123,126] This means that the effective Mg incorporation time of type-B NWs is shorter than that of type-A. However, the difference in nucleation time amounts only to a factor of 1.4 and thus it is not sufficient by itself to explain the measured data. Furthermore, we can speculate that incorporated Mg

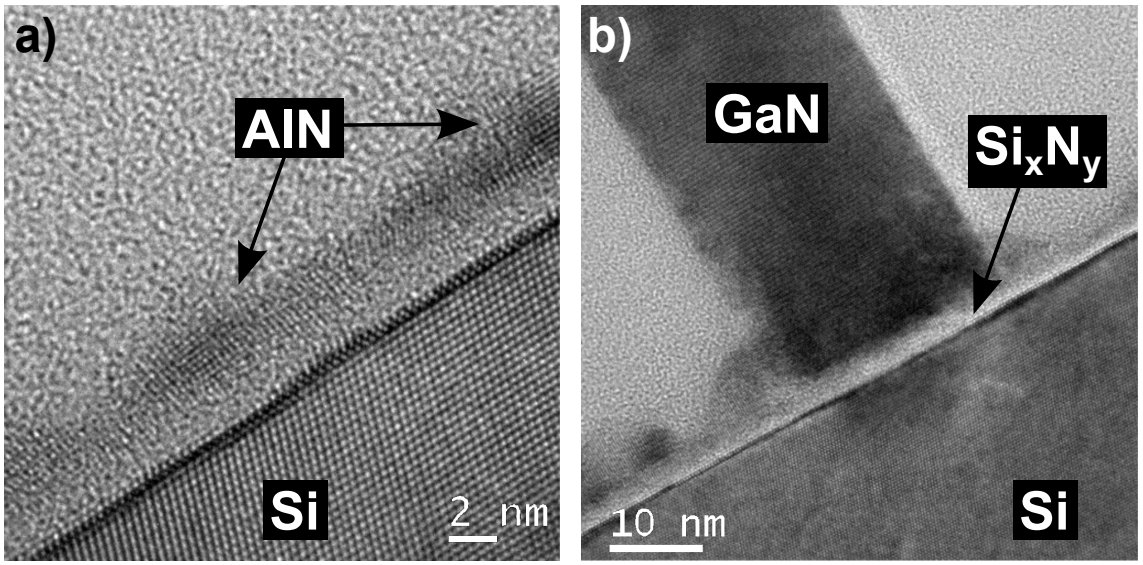

Figure 4.27: TEM images of a type-A GaN NW base. The images were acquired during the polarization determination via EELS.[195] The data was acquired by X. Kong, Paul-Drude Institut für Festkörperelektronik, Berlin

atoms might be passivated by in-diffusing Si atoms from the substrate. This can be further substantiated as usually undoped GaN NWs show at their base an almost optically inactive segment[50] and electrically active defects,[196] although those could not directly be related to Si in either donor or acceptor state.
Another effect that needs to be taken into account is the non-constant axial growth rate of GaN NWs.[113] The fact that NWs have a rather high growth rate at the beginning of their growth which stabilizes only after some time (the exact time depends on the growth conditions) causes an inhomogeneous material deposition. Therefore, Mg supplied at the beginning of the growth can be distributed over a bigger volume compared to Mg supplied in a later growth phase when the volume increase per time unit is smaller.
In summary, each effect considered singularly is insufficient to quantitatively explain the data. Yet, they all suggest the preferential incorporation of Mg as an acceptor at the later stages of the growth and we can speculate that the synergistic action of these effects is sufficient to support the experimental results.
In conclusion, we have investigated the effect of Mg doping in GaN NWs at different stages of the growth. Mg is much more likely to be incorporated when supplied after the NWs have already developed as assessed by PL and CL spectra. A polarity flip could be ruled out and nitrogen polarity was determined via EELS for all investigated samples. Mg incorporation hampering in the nucleation stage is discussed and could be explained considering the concomitant appearance of several kinetic and geometrical effects.
The results of this section lead to a technologically relevant conclusion. The incorporation of Mg in GaN NWs is much more effective if it is not done in the initial stages of the growth but rather when the NWs have developed for some time and gained a significant length. This effects the device design as it implies difficulties in the creation of p-type GaN at the Si/GaN interface. As a consequence GaN NW LEDs need to have their n-terminal at Si/GaN interface and their p-terminal at the top of the NWs.

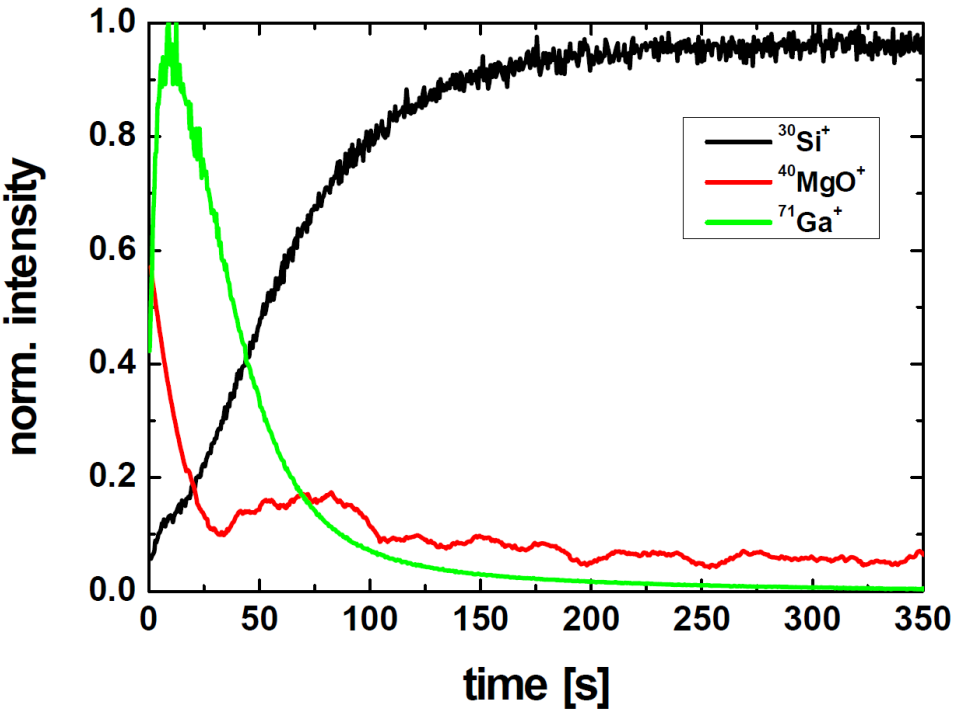

Figure 4.28: SIMS profile of a GaN NW ensemble doped with Mg.The data was acquired by ZCH, Forschungszentrum Jülich.

Conclusion

Within this chapter both p-type (Mg) and n-type (Si) doping species were investigated. Mg doping proves to have a significant influence on the growth behavior of GaN NWs. Their nucleation occurs faster in the presence of Mg[118] and also the lateral growth rate is increased. Even though the evidence for an increased incorporation at lower T_S is weak, it does not contradict this notion.[150]
Also Si has an influence on the growth dynamics of self-assisted GaN NWs. It leads to broadening of the NWs during growth and a loss in orientation with respect to the substrate. A Si flux was found at which the morphology and optical properties are only slightly effected while the conductivity is enhanced at the same time.
Nominal p-i-n and n-i-p junctions within GaN NWs were synthesized. The strong difference in the optoelectronic properties upon reversing the doping profile was investigated. Especially the acceptor concentration varies significantly. Though no single mechanism discussed is sufficient to explain the observed behavior, they all point to an improved incorporation of acceptors when Mg is supplied after the initial formation of the NWs. The technologically relevant information extracted from this result is that the doping sequence for a NW pn-junction needs to start with Si doping and end with Mg doping.

5. InGaN structures

The active zone of a GaN based LED typically consists of an insertion of $In_xGa_{1-x}N$. This alloy enables capturing of the electrons and holes for efficient recombination[13,28] as well as tunability of the emitted photons through tailoring of the bandgap between 0.7 eV of InN and 3.4 eV of GaN (see section 2.2).[13,26]
The goal of this chapter is to synthesize InGaN QWs within GaN NWs and to achieve control of the In composition within them. The discussion is focused on the effects which occur if InGaN is grown subsequent to GaN NW growth. In order to get a feeling for the behavior of this kind of growth, initially pure InGaN growth is addressed (section 5.1). Moreover, the growth of segments and nanodots on top of a GaN NW base and the resulting structures are presented (section 5.2).[176] Finally the QW and MQW growth is briefly discussed in section 5.3.[197–199]

5.1. InGaN nanowires on Si

In order to create InGaN for NW-LEDs initial tests were conducted to grow pure InGaN NWs directly on Si. For this purpose the silicon substrates were cleaned before epitaxy by a standard ex-situ chemical cleaning procedure (2 min ultra sonic bath in Acetone and Isopropyl alcohol each) and by in situ annealing in ultra-high vacuum at 925 °C for 15 min, in order to obtain an oxygen-free surface. The substrate was cooled down to a substrate temperature around T_S = 600 °C. This is well above the decomposition temperature of InN (470 °C).[28,146] For the growth, a Ga flux of 0.3 nm/min, an In flux of 1.1 nm/min, an RF-power of 500 W, a nitrogen flow rate of 4 sccm and a growth duration of 2 h was chosen. Several authors have found that the In content in InGaN is strongly effected by the growth temperature and less so by the ratio of the supplied material.[147,200–202] For this reason a series of samples with different growth temperatures, namely T_S = 580 °C, 610 °C and 630 °C, was grown. In Fig. 5.1 SEM top view and birds-eye images of these samples are presented. All three show a columnar morphology and exhibit a strong tendency of coalescence. The spacing between the structures is very small compared to typical GaN NW growth (see e.g. Fig. 3.5). In addition to NWs a parasitic layer is formed in the case of the T_S = 580 °C growth.
PL measurements were conducted in order to determine whether the formed nanostructures consist of InGaN. According to equation (2.2) the bandgap of InGaN should shift with rising In content towards the bandgap of InN (0.7 eV). Fig. 5.2 shows the acquired spectra for two of the samples described above, along with two standard spectra, one of InN NWs and one of GaN NWs.
The shift in emission energy to around 2.2 eV suggests the synthesis of InGaN with an In content of around 31% for the sample grown at T_S=630 °C and 34% for the sample grown at T_S=580 °C. The acquired spectra are rather broad, indicating significant compositional variations. Even though a Ga to In ratio of $\approx$ 1:4 was supplied, much less In has been incorporated, than the 80% In-content expected for total incorporation of all the supplied material. This can be explained by the fact that T_S was well above the decomposition

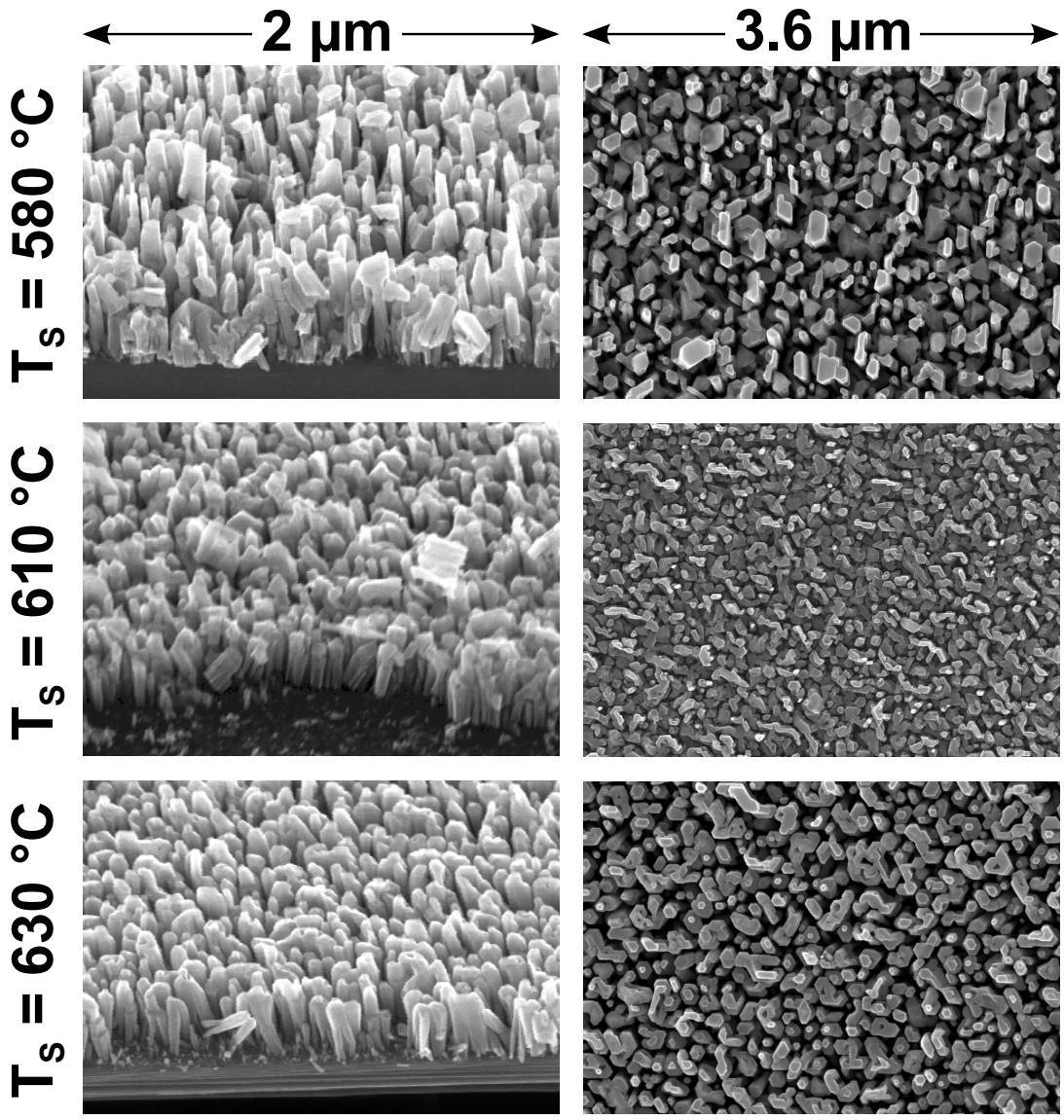

Figure 5.1: SEM top view and birds-eye images of InGaN NWs grown directly on Si(111) substrates with varying T_S.

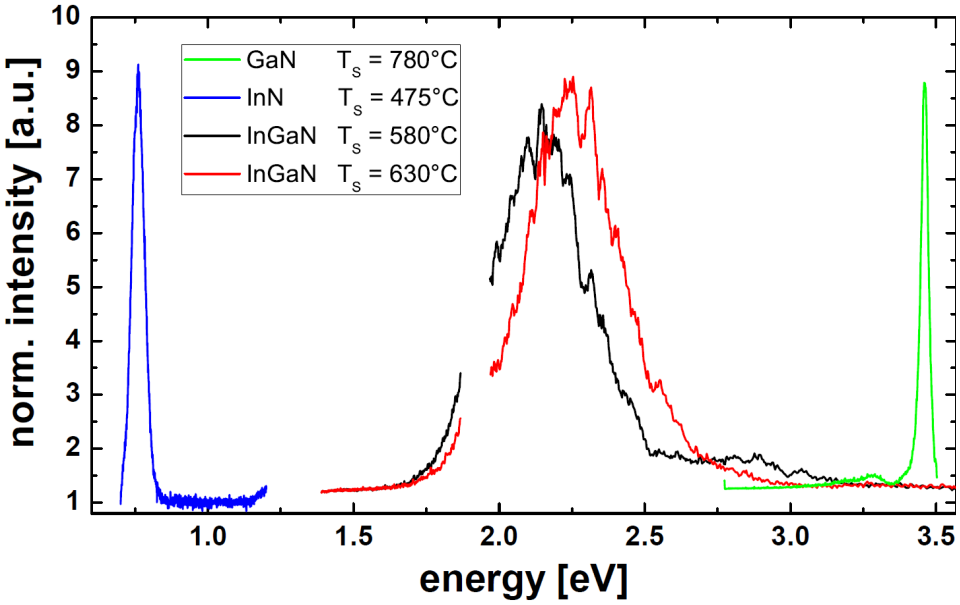

Figure 5.2: PL spectra of InN, InGaN and GaN NWs grown directly on Si(111) substrates. The InN NW data was acquired by T. Gotschke, Forschungszentrum Jülich.

temperature of InN. This means that In-N bonds are not stable and a dynamic equilibrium between the formation and breakage of bonds is established.
Due to the low growth temperature, compared with typical GaN growth, a high density of structural defects can be expected, which could cause defect luminescence in GaN with a PL emission at 2.2 eV.[48] In order to rule this hypothesis out, a GaN sample grown with the same growth parameters but without In supply was investigated, and no luminescence at 2.2 eV could be detected.
In addition to the discussed sample series in which T_S was varied, series with a change in In or Ga flux were grown as well. In neither one of them a significant shift of the luminescence due to the change in growth parameters was found via PL. This confirms the findings of other authors, mentioned earlier, that T_S is the most influential parameter for the In incorporation in GaN.[147,200–202]
InGaN is desired to be the active region of a GaN NW based LED, for this reason these initial trials directly on Si can only provide some first insights into the behavior of InGaN MBE growth in N-rich conditions. The next step is the synthesis of InGaN on top of an existing GaN NW.

5.2. InGaN segments on GaN nanowires

This section will focus on the overgrowth of a GaN NW base with an InGaN cap. A majority of this section will focus on an overgrowth of equal duration as the base growth, 2 hours each. In addition to this, data from GaN NWs overgrown for only 30 minutes will be presented.

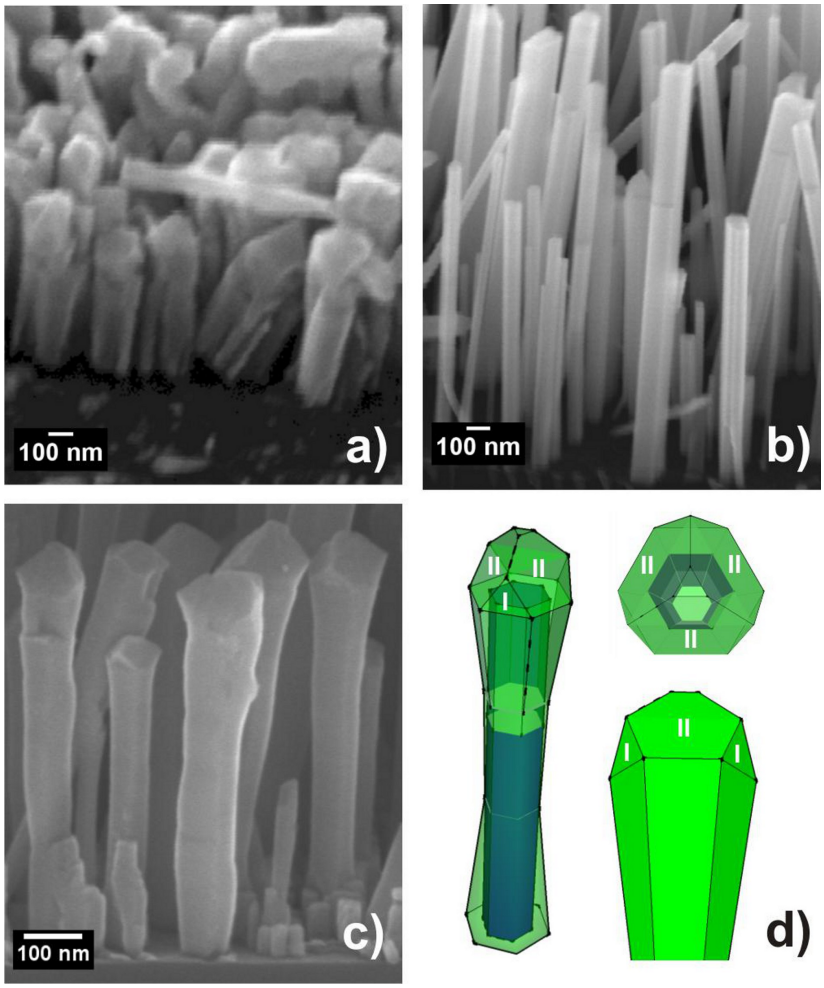

Figure 5.3: SEM birds-eye images a) of InGaN grown directly on Si at T_S = 600 °C. b) of pure GaN NWs grown at T_S = 785 °C. c) SEM cross section image of a InGaN/GaN heterostructure, both InGaN and GaN were grown for 2 hours each with the same growth conditions as the samples displayed in a) and b), respectively. d) Sketch of the NW morphology according to analysis. The blue core represents the initially grown GaN NW. The green shell is formed during the subsequent InGaN growth.

Growth and structural properties of InGaN segments on GaN NW

The InGaN/GaN heterostructure NWs were grown on Si(111) substrates. The silicon substrates were cleaned before epitaxy in the same way as described in section 5.1. The GaN NW base was grown at a substrate temperature of T_S = 785 °C, a Ga flux of 0.7 nm/min, an RF-power of 500 W, a nitrogen flow rate of 4 sccm and a growth duration of 2h. Subsequently the growth was interrupted and T_S ramped down to 600 °C within 10 minutes. Thereafter the InGaN growth was started for 2 h, or 0.5 h respectively with a Ga flux of 0.3 nm/min and an In flux of 1.1 nm/min with the same nitrogen plasma conditions.

The morphology of the samples was investigated by SEM. SEM birds-eye images in Fig. 5.3a) and Fig. 5.3b) show pure InGaN and GaN NWs, respectively. These two reference samples were grown under the same growth conditions used for the GaN NW base and InGaN cap (2 h) respectively. The InGaN and GaN NWs are displayed to allow comparison with the InGaN/GaN heterostructures, shown in Fig. 5.3c). It can be

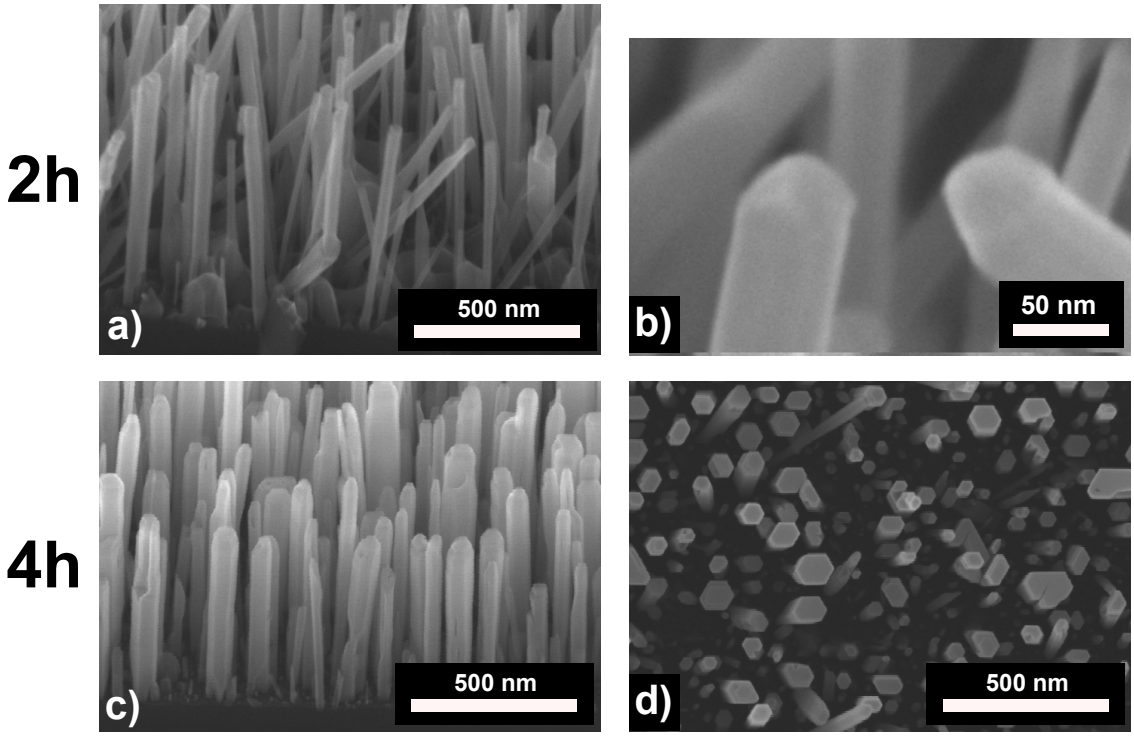

Figure 5.4: SEM images of InGaN segments with 30 minutes growth time on top of a GaN NW base. a) and b) SEM birds-eye images of segments grown on a GaN NW base of 2 h growth time. c) and d) SEM birds-eye and top view images of segments grown on a GaN NW base of 4 h growth time.

seen (Fig. 5.3a)) that the InGaN nanowires have a small aspect ratio of about 4 and no symmetric hexagonal shape is evident from SEM top view images. In contrast to the InGaN NWs, both GaN NWs and the heterostructure NWs have high aspect ratios and exhibit faceting with hexagonal shape, consistent with the top basal plane perpendicular to and growth along the c-axis. However, it can be seen that the heterostructure NWs increase in diameter towards the top, whereas the GaN NWs have smooth and very parallel sidewalls, i.e. a uniform diameter over the entire length of the GaN NW. Moreover the GaN NWs have a flat top surface while the InGaN/GaN NWs exhibit a complex apex with a three-fold symmetry. Three of the 6 sidewalls are terminated in triangular shaped sidewalls labeled I in the morphology scheme in Fig. 5.3d) (the blue hexagonal core represents the initially grown GaN while the green shell is formed during the subsequent InGaN growth). The hexagonally shaped facets labeled II are inclined towards the center of the wire and form a tripod pyramid. The complex morphology is similar to the one observed by Kishino *et al.*[158] but differs from the findings by Hong *et al.*[203] where the NW tops were seen to be almost flat.

For the use in NW LED structures the InGaN active zone will consist of much smaller segments then those presented in Fig. 5.3c). For this reason InGaN segments with only 30 minutes growth time were synthesised (see Fig. 5.4). Also for this sample pyramidal shaped top facets can be seen, especially in the case of the segments on top of the 2 h growth time GaN NW base (Fig. 5.4b)). The wires with the 4 h base growth time on the other hand show tapering but have flat top facets, see Fig. 5.4c) and d). This difference can be explained by the significant difference in the diameters of the wires: The ones

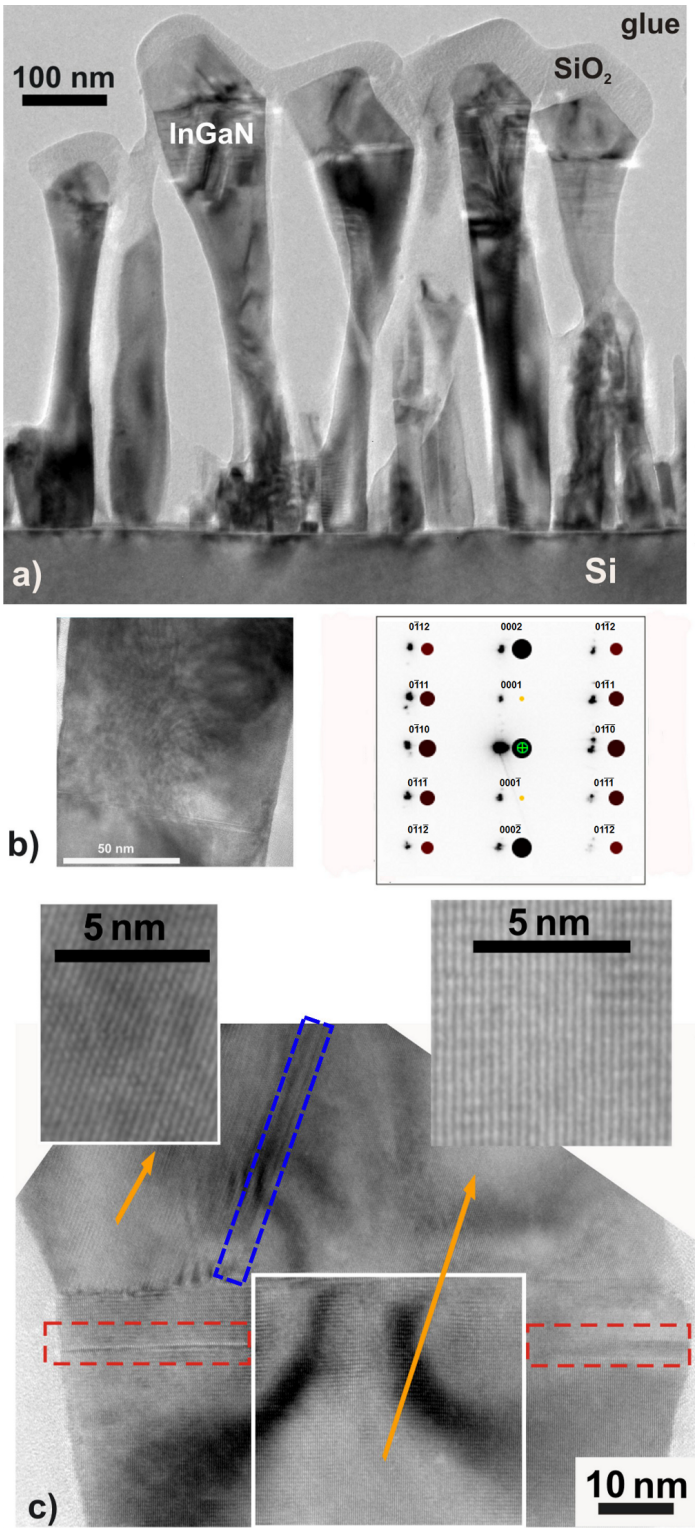

Figure 5.5: a) TEM cross section of the InGaN/GaN NW ensemble. b) TEM of the top region of an InGaN/GaN heterostructure nanowire and the corresponding diffraction pattern. c) HRTEM of the top region of an InGaN/GaN wire. The white box indicates the previously grown GaN, stacking faults can be observed in the areas in the red and blue boxes. The insets show HRTEM pictures of two different regions in the NW. The data was acquired by E. Sutter, Brookhaven National Laboratory.

with a 4 h growth time base have a significantly bigger average diameter. This means the same amount of InGaN capping has to fit into a much smaller area in the case of the 2 h base growth compared with the 4 h base growth. In turn this leads to a decreased height of the caps and might not be enough for the formation of a pyramidal shape cap. Such a behavior could also be the explanation for the different observations by other authors mentioned before[158,203] and is currently a topic of ongoing research.[204] For both NW base types no overgrowth of the side facets is obvious as there is no increase in diameter towards the top. This is different from the case of the sample displayed in Fig. 5.3c) with 2 h InGaN growth time.
HRTEM investigations were performed, in order to investigate further the overall morphology and the complex apex structure found in the samples displayed in Fig. 5.3c) with a 2 h InGaN growth time. Fig. 5.5a) shows a cross-sectional TEM image of an array of InGaN/GaN NWs. In contrast to the pure GaN NWs, the InGaN/GaN NWs exhibit a gradual increase in diameter towards the tops (as well seen by SEM, Fig. 5.3c)). A cap-like structure with a faceted apex is visible at the top part of the NWs. A somewhat smaller increase in diameter is seen close to the base of the heterostructure NWs as well as some additional small wires adjacent to the base of the longer ones. The change in diameter of the longer NWs can be attributed to InGaN growth on the GaN NW sidewalls. The small NWs most likely also nucleated in the InGaN phase of the growth[126] as they show the same tendency to coalesce (observed in SEM images not shown) as is observed for pure InGaN NWs (SEM image in Fig. 5.3a)). In Fig. 5.5b) a higher maginification TEM image from the middle section of a heterostructure NW and the corresponding diffraction pattern (DP) are shown. The DP can be indexed to the GaN wurtzite structure growing along the c-axis. The simulated DP along the $[2\bar{1}\bar{1}0]$ zone axis is shown for comparison in color (slightly shifted towards the right from the experimental spots). It can be seen that the diffraction spots originating from this part of the NW are of two different crystal orientations, i.e. the electron beam probes regions of material with two different lattice spacings. This would be the case if the electron beam penetrates through a thin but well defined shell of InGaN (larger lattice constant than GaN) grown on the GaN core. Another cause could be the presence of a cubic phase alongside the hexagonal wurtzite phase.
The cross-sectional HRTEM image in Fig. 5.5c) shows a high resolution image of the cap on top of the GaN NW base. The faceted apex of the wire has a different crystallographic orientation than the lower parts. This is highlighted in the insets of Fig. 5.5c) showing lattice images of the trunk and cap of the NW. The DP from the cap shows that there is still a GaN core present in the cap region but the InGaN alloy has now a growth direction inclined by 66° relative to the original direction. The inclination of the InGaN cap fluctuates from wire to wire, with inclinations of the terminating facets leading to shape variation. The interface between the two distinct parts of the NW having different crystallographic orientation is clearly indicated by the termination of an inclined stacking fault (marked by a blue rectangle in Fig. 5.5c)). In addition, the cross section depicts two defects one on either side of the image, which extend approximately 25 nm from the side surface into the wire (marked by the red boxes in Fig. 5.5c)). The position at which these defects terminate appears to coincide with the sidewall surface of the previously grown GaN NW. This leads to the conclusion that the subsequently grown InGaN alloy covers the top part of the GaN NW on the sidewalls and the top facet, where it forms a complex cap, schematically shown in Fig. 5.3d). For illustration the white line in Fig. 5.5c) indicates the interface between the GaN trunk and the InGaN cap. Thus there is an axial interface at the top and a radial interface at the sides of the GaN trunk. The InGaN grows

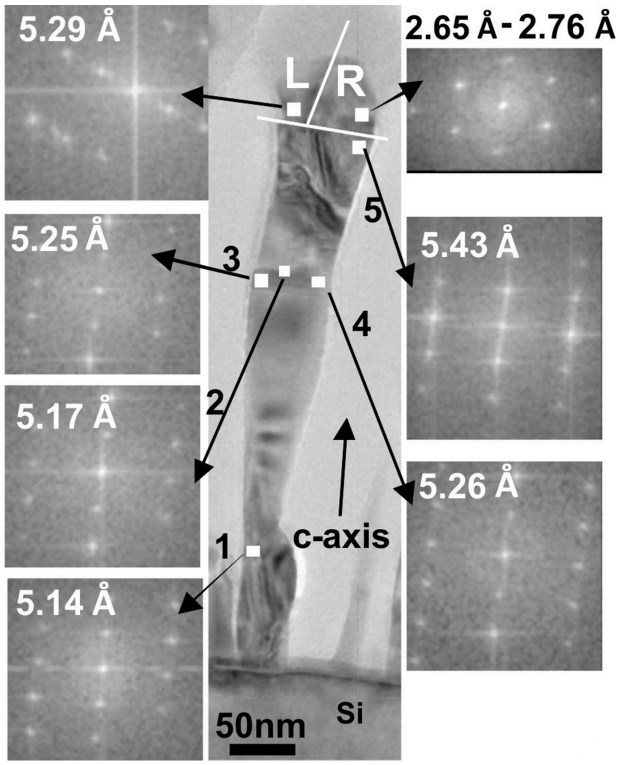

Figure 5.6: Local FFT results from indicated positions of the TEM image along the wire and the corresponding c-lattice parameters. The azimuth is the [11$\bar{2}$0] direction. The data was acquired by E. Sutter, Brookhaven National Laboratory.

on the sidewalls at the upper part of the GaN trunk, forming a core-shell region. On the top facet of the GaN NW core a faceted cap is formed.

A careful structural investigation of the NW in Fig. 5.6 was performed, in which HR-TEM images from $10 \times 10\,\mathrm{nm}^2$ regions along different parts of the wire were analyzed using fast Fourier transform (FFT) to evaluate the spacings of the crystallographic planes of the InGaN and the GaN core and their relative orientation. The areas of FFT analysis were taken from regions with no visible stacking faults or other extended defects. The presence of such defects and strain fluctuations in neighboring areas can influence local lattice spacings. Yet, such defects are only found in the parts of the NW close to the top. These effects, as well as the local residual strain are neglected in our computation of the In concentration profile. The InGaN growing on the sidewalls, forming the shell around the trunk has the same crystal orientation as the GaN. Within this core-shell region of the wire, InGaN is deposited non-uniformly, resulting in NWs with constantly increasing diameter toward the top. In the lower part of the NW the smallest diameter of about 25 nm is found, which corresponds approximately to the GaN NW core diameter. The plane spacings fluctuate in a wide range along the wire. As can be seen in Fig. 5.6, there are regions with lattice distances close to 5.18 Å the value of pure GaN (position 1 and 2 of the GaN core), as well as regions with larger plane spacing up to 5.43 Å. However, the most frequent value determined in the shell region is about 5.26 Å as for the points 3 and 4 in Fig. 5.6, which corresponds to 16% In content in an unstrained alloy. If some compressive strain remains, the In concentration is underestimated by this procedure. The strain of a thin InGaN layer with 20% In concentration deposited on the lateral sides

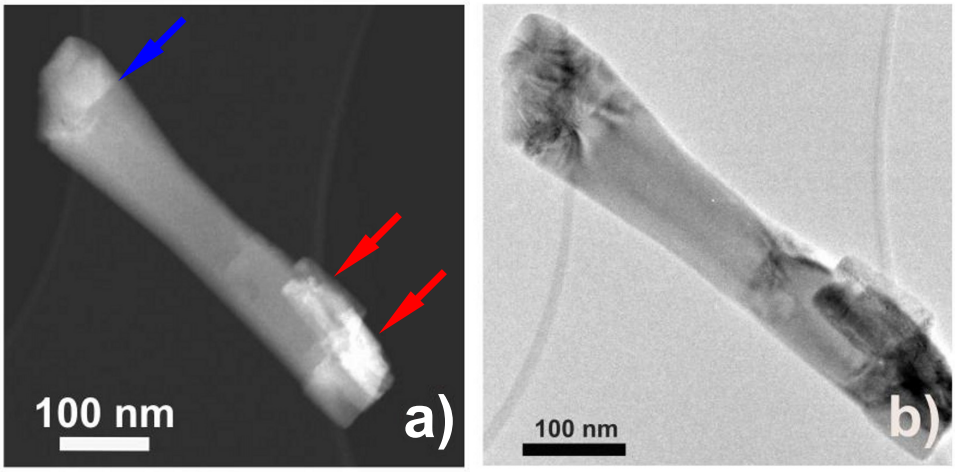

Figure 5.7: TEM image of a single wire on a copper grid. a) Z-contrast image of the same wire shown in b) in bright field imaging mode. The arrows in a) indicate the position of the cap interface (blue arrow) and of some small wires attachted to the one under investigation (red arrows). The data was acquired by E. Sutter, Brookhaven National Laboratory.

of the GaN NW can be estimated at about 2%. The local In concentration has a tendency to increase and strongly fluctuate towards the top of the core-shell NW region, reaching values as high as 50% In at point 5.

In the InGaN cap which grows on the top of the GaN wire, domains with different crystallographic orientations can be identified. In the particular TEM image of Fig. 5.6, two domains are visible. These are separated by white straight lines in Fig. 5.6. One domain (L - left part) has the c-axis in the same plane ($[11\bar{2}0]$), as the rest of the wire, but rotated approximately 70° relative to the GaN NW growth direction and the estimated lattice distance of 5.26 Å which corresponds to an alloy containing 22% In. The other region (R - right part) of the cap might be a wurtzite structure with the c-axis almost perpendicular to the c-axis of the rest of the wire, or may be of cubic type. As previously discussed, the formation of different crystallographic domains determines the faceted shape of the InGaN cap, which frequently exibitins a 3-fold symetry.

Fig. 5.7a) and Fig. 5.7b) show the annular dark field image and bright field TEM image of a single heterostructure NW, respectively. In annular dark field imaging, heavier nuclei such as In compared with that of Ga, appear brighter. Therefore bright areas are an indication where In atoms are incorporated. For this reason this method is also call Z-contrast. The interface between the trunk and the cap (upper left corner in Fig. 5.7a) indicated by the blue arrow) is clearly visible due to Z-contrast indicating higher In content in the cap compared to the remaining NW (see below for details). At the base of the NW (lower right corner in Fig. 5.7a) indicated by the red arrows) brighter contrast is visible, which originates from three small wires attached to the longer one. This brighter contrast results from two factors: I. Due to this agglomeration the e-beam penetrates through more material, which gives rise to a higher number of scattered electrons at the annular detector angle and II. The shorter NWs at the base nucleated later than the fully grown NWs, during the InGaN growth as discussed above. Most probably they contain more In than the amount at the base of the fully grown NW which was not exposed to In during its initial synthesis. Importantly, in Fig. 5.7a), a brightness contrast change is

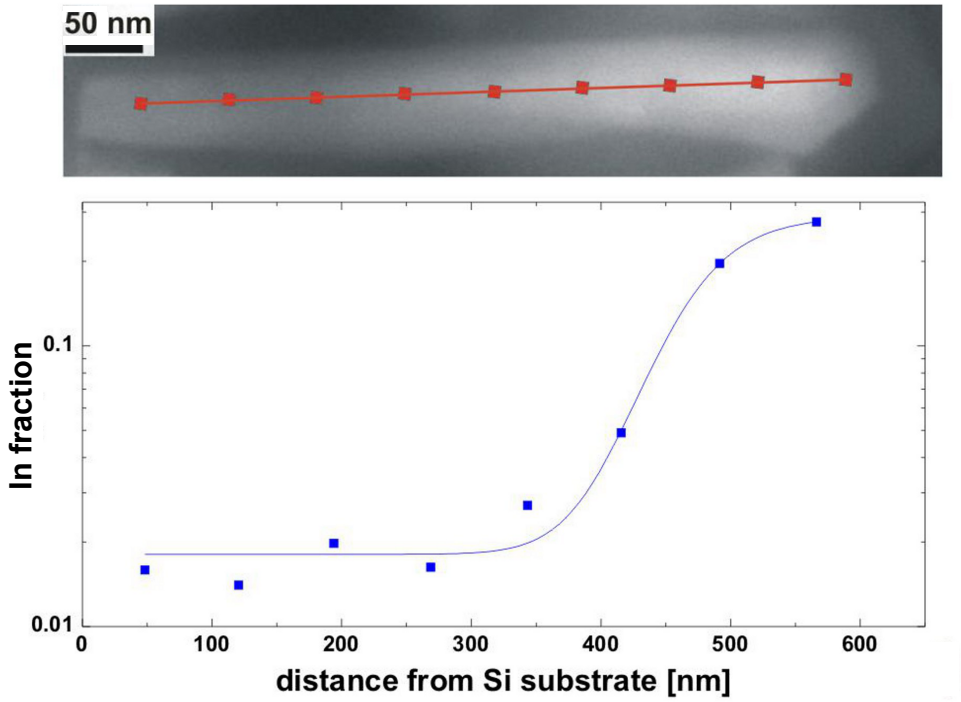

Figure 5.8: STEM image of InGaN/GaN heterostructure indicating where local EDS spectra have been taken (red boxes). The graph gives the fraction of In with respect to Ga in the beam path as a function of the distance from the Si substrate. The EDS spectrum at the top of the wire was left out as the signal to noise ration was to small. The data was acquired by E. Sutter, Brookhaven National Laboratory.

observed along the growth axis of the NW, which indicates that the interface between the initially grown GaN NW and the subsequent InGaN growth is rather sharp.
In order to evaluate the In concentration, EDS measurements were carried out in scanning transmission electron microscope (STEM) mode with a spot size of about 0.2 nm. Fig. 5.8 shows a representative bright-field (BF) STEM image of an InGaN/GaN NW heterostructure along which EDS line profiles were taken. The points at which the EDS measurements were performed are marked by colored dots. The In content as a function of the distance from the Si substrate is shown in Fig. 5.8. The In concentration is evaluated as a mean value which includes the contribution due to the GaN core. Overall In was detected over the entire length of the NW even though the distribution is not uniform. While the middle section of the wire contains very little In, the mean concentration of In in the cap increases rapidly and reaches about 27 atomic %.
X-ray diffraction measurements in a ω-2ϑ geometry of the same sample are presented in Fig. 5.9. The vertical lines mark the expected position of the pure materials. The formation of InGaN causes a change in the lattice parameters (see equation (2.1)). This in turn results in a shift of the signal towards smaller Bragg angles compared with GaN. The broad peak detected at 17° indicates compositional variations in line with the finding of the TEM analysis discussed previously.

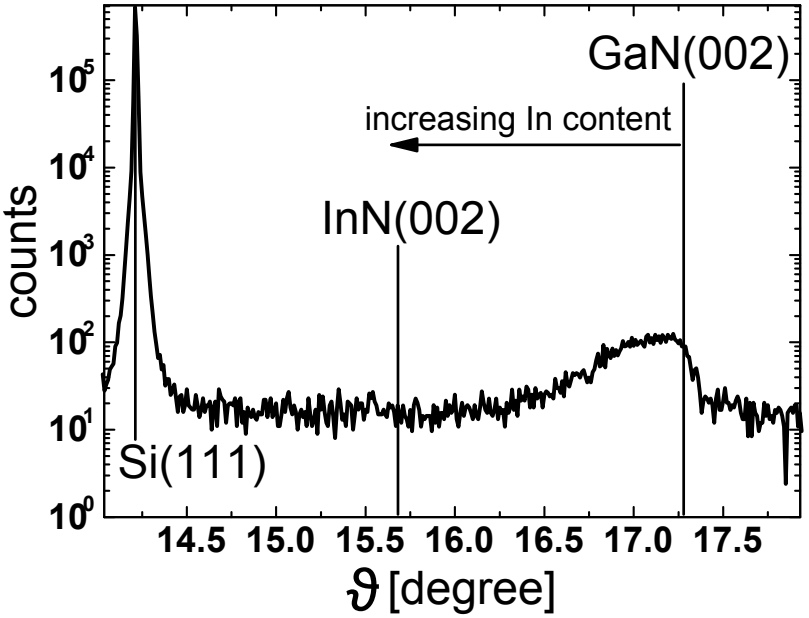

Figure 5.9: X-ray diffraction data of an InGaN segment on top of a GaN NW base. The vertical lines indicate the positions where pure GaN and InN peaks would be found, these values are taken from Morkoç.[28] The data was acquired by T. Gotschke, Forschungszentrum Jülich.

Optical properties of InGaN segments on GaN NW

The PL spectra of the three samples shown in Fig. 5.3 are presented in Fig. 5.10. The InGaN NWs show a very broad PL emission (FWHM = 0.76 eV) centered at 2.1 eV. However, no emission was observed in the near band edge region of GaN around 3.47 eV. This broad peak could be assigned to InGaN alloy band edge emission, but also to defects present in GaN. If spontaneous phase seperation takes place, GaN NWs or GaN inclusions in InGaN could have also been produced. The PL spectrum of the GaN NWs shown in Fig. 5.3b) has a strong band edge emission that contains FE and DBE contributions.[16] In addition emission between 3.1 eV and 3.26 eV is observed, which is typically assigned to a donor acceptor pair DAP transition.[28] The PL spectrum of the InGaN/GaN NW heterostructure shown in Fig. 5.10 has the characteristics of both GaN and InGaN NW spectra described previously. In the spectral range of the emission from the GaN core, the GaN NBE peak as well as the DAP region can be observed. The broad emission from the InGaN is centered at about 2.2 eV with a FWHM of 0.8 eV. The peak position suggests an average incorporation of approximately 30% In,[28] in agreement with EDS measurements. The broadness of the emission could be explained by compositional variations of the InGaN alloy along the NW and between NWs.[205] This is confirmed by μ-PL measurements on single InGaN/GaN NW heterostructures presented in Fig. 5.11. For this type of measurement the wires were mechanically removed from the growth substrate and deposited on a thermally oxidized Si(100) substrate with gold markers. The markers allow the identification of individual wires even after transfer of the sample to another setup or, as in this case, to another city. In total 21 wires have been investigated, all showing luminescence near the GaN band edge region. Most NWs also exhibit luminescence below 2.6 eV. The center of this emission varies from wire to wire and has a FWHM as

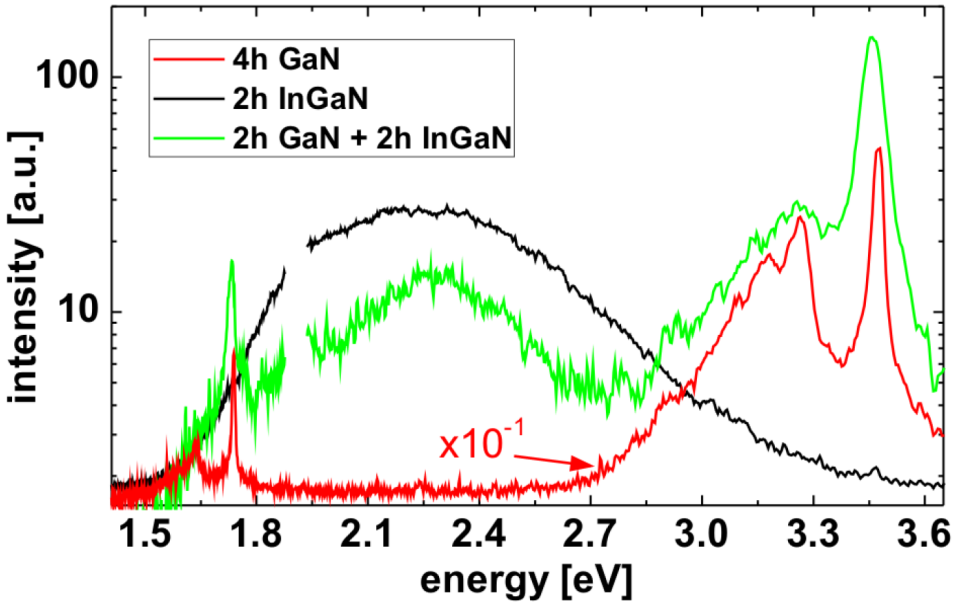

Figure 5.10: PL spectra for the samples shown in Fig. 5.3a) - c) at 160K, deleted points are due to second harmonic of the excitation laser.

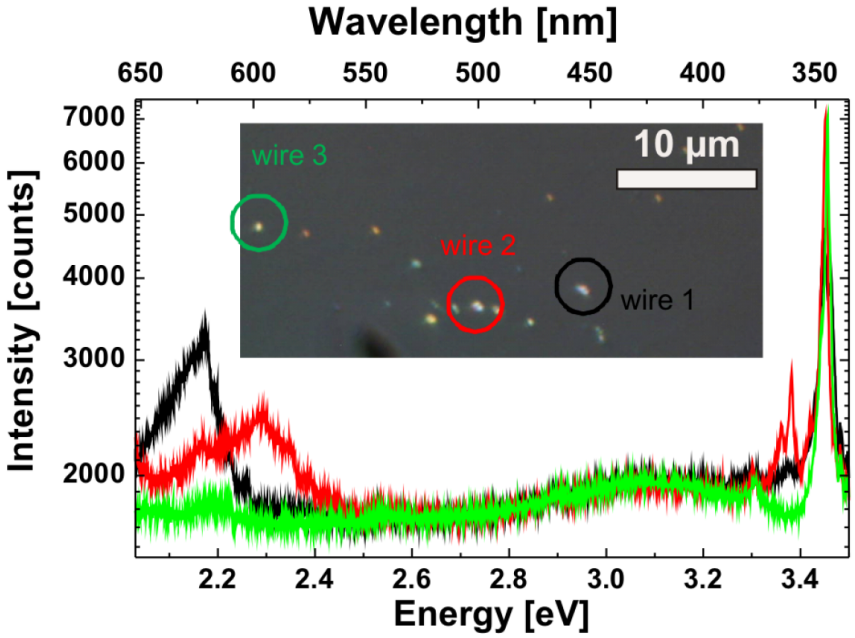

Figure 5.11: µ-PL measurements of single NWs with a cap of 2 h growth time. The positions of the individual wires is indicated in the inset (optical microscope). The PL data was acquired by S. Kremling, Universität Würzburg.

low as 0.25 eV. This broadening is assigned to band gap variations due the different In content in the core-shell and cap segments of individual wires. A variation of the In content of 8% corresponds to the FWHM of 0.25 eV. This variation of the In content indicated by µ-PL is in agreement with that of the TEM analysis discussed previously.
The excitation power series displayed in Fig. 5.12 shows µ-PL of a NW with an InGaN

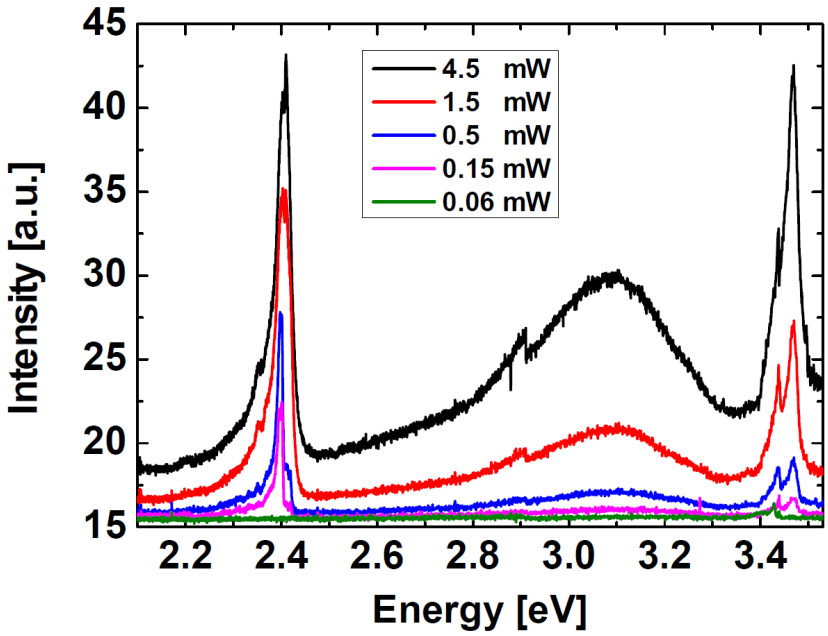

Figure 5.12: Power dependent μ-PL measurements of single NWs with a cap of 30 minutes growth time. The data was acquired by S. Kremling, Universität Würzburg.

segment of 30 minutes growth time, the FWHM of the InGaN luminescence is much smaller than for the wires with segments of 2 h growth time. This supports the statement made above that the broad peak displayed in Fig. 5.11 is in part caused by compositional variations caused by the additional shell growth (discussed in section 5.2). There is little shift with excitation power indicating an absence of internal fields. The presence and strength of internal fields in InGaN QWs in NW is a matter on ongoing research.[40] In addition it is noteworthy that the InGaN luminescence intensity is on the same order as the NBE emission of GaN even though much less InGaN material was deposited.

In order to additionally confirm the In concentration derived from PL measurements and to rule out green defect luminescence of the GaN[28,196,206] Raman measurements were conducted exciting the sample using the 488 nm line of an Ar^+ laser. As a reference, spectra from GaN and InGaN NW samples were also obtained and compared with the InGaN/GaN NW heterostructure sample. The Raman spectra of the NW samples are displayed in Fig. 5.13. For comparison, the Raman spectrum of an MOCVD grown InGaN thin film with 24% of In is also shown. After subtraction of the luminescence background, a clear Raman peak emerges in the spectra of both, the InGaN/GaN and the InGaN NW samples at about 700 cm^{-1}. This corresponds to LO modes of the InGaN alloy, which are resonantly enhanced via the Fröhlich interaction under the near resonant conditions of the experiment.[207] No feature associated with the E_2 mode could be observed above the luminescence background. Given the morphology of the NWs (see Fig. 5.3), which exhibit a large proportion of lateral and beveled facets, the observed LO peak is probably due to quasi-LO modes with a strong component of the E_1(LO) mode (see for instance Harima[168]). However, the A_1(LO) and E_1(LO) modes are very close in frequency,[208] and therefore a single LO peak is observed due to broadening of the Raman lines by alloying fluctuations. The frequency of the resulting quasi LO mode gives a good indication of the mean value of the InGaN alloy composition. By comparison with the Raman spectrum of the InGaN layer, an average In composition in the InGaN NWs of $\approx 25\%$ can

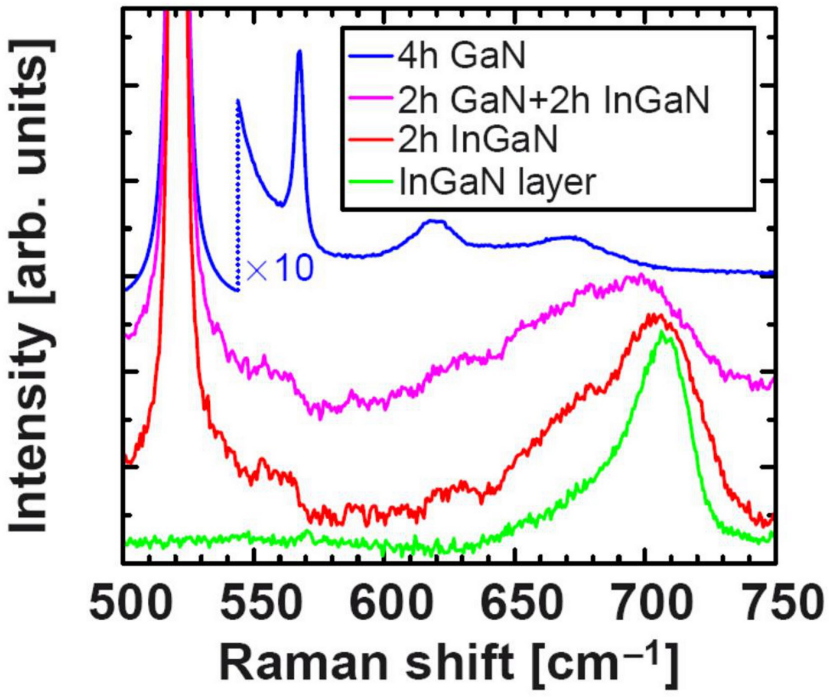

Figure 5.13: Room temperature Raman spectrum of the InGaN/GaN NW heterostructure sample (magenta) compared to the spectra of the GaN and InGaN NW reference samples. The bottom spectrum corresponds to an MOCVD-grown InGaN layer with an In concentration of 24%. The data was acquired by R. Cusco, Institut Jaume Almera, Barcelona

be estimated according to the composition dependence of the A_1(LO) frequency.[207] Raman measurements on the GaN NWs were performed away from resonance conditions and only a weak, sharp E_2 peak was detected at ≈ 567 cm^{-1}. The additional bands that can be observed in the Raman spectrum of that sample correspond to the first and second-order peaks of the Si substrate. In the InGaN/GaN NW heterostructure sample no GaN Raman signal could be detected as it was buried in the luminescence background.

The LO peak observed in the InGaN and InGaN/GaN NW samples displays an asymmetrical broadening to the low frequency side. This probably reflects In composition fluctuations across the nanowires (see above) and also within the ensemble of nanowires probed by the Raman measurement.[207] The LO peak of the InGaN/GaN NW heterostructure is clearly shifted to lower frequencies relative to that of the InGaN NW sample. Such a frequency shift could be related to a higher In content of the InGaN alloy in the NW heterostructure.

5.3. InGaN/GaN quantum wells and multi quantum well structures

For the final combination of all separate components of the LED within one NW not only a very basic knowledge of InGaN/GaN heterostructures is needed but rather detailed information on the creation of MQW structures in such NWs is required (see section 2.2). At this point the efforts described so far benefited greatly from the dedicated work of Martin Wölz on creating such MQW within GaN NWs. In the following section a short

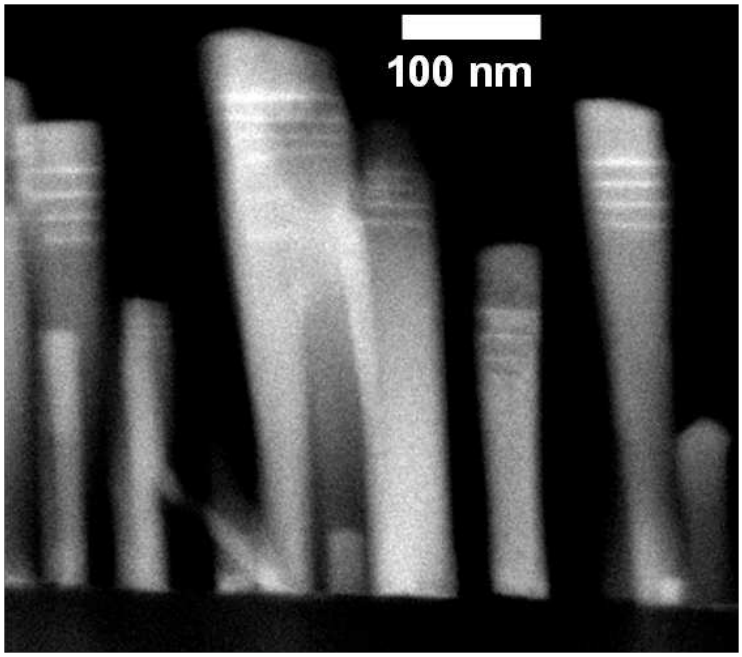

Figure 5.14: Z-contrast TEM image of GaN NW with an InGaN MQW. The data was acquired by A. Trampert, Paul-Drude Institut für Festkörperelektronik, Berlin.

summary of the insight gained in preparing the MQW structures, used for the NW LEDs described in chapter 6, will be given.

In Fig. 5.14 a Z-contrast TEM image of a GaN NW with an InGaN MQW is presented. The four horizontal bright lines represent the wells of the MQW structure within these wires. As one can see from this image the inhomogeneity in the wire height and diameter can lead to different barrier heights (compare e.g. the wire in the center with the second from the right). Also the InGaN QW height might be influenced in a similar way, yet the resolution of this image is not sufficient to clearly state this. Both effects can lead to the same problematic discussed for InGaN sections, namely that each wire has an individual InGaN composition.

MQW structures behave also similar to wires described previously with regards to the change in In incorporation with T_S (see section 5.1). Both a shift in the E_1(LO) peak of the Raman spectra and a shift in the peak energy of the PL can be observed (see Fig. 5.15). Also these structures showed very little dependence on changes in the In/Ga ratio. As it is not feasible to investigate every single MQW sample by TEM a method based on a laboratory XRD equipment was developed for measuring the achieved well and barrier thickness.[198,199] This allows a rapid check of the fabricated MQWs and enables direct feedback for the next growth runs.

Also for these structures the LS-QMS proved to be a valuable tool. It can be used to monitor the desorption of ^{115}In and hereby allows an *in-situ* calibration of the In source. In Fig. 5.16a) a typical LS-QMS signal for an InGaN/GaN MQW structure is displayed. In the initial phase the noise level rises due to the ignition of the plasma source. Upon opening of the N and Ga shutters the ^{69}Ga signal rises, followed by a decline signaling nucleation (see also section 4.1.1). For the remainder of the 90 minute GaN NW base growth the ^{69}Ga signal is rather stable.

Once GaN growth has terminated both Ga and N shutters are closed and the In shutter

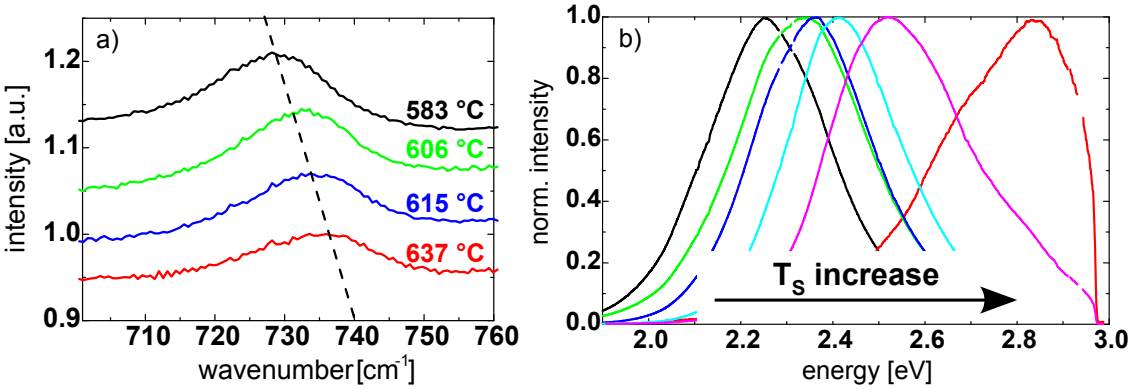

Figure 5.15: a) Raman spectra of InGaN/GaN MQWs grown at different T_S the shift in the E_1(LO) peak is indicated by the dashed line. b) Room temperature PL spectra of InGaN/GaN MQWs grown at different T_S. The excitation was at 3.0 eV and therefore below the GaN bandgap. The shift in the peak maximum is correlated with T_S. The Raman scattering data was acquired by M. Ramsteiner, Paul-Drude Institut für Festkörperelektronik, Berlin. The PL data was acquired by C. Hauswald, Paul-Drude Institut für Festkörperelektronik, Berlin.

is opened. The elevated T_S used for GaN growth lead to a total desorption of all the In supplied. Therefore the LS-QMS signal at 107 minutes (see Fig. 5.16b)) can be used as a relative measure of the total supplied In. Subsequent to this calibration of the In source, the In shutter is closed and T_S ramped down to temperatures suitable for InGaN growth. In Fig. 5.16 the four spikes in the ^{115}In signal between 120 and 155 minutes can be assigned to the In desorption during the growth of the four QWs. In this case In is incorporated in the NWs and therefore less material is desorbed. The difference in signal height compared to the calibration peak at 107 minutes gives only an indication of the In content in the QWs. In accumulation on the surface at low T_S along with small desorption rates, lead to a longer desorption rise times than at high T_S. Therefore, the desorption signal does not reach steady state conditions during the QW growth. Nevertheless, the use of the LS-QMS allows monitoring of the growth and can give additional insights for further analysis later on.

Conclusion

In this chapter InGaN was investigated as an active medium for LEDs. A special focus was put on InGaN segments on top of GaN NW bases. In particular, the proof that in fact InGaN was synthesized and the resulting peculiar shape of the InGaN cap were explored.[176] For long growth times of the InGaN segments, a core/shell type growth was found. The incorporation of InGaN QWs within the GaN NWs was investigated together with Martin Wölz, who has made a significant contribution by designing the MQW structures.

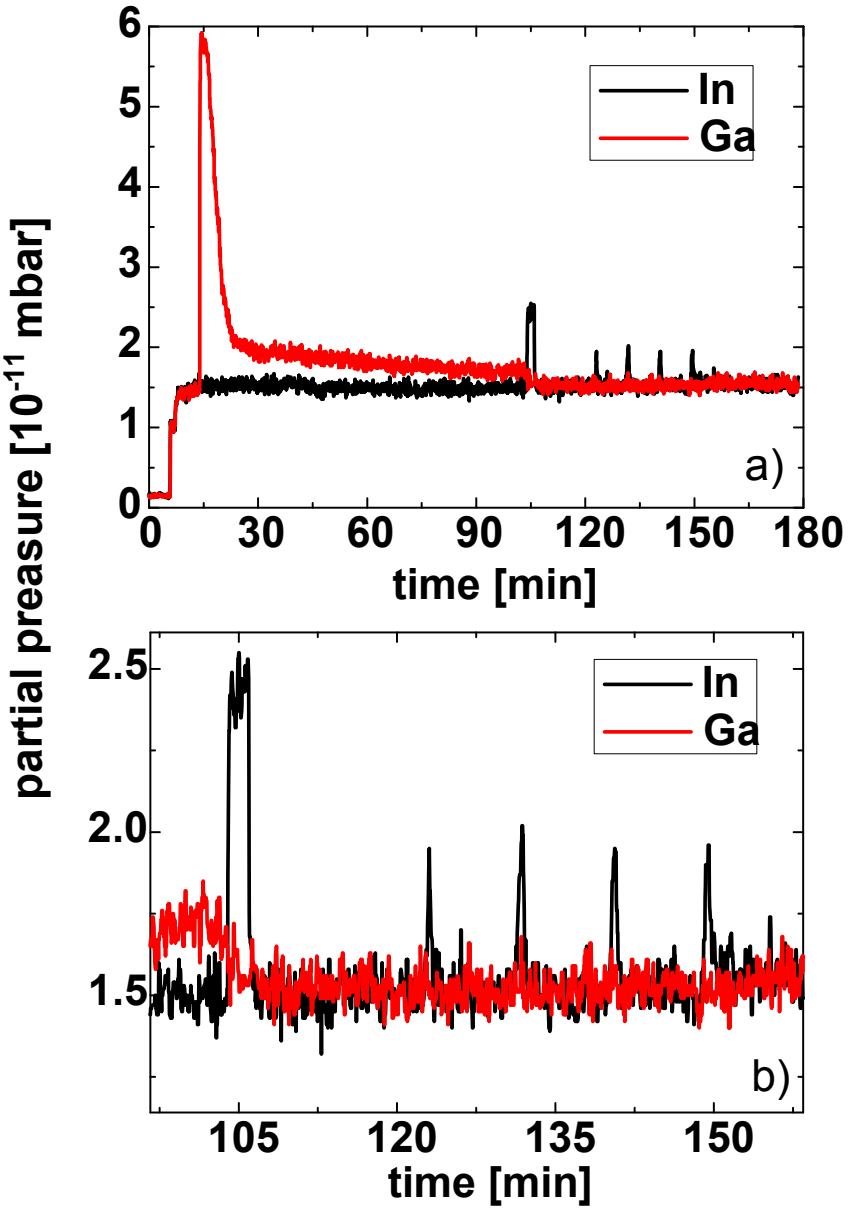

Figure 5.16: In-situ LS-QMS monitoring of the growth of an InGaN/GaN MQW structure by the detection of ^{115}In and ^{69}Ga. a) The LS-QMS signal of the first 165 minutes of growth including the GaN NW base, InGaN/GaN MQW and the subsequent GaN cap. b) LS-QMS signal just prior to and during the growth of MQW structure growth.

6. GaN-InGaN nanowire LEDs

In this chapter all the knowledge obtained by studying the doping of GaN NWs in chapter 4, and the insight gained in chapter 5 on the incorporation of In into the GaN matrix of the NWs is combined. The objective of this chapter is to describe the processing of GaN NW LED structures into working, light emitting devices and to characterize them. The ultimate goal of this thesis to integrate a III-V compound semiconductor device with Si MOSFET technology and to achieve their coexistence on a single wafer is described at the end of the chapter.
Especially the experiences gathered in controlling the morphology under the supply of a particular doping species are vital for producing a working n-i-p junction within single GaN NWs. The subsequent processing of the grown structures into a working device is described. Finally a structural analysis of a fully processed device is carried out along with the analysis of its electrical and optoelectronical properties. In section 6.6 the fabrication of a GaN NW LED on a wafer with Si based MOSFETs is described and an initial characterization is carried out. It will be demonstrated that the growth of GaN NW LEDs is compatible with Si back-end processing, which opens a way for the integration of light emitters with CMOS technology.

6.1. Growth and initial characterization

In order to produce a GaN NW-LED, heterostructures consisting of InGaN MQWs were grown within n-i-p diode structures. The MQWs act as active region for the recombination of holes and electrons and are undoped (see section 2.2). In Fig. 6.1 a schematic of the grown NW heterostructure is presented along with an SEM image of the grown NW ensemble. It is a general challenge for the doping of NWs that the complex growth mech-

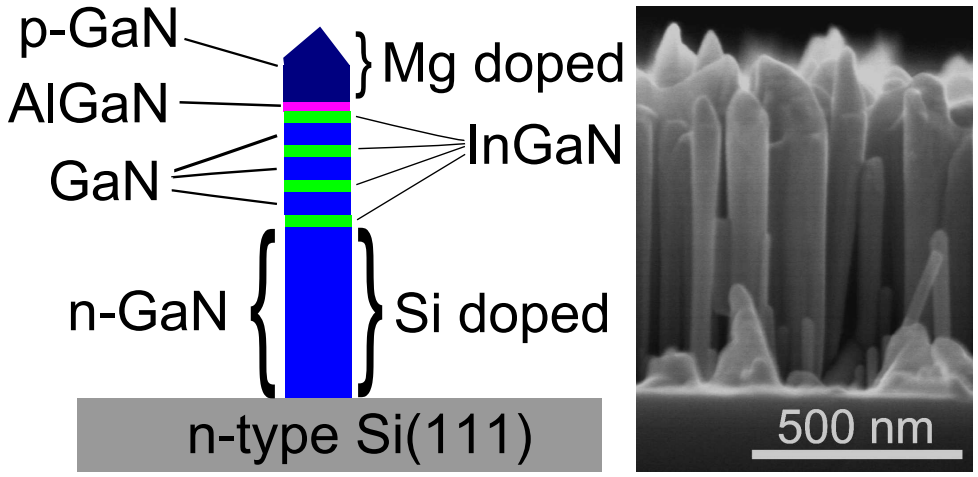

Figure 6.1: Sketch of the grown structure and SEM cross section image of the NW ensemble after MBE growth and prior to processing.

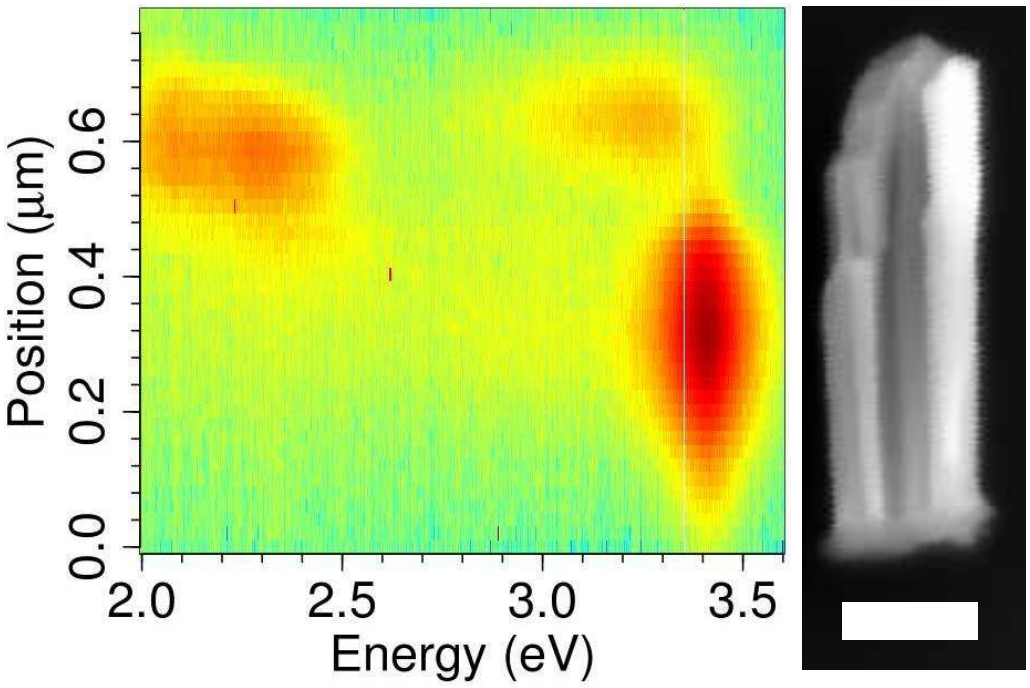

Figure 6.2: CL spectral linescan acquired at RT along the center of a GaN NW depicted in the SEM micrograph shown on the right. The CL intensity is color coded on a logarithmic scale. The scalebar in the SEM is 200 nm. The data was acquired by J. Lähnemann, Paul-Drude Institut für Festkörperelektronik, Berlin.

anisms can be significantly altered by the addition of doping species, see also sections 4.1 and 4.2.
Therefore, the growth of the Si-doped GaN base, special care was taken that the NW morphology was not affected by the supply of Si. With the knowledge gained through previous growth experiments the maximum Si flux was determined for which an impact on the wire morphology does not occur (reference layer calibration: $3 \cdot 10^{19}\,\mathrm{cm}^{-3}$), see section 4.2. Subsequent to the growth of the GaN:Si base at 780 °C, the substrate temperature was decreased to 604 °C in order to allow the incorporation of In into the GaN to form the wells.
The MQW structure consists of four wells each having an In content of 20% ± 10% and a height of 2 nm ± 1 nm, determined by x-ray diffraction on reference NW samples.[198,199] The barriers were designed to have a height of 8 nm. The last QW is immediately followed by a Mg-doped $Al_{0.15}Ga_{0.85}N$ electron blocking layer with a desired height of 13 nm. Finally, a Mg-doped GaN cap layer was grown. Once again, special attention was paid that doping did not destroy the NW morphology. A very low growth rate of only 0.8 nm/min was employed, in order to limit the degree of coalescence of the NWs as much as possible. For the same reason the growth temperature was gently raised by 140 °C to 754 °C at 2 °C/min during the initial stages of the cap growth and then held at 754 °C (see subsection 4.1.2).
The PL of the NW ensemble is as expected from the design (not shown). The NBE emission peak is visible along with luminescence associated with DAP transitions. At energies between 1.8 eV and 2.5 eV a very broad luminescence which originates from the InGaN QWs is observed. In order to determine the locations from which the individual contributions originate, CL spectra were acquired. In Fig. 6.2 a CL linescan taken at room tem-

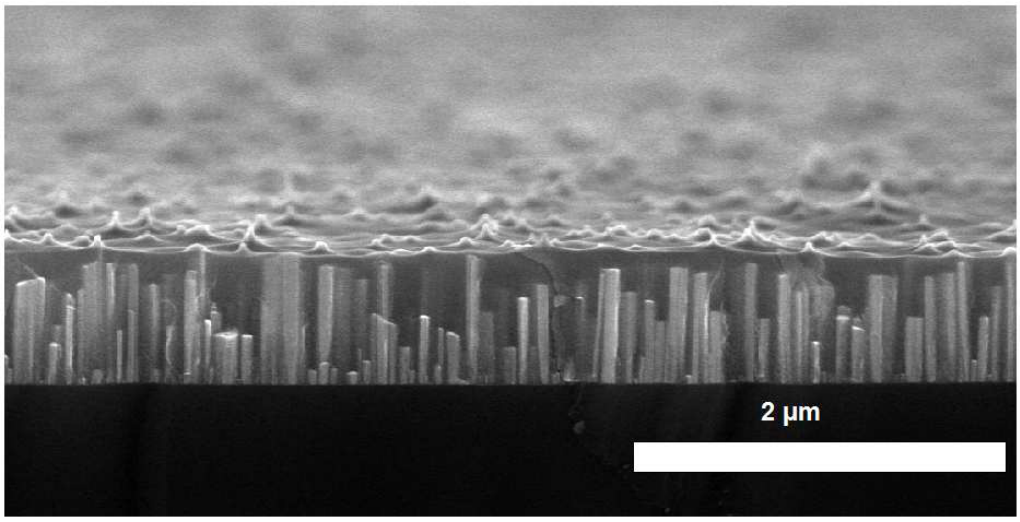

Figure 6.3: SEM cross-sectional image of a GaN NWs test sample. HSQ was spin coated and annealed three times.

perature of a single NW is shown. All three parts of the LED structure can be identified. The bottom 500 nm are dominated by the NBE luminescence of GaN as is expected for n-type GaN (see subsection 4.2.3). This segment is followed by the MQW structure and its broad luminescence centered at 2.2 eV. The origin of this luminescence and an explanation for the large FWHM are discussed in section 5.2. Finally the Mg-doped GaN cap of about 150 nm length can be identified by a redshift of the luminescence compared to the n-type region. This redshift indicates conduction band to acceptor transitions caused by incorporated Mg, see section 4.1.3.

6.2. Processing

While all the active semiconductor structures are prepared by MBE, the as-grown LED structure needs to be processed using several standard nanotechnology tools in order to allow the usage of the device. These processing steps enable the macroscopic contacting of the device and are described in the following paragraphs.
First, a $1.5 \times 1.5\,\mathrm{cm}^2$ piece is cleaved out off of the wafer used for the NW growth. This NW ensemble is planarized by spin coating a solution of HSQ resin in a carrier solvent of methylisobutylketone at 2000 rpm.[182] This solution is transformed into an amorphous SiO_x by thermal annealing in air at 350 °C for 30 min. One such step results in a filling of the space between the wire up to a height of approximately 250 nm. This height depends on the density of the NW ensemble, however it was found to be quite stable within the regime of NW densities encountered for the GaN NW LED growth. Three repetitions of HSQ application are necessary to cover the wires until only a few of them have their top most part above the layer plane. An example of such a filled up NW ensemble is presented in Fig. 6.3. In order to ensure that the filling is sufficient the sample is checked by SEM after the deposition of three layers and another layer is applied if required. The SiO_x acts as a dielectric in-between the wires and ensures that only the Mg-doped GaN is contacted with the front metalization. Even though the tips of some NWs might stick out of the SiO_x layer they are still covered by a thin coating of the dielectric, as can be

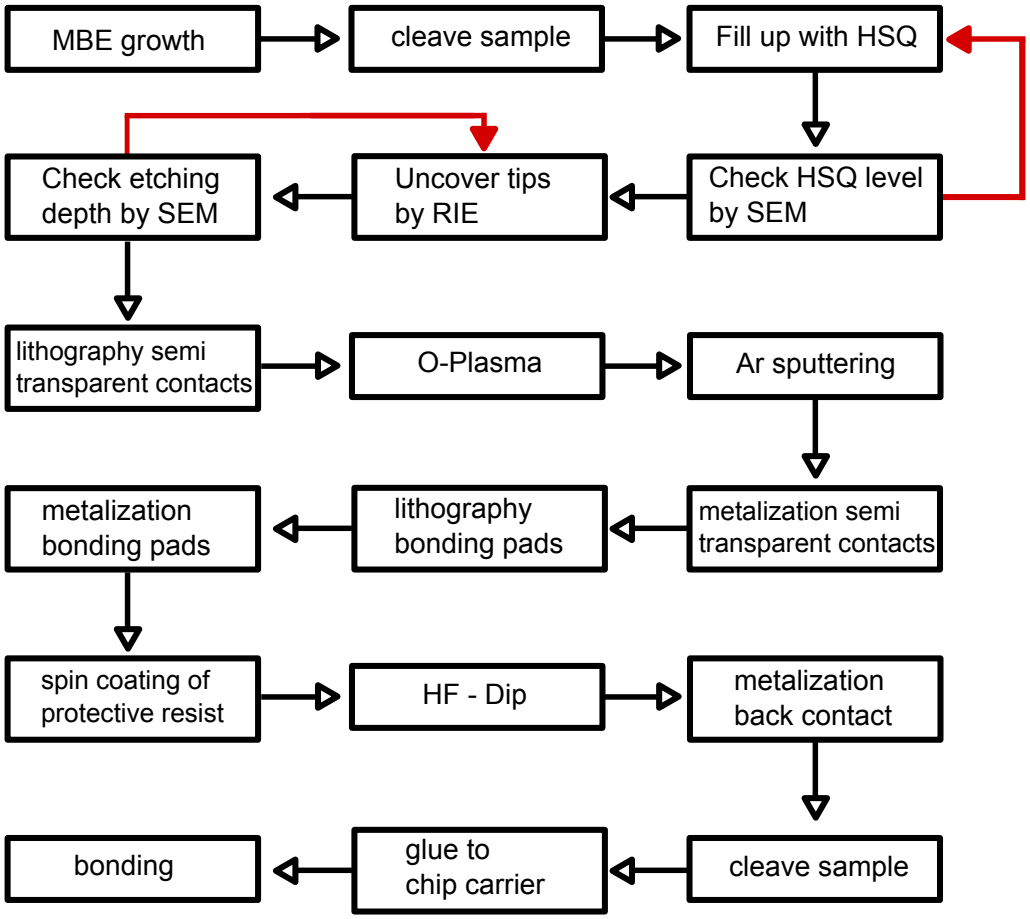

Figure 6.4: Workflow chart of the processing step for the fabrication of a GaN-NW LED after MBE growth.

seen in Fig. 6.3. In order to contact these p-type doped NW tips the oxide on top is removed by RIE using CHF_3 with a nominal etching depth of 30 nm. Depending on the exact thickness of the SiO_x layer 30 nm etching depth may not be enough to make the desired amount of wire tips available for contacting. Therefore the sample is checked by SEM also after this processing step. If the desired result is obtained, the semi-transparent Ni/Au (5 nm / 5 nm) top contacts are defined by optical lithography. After development the sample is subjected to a 5 s oxygen plasma cleaning followed by a 50 s Ar sputtering to ensure that no residues from the resist or oxides remain on the NW tips. Right after the deposition of the semi-transparent top contacts, the contact pads for bonding and current spreading are defined by optical lithography. The subsequent metalization is performed with Ti/Au (10 nm / 90 nm). Sketches of the sample geometry and SEM cross section images of some of these steps can be seen in Fig. 6.5. After the top side metalization, this side is covered by a protective photo resist and the back side is etched in a 3% HF-acid for approximately 10 s in order to remove the native oxide on the backside of the silicon wafer. The backside is then metalized with Al/Au (50 nm / 50 nm) to create the n-type contact. The protective resist is removed by cleaning the sample in acetone and isopropyl alcohol. In order to enable measurements in various setups the sample is cleaved and glued to a chip carrier with silver paste. The final step is the gold wire bonding between chip carrier and sample. All these steps are summarized in Fig. 6.4.

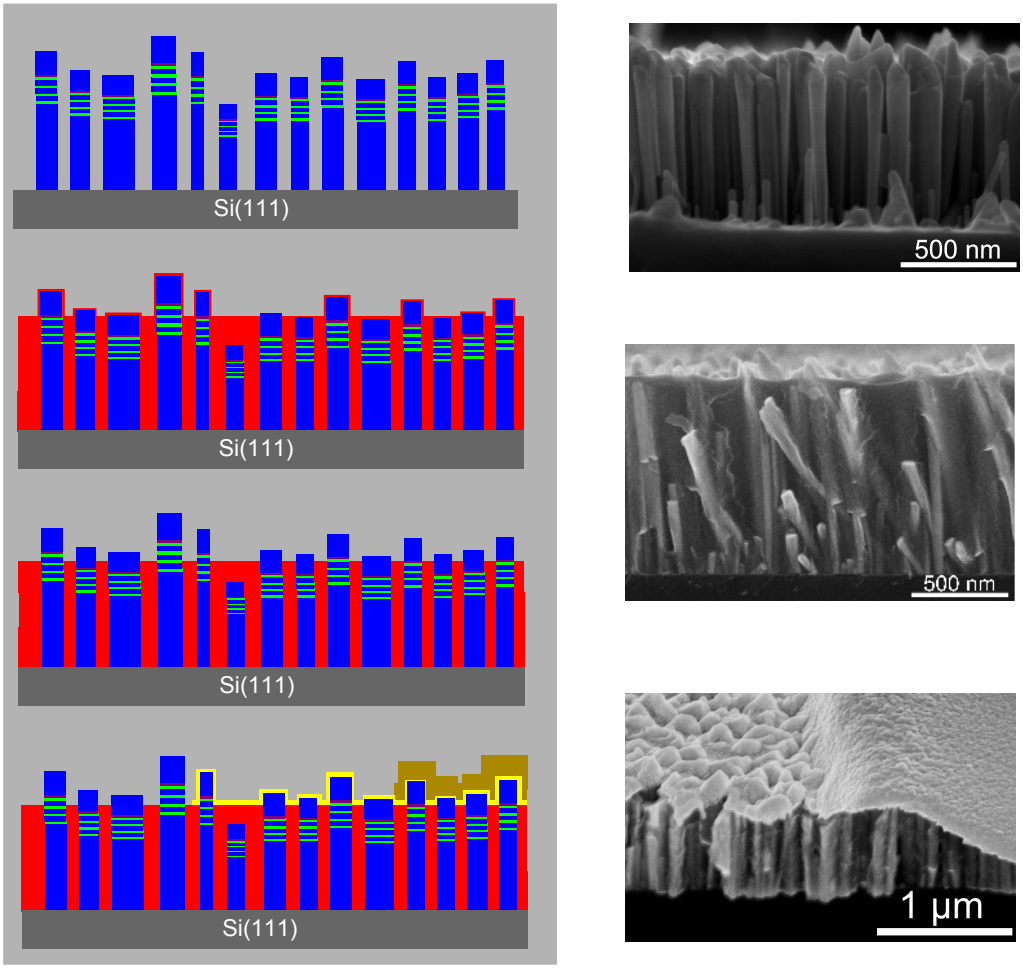

Figure 6.5: Sketches of the sample geometry after growth, filling with HSQ, uncovering of the tips and final metalization. Along with SEM cross section images after growth, filling with HSQ and contact metalization.

6.3. Post processing characterization

After the processing the GaN NW-LEDs were analyzed by cross sectional SEM and TEM. In the SEM images a very rough surface is visible where the semi transparent top contacts were deposited with individual wire tips sticking out from the HSQ layer. These tips are pyramidal in shape for most wires. The surface of the second top metalization is much smoother and hardly any trace of the wires underneath is obvious.
In the cross sectional TEM images presented in Fig. 6.6 all four metalization layers on top of the wires are clearly visible. Especially important is that the first two layers Ni and Au of the semi transparent contact are well connected from wire to wire. Another critical point in the processing is that Ni is in direct contact with the wire tips as desired, see Fig. 6.6b). This is the confirmation that the cleaning steps between lithography and metalization worked as aimed for. Also no extensive radiation damage which could have been caused by the Ar sputtering of the wires is clearly visible (no obvious amorphization). In addition stacking faults (SFs) are visible in Fig. 6.6a) approximately 100 nm − 150 nm below the NW tips. These might originate from the growth of the QWs as well as the electron blocking layer which otherwise do not give sufficient contrast in this imaging

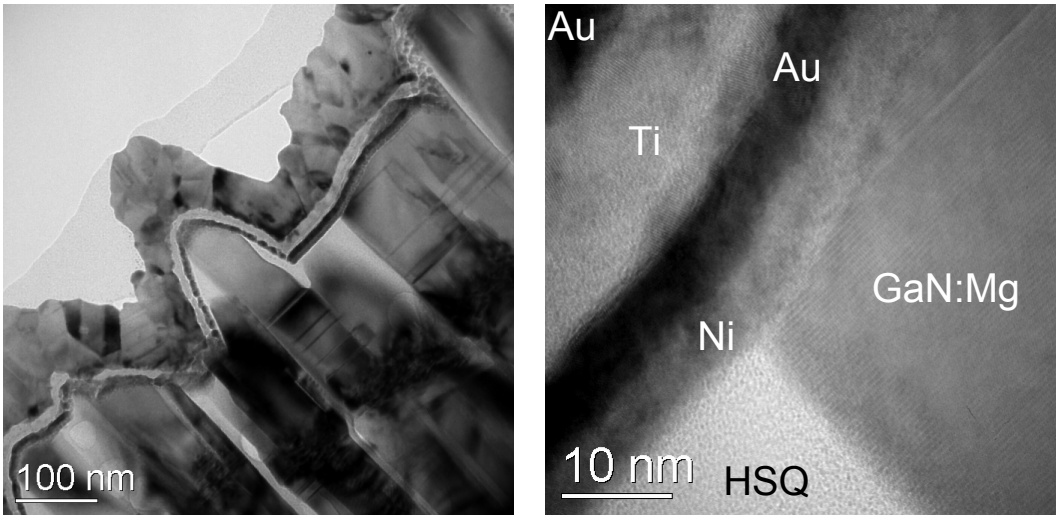

(a) (b)

Figure 6.6: (a) Bright field TEM cross section image of the contacted NW ensemble. (b) High resolution TEM image of a single NW and the interface with the metalization. In the bottom left the transformed HSQ of the planarization is visible. The data was acquired by A. Trampert, Paul-Drude Institut für Festkörperelektronik, Berlin.

mode. Also the low T_S employed during this stage of the growth might play a role in the formation of SFs.

6.4. Electrical properties

The NW-LED current-voltage characteristics of a contact pad of 0.2 mm^2 is presented in Fig. 6.7. The turn-on voltage of the device is approximately 5.2 V. The exact determination of this value is not possible as each NW-LED has its own turn-on voltage. Therefore the value of 5.2 V is only an average of turn-on voltages of the wires active at 8 V. This high turn-on voltage can in part be explained by the amorphous Si_xN_y layer between the NWs and the Si substrate (see section 3.1), but also the non-optimized processing techniques for contacting might give a significant contribution. The leakage current at -8 V is $1.5 \cdot 10^{-6}$ A/mm^2 which indicates a very good insulation of the individual wires by the SiO_x and is two orders of magnitude lower than what has been published previously.[62,209–211] The slope in the reverse bias regime is linear and therefore not as one would expect for a perfect diode. This behavior indicates the presence of a parallel current path with resistance R_p. Its value can be determined by using a line fit for the linear part of the reverse bias regime, see Fig 6.8 (see equation (2.15)). The observed parallel resistance has a value of $R_p = 27.3\,\text{M}\Omega \pm 0.1\,\text{M}\Omega$ which is rather good considering the not optimized processing for this device. Another feature which is not expected for neither an ideal diode nor a diode with a parallel resistance is the behavior between 0 V and -1.2 V. This is the effect of the amorphous Si_xN_y layer between the wires and the Si substrate[19] which acts as a tunnel barrier resistance that is in series with the NW-LED.
Also in the forward bias regime the current-voltage characteristic does not behave in an ideal way. Such a behavior is in part due to series resistances R_S in the current path. This is expected as both, the Si_xN_y interlayer present at the bottom of the GaN NWs (see

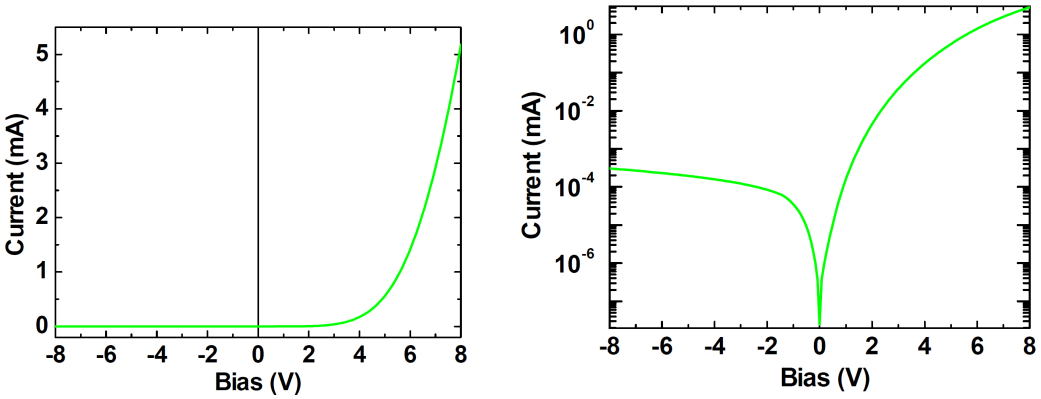

Figure 6.7: Current-voltage characteristics of the processed LED both in linear (a) and logarithmic (b) scale. The contact pad used for these measurements had an area of 0.2 mm^2.

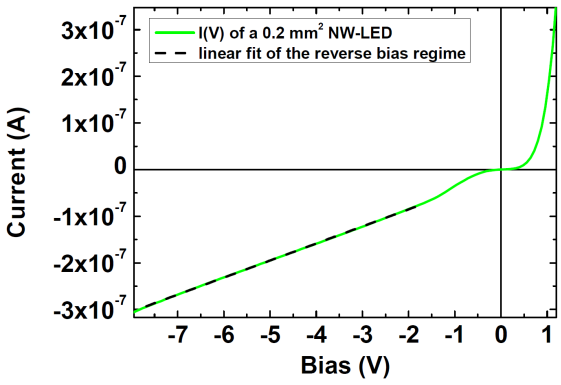

Figure 6.8: Plot of the reverse bias regime and linear fit at high negative voltages to determine the shunt.

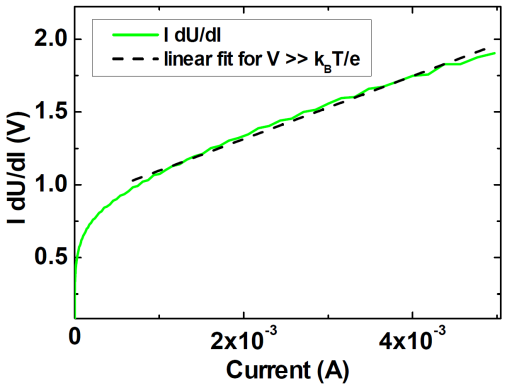

Figure 6.9: Plot of $I \cdot (dU/dI)$ versus I for determining R_S of the processed device.

section 3.1 and Stoica et al.[19]) and the not optimized processing of the contacts, represent resistors in series with the diode. Both contribute to the total resistance. In order to find the value of R_S the slope of a plot of $I \cdot (dU/dI)$ versus I is determined in Fig. 6.9 (see equation (2.17)). In order to extract a value also the device temperature is important, since a direct measurement is not possible the device temperature was assumed to be 400 K. The fact that the slope is not perfectly linear can be related to the contribution of the tunneling resistance of the Si_xN_y interlayer which would decrease at high bias voltages. Therefore a big error for R_S is associated with this determination. The linear fit of the slope results in a series resistance of $R_S = 220\,\Omega \pm 40\,\Omega$. The y-axis intercept of 0.88 ± 0.01 results in an ideality factor $n_{ideal} \approx 25$ which is significantly influenced by the assumption of a device temperature of 400 K. Due to the fact that the device holds approximately 10^6 individual NW-LED structures per mm^2, which are all connected in parallel, each with its individual ideality factor, it is not helpful to assign a global ideality

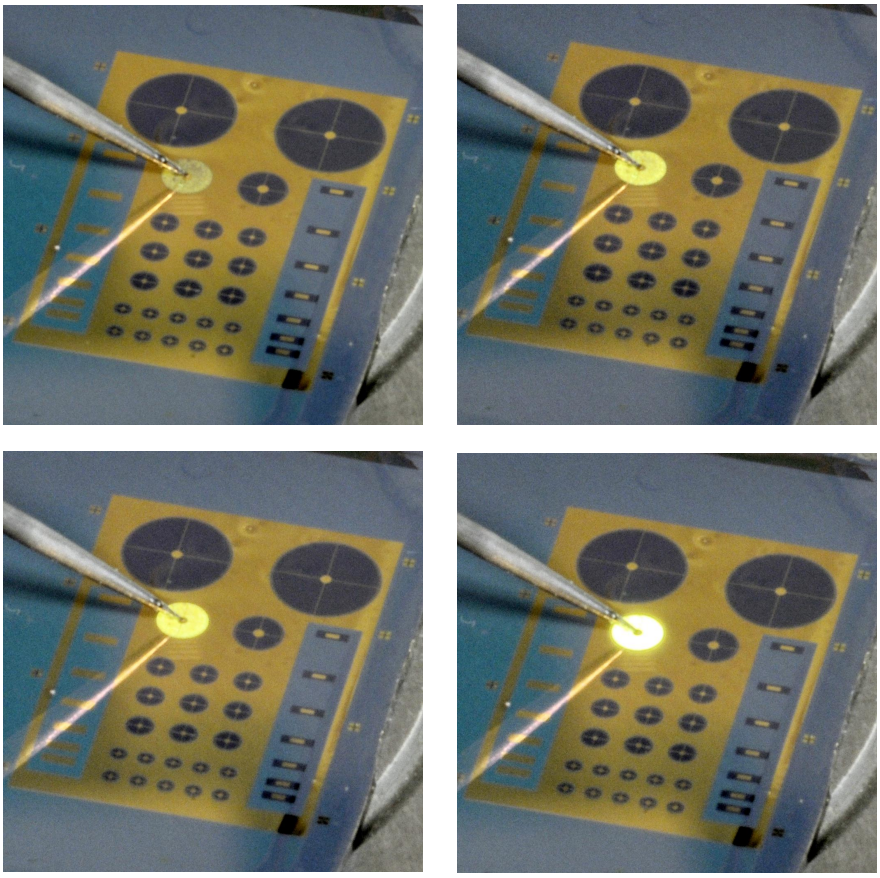

Figure 6.10: EL of a processed NW-LED under 4 V, 6 V, 8 V and 10 V forward bias.

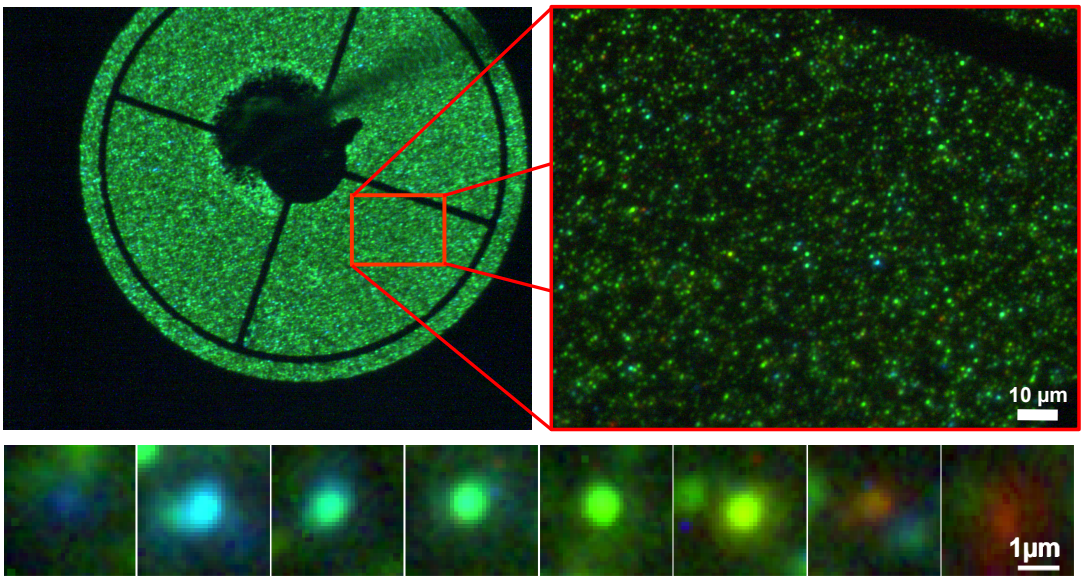

Figure 6.11: µ-EL of a NW-LED of 0.19 mm^2 under 10 V forward bias through a microscope at 200x and 500x magnification. Below are close ups of individual luminescence spots taken from the image with 500x magnification. The data was acquired by C. Hauswald, Paul-Drude Institut für Festkörperelektronik, Berlin.

factor for the device. By using R_S and R_p in equation (2.14) one can determine an upper bound for the saturation current $I_S \leq 10^{-9}$ A.

6.5. Electroluminescence

For the initial testing the devices were place on a probe station. The supporting chuck was used as the back contact and connected to ground. The bias was applied from the top through the contact needle of a micro-manipulator. In Fig. 6.10 a series of photos is presented with the NW-LED of 1 mm diameter under various forward bias voltages. It is clear from these pictures that the current spreading through the semi transparent contacts works very well. This is also the case for the even larger diodes with a diameter of 2 mm. Overall the EL can be seen with the naked eye at voltages around 4 V.

Even though the turn-on Voltage is 5.2 V, as determined from the current-voltage characteristic, one can observe significant luminescence already at 4 V forward bias (see Fig. 6.10). This fact is noteworthy and explained below. Especially considering that transmittance measurements of the semi transparent contacts reveal a 42% $\pm$ 7% transmittance in the relevant spectral region of 550 nm.

After this initial check with probe tips, the samples were glued to a chip carrier with silver paste and wire-bonded. This allowed μ-EL investigations of the samples. In Fig. 6.11 photos taken through a microscope at 200x and 500x magnification are presented while a forward bias of 10 V was applied. It is obvious that the NW-LED has a very spotty emission pattern. One can find emission spots with different colors ranging from blue all the way to red. Nevertheless the spot which exhibit green emission dominate by far. The size of the emission spots is at the resolution limit of the microscope settings and it is therefore suspected that each spot corresponds to a single NW emitting light.

The total number density of spots at 10 V is at around $1 \cdot 10^7\,\mathrm{cm}^{-2}$. This means that

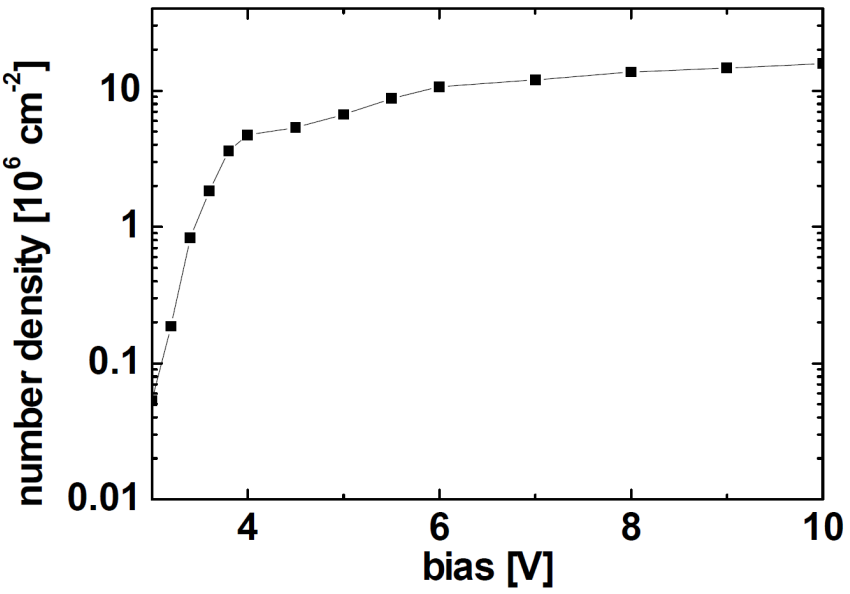

Figure 6.12: Number density of the luminescence spots as a function of the applied forward bias.

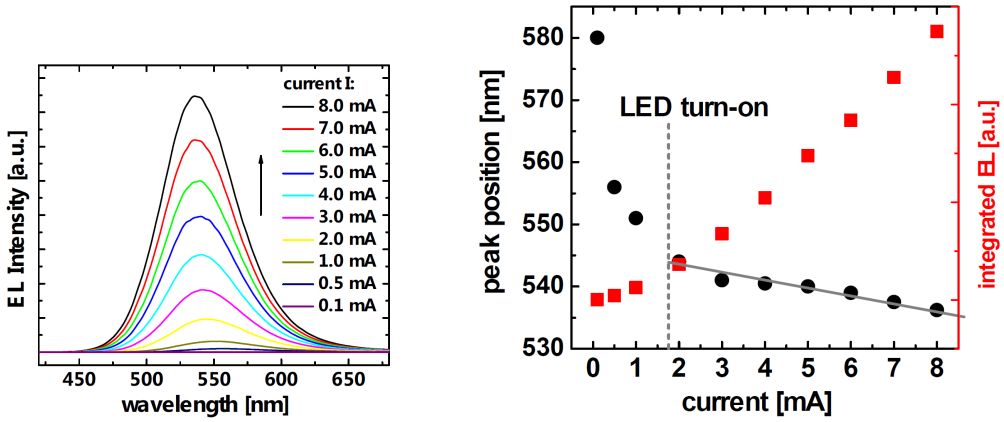

Figure 6.13: a) Spectrally resolved EL as a function of current. b) Plot of the EL peak position and its integrated intensity versus current. The data was acquired by C. Hauswald, Paul-Drude Institut für Festkörperelektronik, Berlin.

it is roughly two orders of magnitude lower then the wire density on the sample after growth. This may be caused by a number of reasons. The height distribution of the NWs and the planarization of the ensemble lead to the burial of some wires which are significantly smaller than the mean. On the other hand for wires that are significantly longer than the mean a contacting of the MQW structure or even the n-type base is possible. Luminescence would not be expected from either of these wire types. Furthermore the coalescence of some wires during the growth of the p-type cap would give rise to a single big structure and holes injected into it will choose the path of least resistance, meaning a diode with otherwise small series resistance. As the value for R_S is expected to be slightly different for each one of these diodes (slight changes in the layer thickness of the Si_xN_y for example may cause profound resistance differences) only one of the original NWs in the coalesced NW bundle will luminesce.

Also the turn on behavior of the NW-LED suggests that it can not be treated as a single device but rather needs to be understood as a collective contacting of several individual NW-LEDs all operated in parallel. Counting the luminescence spots at various forward biases one finds that already at 3.4 V a significant number of wires emit light (see Fig. 6.12). This is well below the turn-on voltage that is found for the device as a whole. Overall one can say that inhomogeneities between the individual wires can explain many of the observed phenomena described above.

Looking a the spectrally resolved EL the dominance of the green luminescence spots becomes obvious (see Fig. 6.13a)). In addition to the increased intensity of the light emission from the NW-LED an additional blue shift of the EL can be observed (see Fig. 6.13b)). This blue shift can be explained by the screening of an internal field within the QWs of the active region as more and more charge carriers are injected into the QW.[13,28] The bule shift below the turn-on voltage is most likely a superposition of the turn-on behavior of the individual wires and the screening of an internal field.

The integrated EL is increasing monotonously throughout the explored current injection range and no droop behavior was observed.[212]

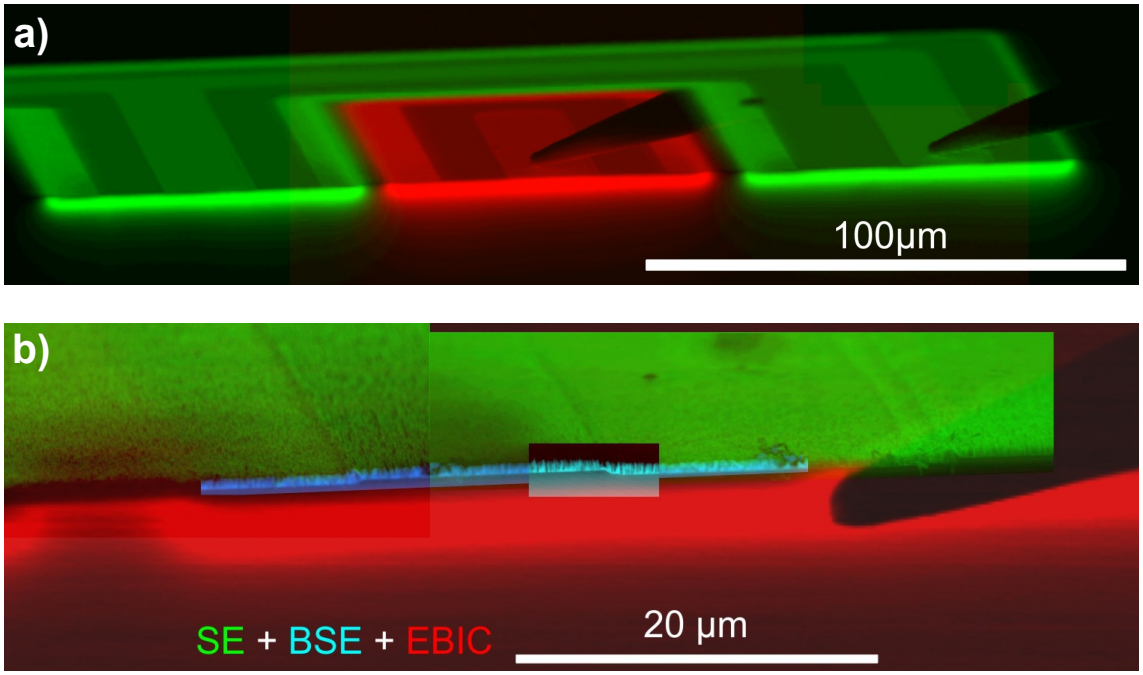

Figure 6.14: a) Overlay of two EBIC images of the MOSFET structure. The W-nanotip is on the source contact in one image and on the drain contact in the other. b) Overlay of one EBIC image, two SE images and two BSE images of the NW overgrown drain region of one of the MOSFETs. The data was acquired by J. Ledig, Technische Universität Braunschweig.

6.6. Nanowire LEDs for optoelectronic integrated circuits

One of the great long-term visions for the advancement of Si technology has been the integration of on-chip optical emitters which are compatible with standard, silicon-based ultra-large-scale integration technology.[213,214] A lot of research effort was put into producing efficient light emitters on the basis of silicon[215–222] and is still today. Another viable route may be the use of III-V compound semiconductor NWs which can act as light emitters on Si substrates (see previous sections).[62,64,65,209,211,223–226]
Group III and group V elements are only acceptable for complementary metal-oxide-semiconductor (CMOS) technology industry in back-end processing, due to their nature as dopants for Si. This results in some limitations for further processing. High temperatures will cause diffusion of doping species in the Si and might destroy or compromise the functionality of the CMOS device. The temperatures such devices can take, also called thermal budget, depends on their size, the doping atoms used and several other process parameters. For the most basic logic elements this budget is on the order of several hundred °C up to 850 °C.[3,227,228] For this reason it is difficult to employ MOCVD processes for the back-end creation of III-nitride devices on CMOS structures as the temperatures involved in this deposition technique are typically much higher. MBE growth of III-nitrides on the other hand offers growth temperatures which are within the range of the thermal budget for CMOS technology.
To date very few publications claiming the monolithic integration of III-V active devices with Si CMOS devices on the same wafer have been published.[229–231] Non of them describe the use of nitrides, if one disregards the publication by Furukawa[229] describing

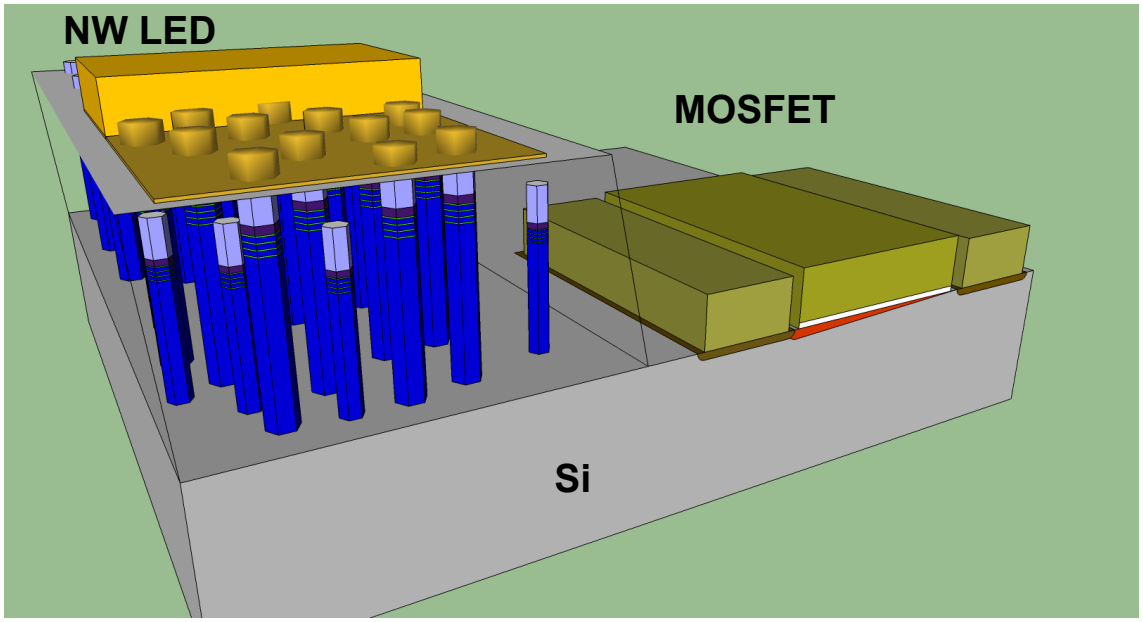

Figure 6.15: Sketch of a III-N NW LED and a Si based MOSFET on the same wafer.

a GaInPN device with 2% N-content. In this sense, the approach of using nitride nano structures for the monolithic integration of III-V and CMOS technology is unique.
This section demonstrates the compatibility of III-N NW growth and the subsequent LED processing with the simultaneous processing of a Si based MOSFET on the same wafer. The coexistence of a NW based LED on a Si wafer with a functioning p-MOS device demonstrates the usability of such structures as optoelectronic integrated circuits.
In order to create such a device, our partners from the Technische Universität Braunschweig prepatterned n-type Si wafers (500 Ωcm) in three different orientations ((100), (111) and (110)). Initially, the wafers were oxidized. The oxide was locally removed through optical lithography and wet etching, in areas where the source and drain regions were to be created. Through spin-coating of a Boron-emulsion and subsequent heating a in-diffusion of B is achieved, to form the source and drain regions. This was initiated but not carried out in full. The reason for this are the temperatures at which the MBE growth of the GaN NW LEDs takes place. The further B diffusion during the GaN NW growth was modeled and the initial in-diffusion adapted accordingly.
Subsequent to the first in-diffusion step all the structures on the wafer top are removed again. The wafer is then fully oxidized once more. This oxide will later on form the gate oxide of the MOSFET. The definition of the oxide between the source and drain regions was again carried out by optical lithography and wet etching.
After the patterning of the MOSFET structure up to the point of metalization, the samples were send to the Paul-Drude Institut für Festkörperelektronik (PDI). Here the growth of the NW LED structures was carried out in the same way as described in section 6.1. The only difference was the coverage of half of the wafer by the use of a shadow mask. The temperatures used for the growth of the NW LEDs can be viewed as a second diffusion step for the creation of the source and drain regions of the MOSFET. The covered half was afterwards used for the final processing of the MOSFETs while the half exposed to NW growth was fabricated into NW LEDs.
At this stage electron beam induced current (EBIC) imaging of the produced structures

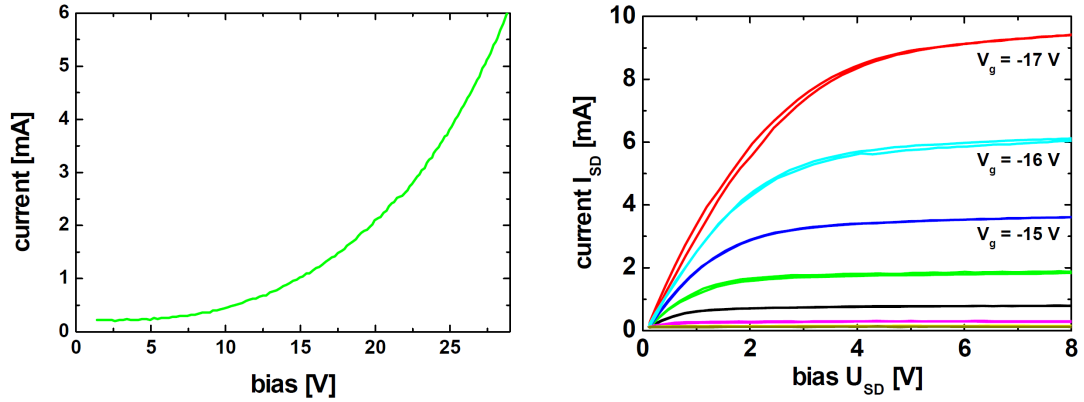

Figure 6.16: a) Electrical characteristics of a NW-LED grown on top of predefined partially processed MOSFET structures. b) Electrical characteristics of a MOSFET processed on the same wafer as the InGaN/GaN NW LEDs. The applied gate voltages V_G range from -11 V to -17 V in 1 V steps. The data was acquired by M. Erenburg, Technische Universität Braunschweig.

was performed on a cleaved sample. The EBIC signal is generated through the separation of electron hole pairs through internal electric fields such a p-n junctions. Such a junctions exists between the p-type doped source and drain regions of the MOSFET and the n-type Si wafer. Fig. 6.14a) shows a combined image of two EBIC images. The contrast was generated between a Si bulk back contact and a W-nanotip contact inside the contact window of drain and source areas at the cleavage edge at 0 V bias. In this case the examined position was covered by a shadow mask during MBE growth to prevent GaN NW LED growth on the transistors. Clearly visible is the formation of the p-n junction caused by the p-type doping of the source and drain regions (green and red color well below the wafer surface). In addition the channel position can be seen by the lack of signal between the two regions.
Fig. 6.14b) shows EBIC imaging (between nanotip and Si bulk back contact, at a reverse bias of 0.6 V) at the cleavage edge with a secondary electron (SE) and a back scattered electron (BSE) image overlay which show the GaN NW LEDs (not yet planarized and contacted) grown on top of the transistor. The field oxide is clearly visible by steps of around 250 nm at the surface (around 300 nm SiO_2 was expected) in the BSE image of Fig. 6.14b). The NW LEDs or the Si_xN_y layer have some lateral conductivity and hence short the drain and source contact windows of overgrown transistors which results in an EBIC signal from both source and drain regions at the same time (left hand side of Fig. 6.14b)).
After growth of the GaN NW LEDs the MOSFET side of the wafer was dipped into 3% HF for 3 seconds in order to remove the native oxide on the predefined windows for source and drain. Directly after the HF etching this half of the wafer was metalized with 200 nm of Al.
These steps were followed by the processing of the NW LED as described in section 6.2. After an initial test of the LEDs the samples were sent back to the Technische Universität Braunschweig where the final processing of the MOSFETs was carried out. First of all the SiO_x layer on top of the Al, caused by the application of HSQ during the LED processing, is removed through dry etching with CHF_3. Subsequently the Al layer was removed

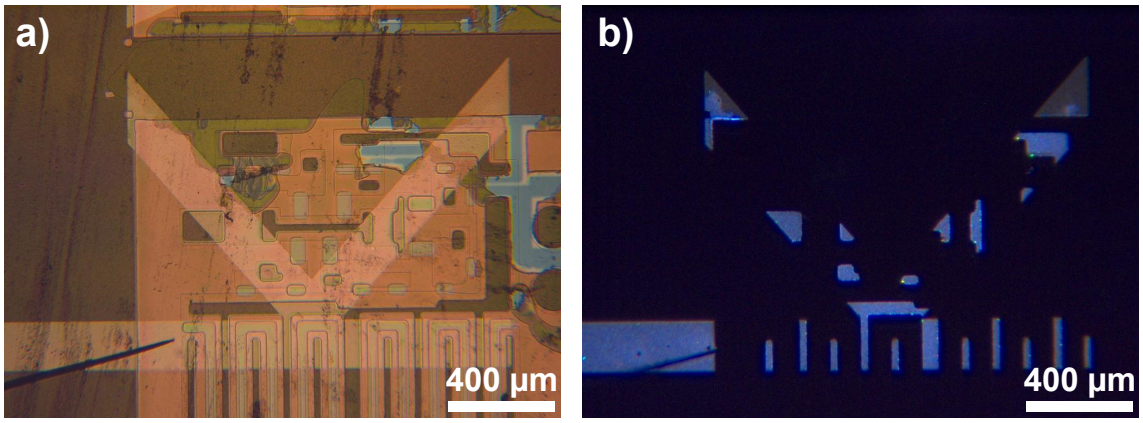

Figure 6.17: a) Microscope image of the NW-LED and MOSFET design. b) Electroluminescence of the NW-LED observed at the same magnification as the microscope image in a). The data was acquired by M. Erenburg, Technische Universität Braunschweig.

everywhere but at the source and drain region where it acts as contact metalization. The selectivity was again provided by optical lithography and wet etching.
Fig. 6.15 shows a sketch of the outcome after processing of the two devices. They are spatially separated but in coexistence on the same wafer. In reality the NWs have predefined structures underneath them at several locations. Only at a few places the NWs are placed directly on top of the bare Si. This results in a drastic deterioration of the electrical characteristics of the NW LEDs. The I-U characteristics are displayed in Fig. 6.16a) and show a very high turn-on voltage of ≈ 14 V. Nevertheless, the NW LEDs still retain their rectifying diode characteristics and EL is visible. Also the MOSFETs have suboptimal characteristics as the gate voltage required to switch the transistors is rather high. The gate voltages V_g displayed if Fig. 6.16b) range from -11 V up to -17 V in 1 V steps. In both cases there is a lot of room for improvement, as the processing of the combination of these kinds of devices was tried only for this series of samples and therefore for the first time.
One simple improvement is the processing of the MOSFET structures also only on one half of the wafer which would place the NW-LEDs directly on the Si. This should yield similar characteristics for the LEDs as described in section 6.4 and 6.5. The flaws of the design utilized so far can be seen in Fig. 6.17. The left image shows a microscope image of the NW-LED and the MOSFET structures on top of one another. The structure resembling the lying *k* is the metalization for the NW LED top contact. All the other structures are either SiO_2 on top of the Si surface or source drain areas, both were defined prior to the NW growth. In the EL image of Fig. 6.17b) it be comes obvious that a significant portion of the NW-LED is not functioning due to the underlying structures.
Even though the electrical characteristics are sub optimal it was possible to extract an EL spectrum. This spectrum is presented in Fig. 6.18. Other than the spectra obtained and discussed prior to these experiments the EL spectrum shows two distinct peaks, one at 500 nm and another one centered at 700 nm. The reasons for these differences are not clear an require an intensive investigation, as the NW LEDs were grown with nominally the same parameters. One significant difference between the samples discussed in sections 6.4 and 6.5 and the ones discussed in this section, is the time in which they were grown. The MBE machine was not opened between the two growth campaigns but 6 month passed in between the two campaigns. Some shift in the parameters might be the

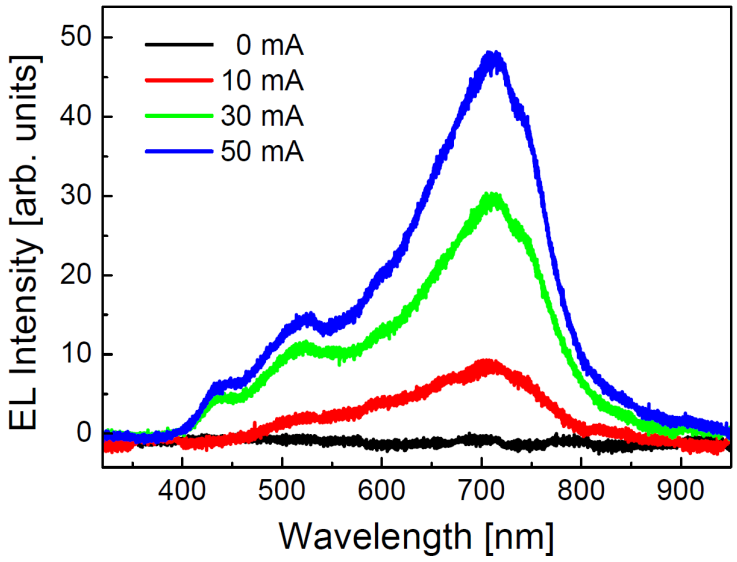

Figure 6.18: EL spectrum of a NW-LED on a wafer with MOSFETs. The data was acquired by C. Hauswald, Paul-Drude Institut für Festkörperelektronik, Berlin.

explanation for the different spectral behavior.
Even though the two devices are spatially separated on the wafer they can be connected via probe needles and cables. This allows to control the NW-LED through the transistor gate voltage V_g at a fixed bias U_{SD}. The measured characteristic of this experiment is presented in Fig. 6.19. The conduction channel below the gate starts to open at around V_g = -8 V. Increasing the gate voltage allows more current to pass through and therefore to reach the NW LED. At V_g = -14 V the diode becomes the limiting factor for I_{LED} as the fixed bias of U_{SD} = 35 V does not allow a current of $I_{\mathrm{LED}} > 9$ mA for the specific device under test.

The described results were found to be representative of all three wafer orientations ((100), (111) and (110)) tested. No significant difference between them could be identified.

Conclusion

In this chapter, all the knowledge on the single components of an LED in GaN NWs was combined to form an actual LED structure. The NW LEDs were subsequently processed collectively into a macroscopic LED which was then characterized by electrical and optical methods. The produced LED proves that NW LEDs are feasible. The processing technology leaves a lot of room for improvement of the performance using the current design.
Finally, the NW LEDs were grown and processed on top of a partially processed MOSFET. The MOSFET processing was subsequently concluded. The result was a functioning III-V semiconductor LED on the same wafer as elementary Si based logic elements. These experiments were repeated on wafers with three different orientations and the achieved results were the same for all of them. Being able to drive the LED via a MOSFET structure on the same wafer represents true integration of III-V opto-electronics with large scale Si based micro electronics.

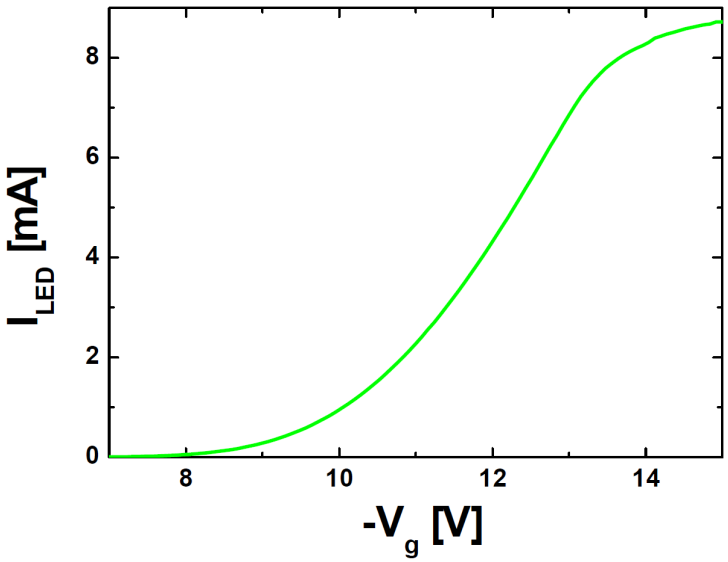

Figure 6.19: NW-LED current I_{LED} as a function of gate voltage V_g of a MOSFET on the same wafer. The data was acquired by M. Erenburg, Technische Universität Braunschweig.

7. Conclusion and outlook

This chapter briefly summarizes the results of the entire thesis and gives an outlook on further experiments and technological advances using the tools which are now at hand.

Conclusion

The investigations conducted for this thesis were motivated by the interest in semiconductor NWs, the desire to produce a working device based on such NWs and its integration with Si technology. The III-N material system was chosen due to its relevance for solid state lighting.[27] The main driving force to use GaN NWs as a medium for solid state lighting is the lack of a suitable substrate for GaN growth. NWs have the potential to resolve this issue due to their small footprint.
In this thesis, the integration of GaN based NWs LEDs with the quintessential semiconductor substrate Si is studied in detail. The main aims were as follows:

- to investigate the changes in growth behavior and morphology which occur when doping species such as Mg and Si are supplied to the MBE growth of NWs.
- to synthesize InGaN QWs within GaN NWs and to achieve control of the In composition.
- to process GaN NW LED structures into a working, light emitting device and characterize it.
- to integrate a III-V compound semiconductor device with Si MOSFET technology and to achieve their coexistence on a single wafer.

GaN NWs have been grown by self assisted mechanism in plasma-assisted MBE. Studies of the pure GaN NW growth were used, in combination with the experience gained through previous studies,[112,232] as a basis for comparison with the growth under the supply of additional atomic species.
Both p- and n-type doping species were investigated. Namely, Mg as an acceptor and Si as a donor. Mg doping proves to have a significant influence on the growth behavior of GaN NWs. Their nucleation occurs much faster in the presence of Mg[118] and also their lateral growth rate is increased. The thesis that Mg incorporation at low T_S is increased could not be prooven, yet the evidence does not contradict this notion either.[150]
N-type doping of GaN NWs is less important from a technological point of view, as the nominally undoped NWs are already n-type. Nevertheless, Si doping can enhance the conductivity of the NWs. Also Si has an influence on the growth dynamics of self-assisted GaN NWs. It leads to inverse tapering and a loss of orientation with respect to the substrate. A Si flux was found at which the morphology is only slightly effected while the conductivity is enhanced at the same time.
Nominal p-i-n and n-i-p junctions within GaN NWs were synthesized and investigated. A strong difference in the optoelectronic properties upon reversing the doping profile

was found, in that especially the acceptor concentration varies significantly. An improved incorporation of acceptors is achieved when Mg is supplied at the NW top. The technologically relevant information extracted from this result is that the doping sequence for a NW pn-junction needs to start with Si doping and end with Mg doping.
Within the scope of this thesis, InGaN was investigated as an active medium for LEDs. A special focus was put on InGaN segments on top of GaN NW bases. In particular, the proof that in fact InGaN was synthesized and the resulting peculiar shape of the InGaN cap was explored.[176] For long growth times of the the InGaN segments, a core/shell type growth was found. The incorporation of InGaN QWs within the GaN NWs was investigated together with Martin Wölz, who has made a significant contribution in designing the MQW structures.
All the knowledge on the single components of an LED in GaN NWs was combined to form an actual LED structure. The NW LEDs were subsequently processed collectively into a macroscopic LED which was then characterized by electrical and optical methods. The produced LED proves that NW LEDs are feasible. The processing technology leaves a lot of room for improvement of the performance using the current design.
Finally, the NW LEDs were grown and processed on top of a partially processed MOSFET. The MOSFET processing was subsequently completed. The result was a functioning III-V semiconductor LED on the same wafer as elementary Si based logic elements. This represents true integration of III-V opto-electronics with large scale Si based micro electronics.
In conclusion, we find that, through overcoming or dealing with the effects of additional atomic species during growth, GaN based NW LEDs can be fabricated. A processing scheme was developed and the integration of Si based logic and III-V opto-electronics was achieved.

Outlook

A significant deficit of the GaN NW LEDs fabricated is the fact that only about 1% of all the NWs on a given sample actually emit light. Increasing this percentage would dramatically increase the lighting efficiency per area of these devices. Possible reasons for this low yield in luminescing NWs were discussed in section 6.5. Another flaw in the current design is the polychromatic appearance of the NW LEDs. While they were designed to have a specific color, the EL of the ensemble is rather broad with individual wires having very well defined but different emission colors. This is ascribed to the non uniformity of the neighborhood of an individual NW as well as to the non uniformity in morphology from NW to NW. These differences might lead to different In incorporation rates during the growth of the active region. For these reasons it is desirable to create a much more uniform NW LED ensemble.
Selective area growth (SAG) of GaN NWs may be the tool needed to overcome these difficulties and to achieve the desired uniformity. Dr. Tobias Gotschke developed during his PhD. thesis a technique to selectively grow GaN NWs (SAG) using a metal free mask.[113] Some of his results are presented in Fig. 7.1. SAG allows the creation of a homogeneous neighborhood for all NWs and also enables the synthesis of NWs with very similar morphologies at the same time. The more homogeneous conditions during growth will most likely lead to a more predictable and uniform In incorporation. In addition, the final height of the grown NW will be found within a smaller window of the length distribution, enabling a much higher success rate in contacting the NWs of such an ensemble.

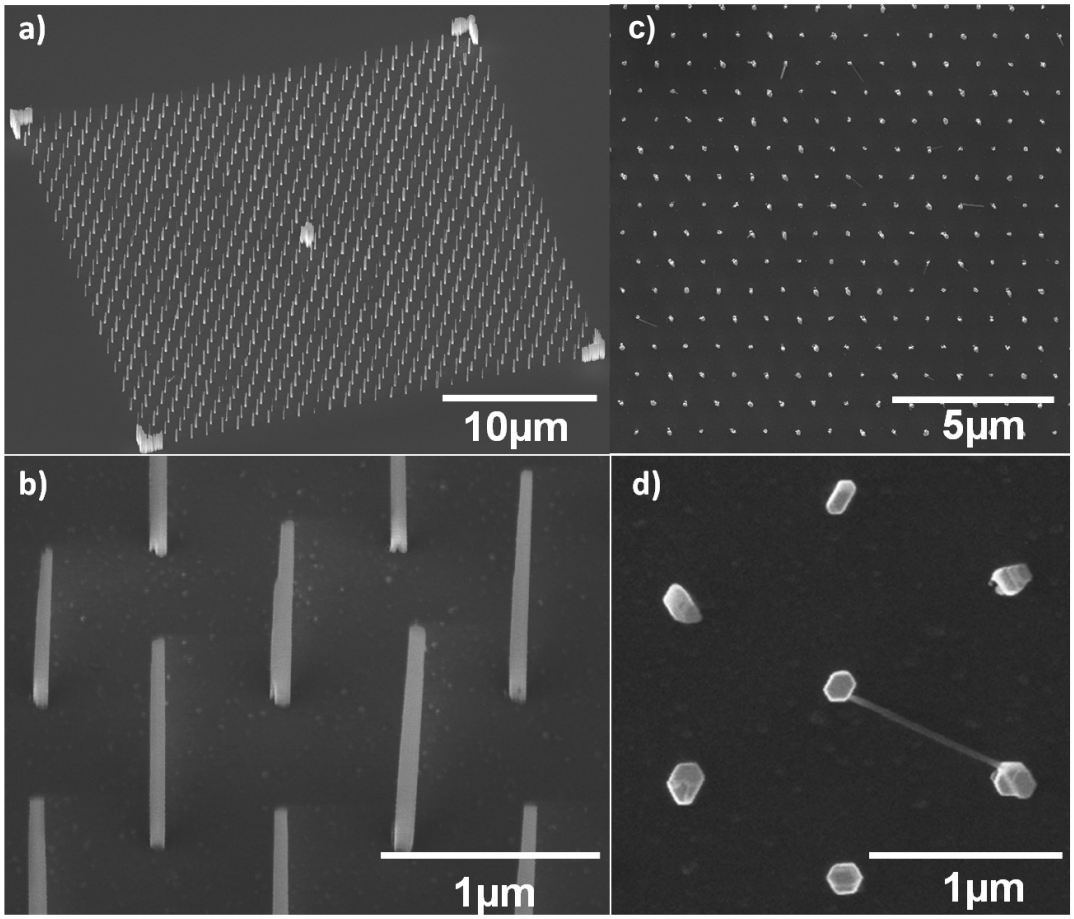

Figure 7.1: Selective area growth of GaN NW.[113]

This technology is compatible with the processes used in the present thesis for the successful fabrication of a NW LED. The selectivity will be lost during the growth of the active region of the LED but this should have no influence on the growth behavior of the well developed NWs which will be contacted in the end. Some of the active area will be lost due to the needed spacing between the wires. Assuming that all of the SAG grown NWs exhibit EL an increase in the number density of NW which show EL from now $1 \cdot 10^7\,\mathrm{cm}^{-2}$ to $5 \cdot 10^8\,\mathrm{cm}^{-2}$ is feasible by using a 440 nm spacing.
The next step, regarding the integration of the NW LEDs with Si based logic, will be to place the NW LEDs directly on the drain area of an n-MOSFET and use it as the back contact. This will allow direct control of the NW LED on a Si chip by the application of a gate voltage. An array of this kind of devices may be used as a display or an on-chip optical interconnect to convert electrical information into light pulses.

A. Appendix A: Calibration of the growth parameters

At the PDI, AlN, GaN and InN layers were grown under N-rich conditions at low temperature (low enough to have no significant desorption), in order to calibrate the Al, Ga and In flux. This ensures that all of the supplied material is incorporated into the growing layer. A subsequent measurement of the thickness of these layers allows to calculate a system independent growth rate with the unit nm/min. Likewise, a GaN layer was grown under Ga-rich conditions, in order to calibrate the N growth rate.
The substrate temperature was monitored through the detection of infrared radiation with a pyrometer.
A calibration in form of a growth rate was not possible for both doping species (Si and Mg) as the amount of material used was insufficient to create a measurable layer.
No such growth rate calibrations were conducted for the samples grown at the FZ Jülich. In their case only the BEP values of the group III metals are known.
In the next paragraphs, a conversion of the BEP values, measured in Jülich, into the system independent growth rate is conducted. This conversion was done by Dr. Tobias Gotschke and can be found also in his PhD thesis.[113] It is subject to various errors and can not be exact. The main reason for this conversion is to create consistency in the use of growth parameters throughout the thesis.
In general, BEP values of different MBE systems are not directly comparable. They are subject to the given geometrical layout of the system and the effusion cells. Especially the distance between effusion cell and substrate is of importance, but also other parameters play a role. Furthermore, no layers were grown at the FZ Jülich. This leaves only the structural comparison of various NW samples for matching the parameters of both systems. Since length, diameter and density of the NWs are dependent on T_S, metal and N flux, a direct comparison does not yield the desired growth rates. In the PhD thesis of Dr. Tobias Gotschke it is stated that the SAG growth of GaN NWs is N-limited at the beginning of the growth and Ga-limited for longer growth times. Using two SAG NW samples from each system with different growth times (2 h and 4 h) allows an estimation for the Ga flux. This results in a growth rate of 2 nm/min at the FZ Jülich for the used T_{Ga}. Assuming that the diffusion length is in the same order of magnitude for the two experiments, one can estimate a N flux of 18 nm/min.
The determination of the In flux is less exact as the growth of InN NWs is less well understood. This leaves only the comparison of morphologies.
The calibration of the Al flux on the other hand is rather precise. Also at the FZ Jülich AlN layers were grown which allows direct comparison.
In table A.1, the conversion from FZ Jülich BEP values to growth rates is summarized along side with the values of the MBE system at the PDI. Since the BEP values are proportional to the growth rates, this table allows the re-determination of the original BEP values using the nm/min values given in the text above.

	FZ Jülich		PDI	
Element	BEP [mbar]	growth rate	BEP [mbar]	growth rate
N	$1.2 \cdot 10^{-5}$	18 nm/min	$1.2 \cdot 10^{-5}$	13 nm/min
Al	$1.2 \cdot 10^{-7}$	4 nm/min	$3.7 \cdot 10^{-7}$	4 nm/min
Ga	$1.2 \cdot 10^{-7}$	3 nm/min	$7.0 \cdot 10^{-7}$	3 nm/min
In	$4.0 \cdot 10^{-8}$	2 nm/min	$3.3 \cdot 10^{-7}$	2 nm/min

Table A.1: List of BEP and growth rate values for the two used MBE systems.

B. Appendix B: Shadowing effect

In a standard MBE chamber, the effusion cell ports are mounted at a specific inclination with respect to the surface normal of the substrate. This results typically in slight inhomogeneity of the material flow at the substrate. In thin film growth, this problem is overcome by sample rotation at an appropriate speed depending on the growth rate of the film.[110,233] For NWs on the other hand the inclination of the cells does not only cause inhomogeneities in material supply but also shadowing of one NW by another. This is not overcome by simply rotating the sample.
These shadowing effects are mentioned at several occasions in the thesis as causes for the observed phenomena. Simulations were performed in order to quantify at what NW height this shadowing effect is relevant.
A top view image of NWs just after nucleation was acquired. The positions of 3097 NWs were determined and used as experimental input for the simulation. Length and diameters were assigned to these wire positions according to the distribution statistic found in investigations, such as the ones described in section 3.1. This was necessary, as it is not possible to determine the x- and y-coordinates as well as the according length and diameter for a large number of wires at the same time.
After this initialization, the NWs were increased in size with a 20 times higher axial growth rate compared to the radial one. After each growth step of 50 nm axial growth the percentage of covered surface area was calculated for several effusion cell inclinations. The inclination angle used in the following discussion is always measured away from the substrate normal.
The results of the simulation are displayed in Fig. B.1. Fig. B.1a) shows the coverage of the substrate which is either caused by a NW or a NW shadow as a function of the NW mean height. This means that the covered area can not be reached anymore by impinging atomic species. Instead these impact on NW side walls or top facets. The horizontal dashed line indicates a coverage of 90%, the vertical one indicates the height at which 90% of the substrate is covered in the case of the Ga effusion cell of the MBE at the FZ Jülich (34°).
The variation for the two MBE systems used is not significant for most of the cells. Only in the case of the cells supplying the doping species the difference is noteworthy. In Jülich a tandem cell for both species (Si and Mg) was used which has an inclination angle of 42°. This cell was for example used for the fabrication of the samples discussed in sections 4.3 and 4.1.2 to 4.1.3.
Fig. B.1b) shows the mean height at which 90% of the substrate is not accessible to the impinging atoms anymore as a function of the cell inclination. The plateaus in this plot are artifacts of the simulation and due to the step size of the NW length growth (50 nm).

For the given geometrical configurations of the MBE chambers, these results demonstrate the importance of shadowing at a mean height of around 400 nm for the NW ensemble. This value is of course only valid for a given set of growth parameters as they will influence this value. T_S and Ga flux for example can lead to different NW densities and therefore change the results. Nevertheless, such a value can act as a guideline at which NW height attention needs to be payed to shadowing.

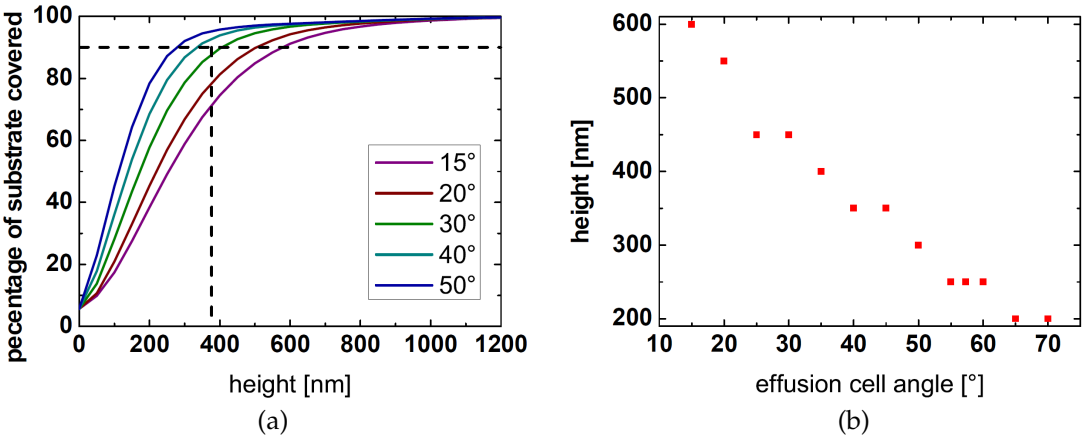

Figure B.1: NW shadowing simulation with experimental input of height, diameter and position. a) Percentage of the substrate which is either covered by a NW or a NW shadow as a function of the NW mean height. The horizontal dashed line indicates a coverage of 90%. The vertical one indicates the height at which 90% of the substrate is covered in the case of the Ga cell in the MBE at the FZ Jülich. b) Mean height at which 90% of the substrate is not accessible to the impinging atoms as a function of the cell angle.

In this simulation, only the showing of the substrate by the growing NWs is considered. Yet one also needs to consider the influence of shadowing among the NWs. With the given typical number densities of 10^{10} cm^{-2} a majority of the NWs already suffers from shadowing by one of its neighbors when 90% of the substrate is covered. Therefore, a NW length of the same order of magnitude of a few 100 nm is of importance for shadowing effects among the NWs.

C. Appendix C: Nomenclature

Throughout this thesis, materials are described by the use of chemical symbols. This appendix is intended to clarify their meaning as their use is handled differently by different authors.
Whenever doping of GaN is treated, a colon is used to indicate the doping species. An example would be GaN:Mg, to indicate that the NWs in question have been doped with Mg. This kind of symbol does not yield any information on the doping level. It only signifies that Mg was supplied during the growth. In particular, it does not signify that actual p-type doping (in the case of Mg doping) was achieved.
The second ambiguous notation is the symbol for the ternary alloy InGaN. In the chemical nomenclature, an alloy made up of these three elements N, Ga and In would be written as GaInN. Yet, in literature the use of InGaN is by far more common.
Strictly speaking, a ternary alloy such as InGaN written in this form is an alloy of exactly 50 atomic % In and 50 atomic % Ga for the group-III metals. For this reason (In,Ga)N is another symbol used in literature to avoid misinterpretations. This form of symbol addresses directly the fact that unknown or varying In concentrations are discussed. It does not tempt readers to fall back on the standard chemical interpretation of InGaN signifying $In_{50}Ga_{50}N$. Within this thesis, InGaN is meant to be an arbitrary amount of In alloying. It thus signifies the incorporation of In into the GaN matrix to an unknown extend, which needs to be quantified. If a given In concentration is known and addressed the use of $In_{22}Ga_{78}N$ (in the case of 22 atomic % In) is common and used in this thesis. These statements also hold true for the use of the symbol AlGaN.

Bibliography

[1] G. E. Moore. Cramming more components onto integrated circuits. *Electronics*, 38 (8):114, 1965.

[2] P. S. Peercy. The drive to miniaturization. *Nature*, 406(6799):1023, 2000.

[3] R. Waser. *Nanoelectronics and information technology*, volume 11. Wiley-VCH Weincheim, 2003.

[4] H. S. Nalwa and K. Ariga, editors. *Bottom-up Nanofabrication*. American Scientific Publishers, 2009.

[5] W. Lu and C. M. Lieber. Semiconductor nanowires. *J. Phys. D*, 39:R387, 2006.

[6] C. M. Lieber and Z. L. Wang. Functional nanowires. *MRS Bulletin*, 32(2):99–108, 2007. ISSN 0883-7694.

[7] E. Calleja, M. A. Sanchez-Garcia, F. J. Sanchez, F. Calle, F. B. Naranjo, E. Munoz, U. Jahn, and K. Ploog. Luminescence properties and defects in GaN nanocolumns grown by molecular beam epitaxy. *Phys. Rev. B*, 62(24):16826, 2000.

[8] K. A. Dick. A review of nanowire growth promoted by alloys and non-alloying elements with emphasis on au-assisted III-V nanowires. *Progr. Cryst. Gr. Char. Mater.*, 54(3-4):138 – 173, 2008. ISSN 0960-8974. doi: DOI:10.1016/j.pcrysgrow.2008.09.001. URL http://www.sciencedirect.com/science/article/B6TJB-4V2J6H7-1/2/706c6d51e20ca9368bf2854eca5c7b97.

[9] V. Schmidt, J. V. Wittemann, and U. Gösele. Growth, thermodynamics, and electrical properties of silicon nanowires. *Chem. Rev.*, 110(1):361–388, 2010. doi: 10.1021/cr900141g. URL http://pubs.acs.org/doi/abs/10.1021/cr900141g. PMID: 20070117.

[10] Y.W. Heo, D.P. Norton, L.C. Tien, Y. Kwon, B.S. Kang, F. Ren, S.J. Pearton, and J.R. LaRoche. ZnO nanowire growth and devices. *Mater. Sci. Eng. R Rep.*, 47(1-2):1 – 47, 2004. ISSN 0927-796X. doi: DOI:10.1016/j.mser.2004.09.001. URL http://www.sciencedirect.com/science/article/B6TXH-4F3NY29-1/2/ae607f593285554c52b5d0748a93d8a4.

[11] R. Agarwal. Heterointerfaces in semiconductor nanowires. *Small*, 4(11):1872–1893, 2008. ISSN 1613-6829. doi: 10.1002/smll.200800556. URL http://dx.doi.org/10.1002/smll.200800556.

[12] M. A. Sanchez-Garcia, E. Calleja, E. Monroy, F. J. Sanchez, F. Calle, E. Munoz, and R. Beresford. The effect of the III/V ratio and substrate temperature on the morphology and properties of GaN- and AlN-layers grown by molecular beam epitaxy on Si(111). *J. Cryst. Growth*, 183(1-2):23–30, 1998. ISSN 0022-0248.

[13] E. F. Schubert. *Light-Emitting Diodes*. Cambridge University Press, New York, 2006.

[14] E. Ertekin, P. A. Greaney, D. C. Chrzan, and T. D. Sands. Equilibrium limits of coherency in strained nanowire heterostructures. *J. Appl. Phys.*, 97(11):114325, 2005. doi: 10.1063/1.1903106. URL http://link.aip.org/link/?JAP/97/114325/1.

[15] F. Glas. Critical dimensions for the plastic relaxation of strained axial heterostructures in free-standing nanowires. *Phys. Rev. B*, 74(12):121302, 2006. doi: 10.1103/PhysRevB.74.121302.

[16] N. Thillosen, K. Sebald, H. Hardtdegen, R. Meijers, R. Calarco, S. Montanari, N. Kaluza, J. Gutowski, and H. Lüth. The state of strain in single GaN nanocolumns as derived from micro-photoluminescence measurements. *Nano Lett.*, 6(4):704–708, 2006.

[17] S. Harui, H. Tamiya, T. Akagi, H. Miyake, K. Hiramatsu, T. Araki, and Y. Nanishi. Transmission electron microscopy characterization of position-controlled InN nanocolumns. *Jpn. J. Appl. Phys.*, 47(7):5330–5332, 2008. doi: 10.1143/JJAP.47.5330. URL http://jjap.jsap.jp/link?JJAP/47/5330/.

[18] R. Meijers, T. Richter, R. Calarco, T. Stoica, H. P. Bochem, M. Marso, and H. Lüth. GaN-nanowhiskers: MBE-growth conditions and optical properties. *J. Cryst. Growth*, 289(1):381–386, 2006. ISSN 0022-0248. doi: 10.1016/j.jcrysgro.2005.11.117.

[19] T. Stoica, E. Sutter, R. J. Meijers, R. K. Debnath, R. Calarco, H. Lüth, and D. Grützmacher. Interface and wetting layer effect on the catalyst-free nucleation and growth of GaN nanowires. *Small*, 4(6):751–754, 2008. ISSN 1613-6829. doi: 10.1002/smll.200700936. URL http://dx.doi.org/10.1002/smll.200700936.

[20] M.-A. Tsai, P. Yu, C. L. Chao, C. H. Chiu, H. C. Kuo, S. H. Lin, J. J. Huang, T. C. Lu, and S. C. Wang. Efficiency enhancement and beam shaping of GaN-InGaN vertical-injection light-emitting diodes via high-aspect-ratio nanorod arrays. *IEEE Phot. Tech. Let.*, 21(4):257 –259, 2009. ISSN 1041-1135. doi: 10.1109/LPT.2008.2010556.

[21] C. Pfüller. *Optical properties of single semiconductor nanowires and nanowire ensembles*. PhD thesis, Humboldt-Universität zu Berlin, 2011.

[22] E. F. Schubert and J. K. Kim. Solid-state light sources getting smart. *Science*, 308(5726):1274–1278, 2005. doi: 10.1126/science.1108712. URL http://www.sciencemag.org/content/308/5726/1274.abstract.

[23] J. Wu, W. Walukiewicz, K. M. Yu, W. Shan, J. W. Ager III, E. E. Haller, H. Lu, W. J. Schaff, W. K. Metzger, and S. Kurtz. Superior radiation resistance of $In_{1-x}Ga_xN$ alloys: Full-solar-spectrum photovoltaic material system. *J. Appl. Phys.*, 94(10):6477–6482, 2003. doi: 10.1063/1.1618353. URL http://link.aip.org/link/?JAP/94/6477/1.

[24] P. Kung and M. Razeghi. III-Nitride wide bandgap semiconductors: a survey of the current status and future trends of the material and device technology. *Opto-Elec. Rev.*, 8(3):201–239, 2000. ISSN 1230-3402.

[25] S. Nakamura, S. Pearton, and F. Gerhard. *The Blue Laser Diode*. Springer-Verlag, 2000.

[26] T. Kuykendall, P. Ulrich, S. Aloni, and P. Yang. Complete composition tunability of InGaN nanowires using a combinatorial approach. *Nature Mater.*, 6(12):951–956, 2007. ISSN 1476-1122. doi: 10.1038/nmat2037.

[27] C. J. Humphreys. Solid state lighting. *Lightwave Technology, Journal of*, 26(10):1363 –1364, 2008. ISSN 0733-8724. doi: 10.1109/JLT.2008.927128.

[28] H. Morkoc. *Handbook of Nitride Semiconductors and Devices: Electronic and optical processes in nitrides*. Vch Verlagsgesellschaft Mbh, 2008.

[29] A. Zoroddu, F. Bernardini, P. Ruggerone, and V. Fiorentini. First-principles prediction of structure, energetics, formation enthalpy, elastic constants, polarization, and piezoelectric constants of AlN, GaN, and InN: Comparison of local and gradient-corrected density-functional theory. *Phys. Rev. B*, 64(4):045208, 2001.

[30] J. Wu, W. Walukiewicz, K. M. Yu, J. W. Ager, E. E. Haller, H. Lu, and W. J. Schaff. Small band gap bowing in $In_{1-x}Ga_xN$ alloys. *Appl. Phys. Lett.*, 80(25):4741–4743, 2002.

[31] F. Bernardini, V. Fiorentini, and D. Vanderbilt. Spontaneous polarization and piezoelectric constants of III-V nitrides. *Phys. Rev. B*, 56(16):10024–10027, 1997.

[32] G. Burns. *Solid State Physics*. Academic Press, New York, 1985.

[33] R. D. King-Smith and D. Vanderbilt. Theory of polarization of crystalline solids. *Phys. Rev. B*, 47(3):1651, 1993.

[34] R. Resta. Macroscopic polarization in crystalline dielectrics: the geometric phase approach. *Rev. Mod. Phys.*, 66(3):899, 1994.

[35] F. Bernardini and V. Fiorentini. Nonlinear behavior of spontaneous and piezoelectric polarization in III-V nitride alloys. *Phys. Status Solidi A*, 190(1):65–73, 2002.

[36] F. Bernardini and V. Fiorentini. Nonlinear macroscopic polarization in III-V nitride alloys. *Phys. Rev. B*, 64(8):085207, 2001.

[37] F. Bernardini and V. Fiorentini. Erratum [Phys. Rev. B 64, 085207 (2001)]: Nonlinear macroscopic polarization in III-V nitride alloys. *Phys. Rev. B*, 65(12):129903, 2002.

[38] C. Wetzel, T. Takeuchi, H. Amano, and I. Akasaki. Piezoelectric Stark-like ladder in GaN/GaInN/GaN heterostructures. *Jpn. J. Appl. Phys.*, 38(2-2B):L163–L165, 1999. doi: 10.1143/JJAP.38.L163. URL `http://jjap.jsap.jp/link?JJAP/38/L163/`.

[39] O. Ambacher, J. Majewski, C. Miskys, A. Link, M. Hermann, M. Eickhoff, M. Stutzmann, F. Bernardini, V. Fiorentini, V. Tilak, et al. Pyroelectric properties of Al (In) GaN/GaN hetero-and quantum well structures. *J. Phys.: Condens. Matter*, 14:3399, 2002.

[40] J. Lähnemann, O. Brandt, C. Pfüller, T. Flissikowski, U. Jahn, E. Luna, M. Hanke, M. Knelangen, A. Trampert, and H. T. Grahn. Coexistence of quantum-confined Stark effect and localized states in an (In,Ga)N/GaN nanowire heterostructure. *Phys. Rev. B*, 84(15):155303, 2011.

[41] T. Mattila and R. M. Nieminen. Point-defect complexes and broadband luminescence in GaN and AlN. *Phys. Rev. B*, 55(15):9571, 1997.

[42] J. Neugebauer and C. G. van de Walle. Gallium vacancies and the yellow luminescence in GaN. *Appl. Phys. Lett.*, 69:503, 1996.

[43] W. J. Moore, J. A. Freitas Jr., S. K. Lee, S. S. Park, and J. Y. Han. Magneto-optical studies of free-standing hydride-vapor-phase epitaxial GaN. *Phys. Rev. B*, 65(8): 081201, 2002.

[44] J. I. Pankove and J. A. Hutchby. Photoluminescence of ion-implanted GaN. *J. Appl. Phys.*, 47(12):5387–5390, 1976.

[45] H. Wang and A. B. Chen. Calculations of acceptor ionization energies in GaN. *Phys. Rev. B*, 63(12):125212, 2001.

[46] F. Mireles and S. E. Ulloa. Acceptor binding energies in GaN and AlN. *Phys. Rev. B*, 58(7):3879, 1998.

[47] H. Obloh, K. H. Bachem, U. Kaufmann, M. Kunzer, M. Maier, A. Ramakrishnan, and P. Schlotter. Self-compensation in Mg doped p-type GaN grown by MOCVD. *J. Cryst. Growth*, 195(1-4):270–273, 1998.

[48] M. A. Reshchikov and H. Morkoç. Luminescence properties of defects in GaN. *J. Appl. Phys.*, 97(6):061301, 2005. ISSN 00218979. doi: DOI:10.1063/1.1868059. URL `http://dx.doi.org/doi/10.1063/1.1868059`.

[49] J. Lähnemann, O. Brandt, U. Jahn, C. Pfüller, C. Roder, P. Dogan, F. Grosse, A. Trampert, L. Geelhaar, A. Belabbes, and F. Bechstedt. Direct experimental determination of the spontaneous polarization of GaN. *Phys. Rev. Lett.*, submitted, 2011.

[50] V. Consonni, M. Knelangen, U. Jahn, A. Trampert, L. Geelhaar, and H. Riechert. Effects of nanowire coalescence on their structural and optical properties on a local scale. *Appl. Phys. Lett.*, 95(24), 2009. ISSN 0003-6951. doi: 10.1063/1.3275793.

[51] H. Lüth. *Solid surfaces, interfaces and thin films*. Springer Verlag, 2010.

[52] S. M. Sze and K. K. Ng. *Physics of semiconductor devices*. Wiley-Blackwell, 2007.

[53] I. K. Park and S. J. Park. Green gap spectral range light-emitting diodes with self-assembled InGaN quantum dots formed by enhanced phase separation. *Appl. Phys. Expr.*, 4(4):042102–042102, 2011.

[54] E. Kioupakis, P. Rinke, K. T. Delaney, and C. G. Van de Walle. Indirect Auger recombination as a cause of efficiency droop in nitride light-emitting diodes. *Appl. Phys. Lett.*, 98:161107, 2011.

[55] A. Laubsch, M. Sabathil, W. Bergbauer, M. Strassburg, H. Lugauer, M. Peter, S. Lutgen, N. Linder, K. Streubel, J. Hader, J. V. Moloney, B. Pasenow, and S. W. Koch. On the origin of IQE-'droop 'in InGaN LEDs. *Phys. Status Solidi C*, 6(S2):S913–S916, 2009.

[56] N. I. Bochkareva, V. V. Voronenkov, R. I. Gorbunov, A. S. Zubrilov, Y. S. Lelikov, P. E. Latyshev, Y. T. Rebane, A. I. Tsyuk, and Y. G. Shreter. Defect-related tunneling mechanism of efficiency droop in III-nitride light-emitting diodes. *Appl. Phys. Lett.*, 96:133502, 2010.

[57] S. H. Yen, M. C. Tsai, M. L. Tsai, Y. J. Shen, T. C. Hsu, and Y. K. Kuo. Effect of n-type AlGaN layer on carrier transportation and efficiency droop of blue InGaN light-emitting diodes. *IEEE Phot. Tech. Lett.*, 21(14):975–977, 2009.

[58] Y. K. Kuo, M. C. Tsai, S. H. Yen, T. C. Hsu, and Y. J. Shen. Effect of p-type last barrier on efficiency droop of blue InGaN light-emitting diodes. *IEEE J. Quantum Electron.*, 46(8):1214–1220, 2010.

[59] Y. J. Lee, C. H. Chen, and C. J. Lee. Reduction in the efficiency-droop effect of InGaN green light-emitting diodes using gradual quantum wells. *IEEE Phot. Tech. Lett.*, 22(20):1506–1508, 2010.

[60] I.-K. Park, M.-K. Kwon, J.-O. Kim, S.-B. Seo, J.-Y. Kim, J.-H. Lim, S.-J. Park, and Y.-S. Kim. Green light-emitting diodes with self-assembled In-rich InGaN quantum dots. *Appl. Phys. Lett.*, 91(13):133105, 2007. doi: 10.1063/1.2790783. URL `http://link.aip.org/link/?APL/91/133105/1`.

[61] G. B. Stringfellow. Microstructures produced during the epitaxial growth of InGaN alloys. *J. Cryst. Growth*, 312(6):735–749, 2010.

[62] W. Guo, M. Zhang, A. Banerjee, and P. Bhattacharya. Catalyst-Free InGaN/GaN nanowire light emitting diodes grown on (001) silicon by molecular beam epitaxy. *Nano Lett.*, 10(9):3355–3359, 2010. doi: 10.1021/nl101027x. URL `http://pubs.acs.org/doi/abs/10.1021/nl101027x`.

[63] H. Sekiguchi, K. Kishino, and A. Kikuchi. Emission color control from blue to red with nanocolumn diameter of InGaN/GaN nanocolumn arrays grown on same substrate. *Appl. Phys. Lett.*, 96(23):231104, 2010.

[64] A.-L. Bavencove, G. Tourbot, E. Pougeoise, J. Garcia, P. Gilet, F. Levy, B. André, G. Feuillet, B. Gayral, B. Daudin, and L. S. Dang. GaN-based nanowires: From nanometric-scale characterization to light emitting diodes. *Phys. Status Solidi A*, 207(6):1425–1427, 2010. ISSN 1862-6319. doi: 10.1002/pssa.200983603. URL `http://dx.doi.org/10.1002/pssa.200983603`.

[65] R. Armitage and K. Tsubaki. Multicolour luminescence from InGaN quantum wells grown over GaN nanowire arrays by molecular-beam epitaxy. *Nanotechnology*, 21 (19):195202, 2010. URL `http://stacks.iop.org/0957-4484/21/i=19/a=195202`.

[66] A. Waag, X. Wang, S. Fündling, J. Ledig, M. Erenburg, R. Neumann, M. Al Suleiman, S. Merzsch, J. Wei, S. Li, et al. The nanorod approach: GaN NanoLEDs for solid state lighting. *Phys. Status Solidi C*, 8(7-8):2296–2301, 2011.

[67] H. Riechert, O. Brandt, C. Cheze, V. Consonni, M. Knelangen, J. Lähnemann, F. Limbach, C. Pfüller, A. Trampert, M. Wölz, et al. Nitride nanowire structures for LED applications. In *Proceedings of SPIE*, volume 7954, page 79540S, 2011.

[68] T. Xu, A. Y. Nikiforov, R. France, C. Thomidis, A. Williams, and T. D. Moustakas. Blue-green-red LEDs based on InGaN quantum dots grown by plasma-assisted molecular beam epitaxy. *Phys. Status Solidi A*, 204(6):2098–2102, 2007. ISSN 1862-6319. doi: 10.1002/pssa.200674834. URL `http://dx.doi.org/10.1002/pssa.200674834`.

[69] H. J. Round. A note on carborundum. *Electrical World*, 19:309, 1907.

[70] O. V. Lossev. Luminous carborundum detector and detection effect and oscillations with crystals. *Phil. Magazine*, 6(39, 7TH SERIES):1024–1044, 1928. ISSN 1478-6443.

[71] R. M. Potter, J. M. Blank, and A. Addamiano. Silicon carbide light emitting diodes. *J. Appl. Phys.*, 40(5):2253–2257, 1969. ISSN 00218979. doi: DOI:10.1063/1.1657967. URL `http://dx.doi.org/10.1063/1.1657967`.

[72] H. Welker. über neue halbleitende Verbindungen. *Z. für Nat. Sec. A - A J. of Phys. Sci.*, 7(11):744–749, 1952. ISSN 0932-0784.

[73] H. Welker. über neue halbleitende Verbindungen-II. *Z. für Nat. Sec. A - A J. of Phys. Sci.*, 8(4):248–251, 1953. ISSN 0932-0784.

[74] R. N. Hall, G. E. Fenner, J. D. Kingsley, T. J. Soltys, and R. O. Carlson. Coherent light emission from GaAs junctions. *Phys. Rev. Lett.*, 9:366–368, 1962. doi: 10.1103/PhysRevLett.9.366. URL `http://link.aps.org/doi/10.1103/PhysRevLett.9.366`.

[75] M. I. Nathan, W. P. Dumke, G. Burns, F. H. Dill, and G. Lasher. Stimulated emission of radiation from GaAs p-n junctions. *Appl. Phys. Lett.*, 1(3):62–64, 1962. ISSN 00036951. doi: DOI:10.1063/1.1777371. URL `http://dx.doi.org/10.1063/1.1777371`.

[76] I. J. Pankove and M. J. Massoulie. Injection luminescence from GaAs. *Bull. Am. Phys. Soc.*, 7:88, 1962.

[77] I. J. Pankove and J. E. Berkeyheiser. A light source modulated at microwave frequencies. *Proc. IRE*, 50:1976, 1962.

[78] T. M. Quist, R. H. Rediker, R. J. Keyes, W. E. Krag, B. Lax, A. L. McWhorter, and H. J. Zeigler. Semiconductor maser of GaAs. *Appl. Phys. Lett.*, 1(4):91–92, 1962. ISSN 00036951. doi: DOI:10.1063/1.1753710. URL `http://dx.doi.org/10.1063/1.1753710`.

[79] N. Holonyak and S. F. Bevacqua. Coherent (visible) light emission from $Ga(As_{1-x}P_x)$ junctions. *Appl. Phys. Lett.*, 1(4):82–83, 1962. ISSN 00036951. doi: DOI:10.1063/1.1753706. URL `http://dx.doi.org/10.1063/1.1753706`.

[80] G. Rostky. LEDs cast monsanto in unfamiliar role. *Elec. Eng. Times*, pages 24–25, 1997.

[81] J. I. Pankove, E. A. Miller, D. Richman, and J. E. Berkeyheiser. Electroluminescence in GaN. *J. Lumin.*, 4(1):63–66, 1971.

[82] H. P. Maruska, D. A. Stevenson, and J. I. Pankove. Violet luminescence of Mg-doped GaN. *Appl. Phys. Lett.*, 22(6):303–305, 1973.

[83] H. Amano, M. Kito, K. Hiramatsu, and I. Akasaki. P-type conduction in Mg-doped GaN treated with low-energy electron beam irradiation (LEEBI). *Jpn. J. Appl. Phys.*, 28:L2112–L2114, 1989.

[84] S. Nakamura, M. Senoh, N. Iwasa, and S. Nagahama. High-brightness InGaN blue, green and yellow light-emitting diodes with quantum well structures. *Jpn. J. Appl. Phys.*, 34:797–797, 1995.

[85] S. Nakamura, M. Senoh, S. Nagahama, N. Iwasa, T. Yamada, T. Matsushita, Y. Sugimoto, and H. Kiyoku. Room-temperature continuous-wave operation of InGaN multi-quantum-well structure laser diodes. *Appl. Phys. Lett.*, 69:4056, 1996.

[86] N. E. J. Hunt, E. F. Schubert, D. L. Sivco, A. Y. Cho, and G. J. Zydzik. Power and efficiency limits in single-mirror light emitting diodes with enhanced intensity. *Electron. Lett.*, 28(23):2169–2171, 1992.

[87] Cree Inc. LED arrays arrive, http://www.cree.com/products/pdf/led arrays.pdf, 12 2011. URL `http://www.cree.com/products/pdf/ledarrays.pdf`.

[88] C. Lieber. The incredible shrinking circuit. *Spe. Ed. of Sci. Am.*, 17(3):64–71, 2007.

[89] X. Duan, Y. Huang, Y. Cui, J. Wang, and C. M. Lieber. Indium phosphide nanowires as building blocks for nanoscale electronic and optoelectronic devices. *Nature*, 409 (6816):66–69, 2001.

[90] C. Fasth, A. Fuhrer, M. T. Bjork, and L. Samuelson. Tunable double quantum dots in InAs nanowires defined by local gate electrodes. *Nano Lett.*, 5(7):1487–1490, 2005.

[91] Y.-R. Wu, C. Chiu, C.-Y. Chang, P. Yu, and H.-C. Kuo. Size-dependent strain relaxation and optical characteristics of InGaN/GaN nanorod LEDs. *IEEE J. Sel. Topics in Quantum Electron.*, 15(4):1226 –1233, 2009. ISSN 1077-260X. doi: 10.1109/JSTQE.2009.2015583.

[92] T. Stoica, A. Haab, D. Griesche, M. Mikulics, F. Limbach, T. Schumann, T. Gotschke, E. Sutter, R. Calarco, H. Hardtdegen, and D. Grützmacher. Photoluminescence and raman scattering studies of gan nanowires obtained by top-down and bottom-up approaches. In *MRS Proc. 1408, MRSF11-1408-BB20-14*, 2012.

[93] R. S. Wagner and W. C. Ellis. Vapor - liquid - solid mechanism of single crystal growth. *Appl. Phys. Lett.*, 4:89, 1964.

[94] H. J. Joyce, Q. Gao, H. Hoe Tan, C. Jagadish, Y. Kim, J. Zou, L. M. Smith, H. E. Jackson, J. M. Yarrison-Rice, P. Parkinson, et al. III-V semiconductor nanowires for optoelectronic device applications. *Prog. in Quantum Electron.*, 2011.

[95] S. Breuer. *Molecular Beam Epitaxy of GaAs nanowires and their suitability for optoelectronic applications*. PhD thesis, Humboldt-Universität zu Berlin, 2011.

[96] S. Nadj-Perge, S. M. Frolov, E. Bakkers, and L. P. Kouwenhoven. Spin-orbit qubit in a semiconductor nanowire. *Nature*, 468(7327):1084–1087, 2010.

[97] S. De Franceschi, J. A. van Dam, E. Bakkers, L. F. Feiner, L. Gurevich, and L. P. Kouwenhoven. Single-electron tunneling in InP nanowires. *Appl. Phys. Lett.*, 83: 344, 2003.

[98] M. T. Björk, C. Thelander, A. E. Hansen, L. E. Jensen, M. W. Larsson, L. R. Wallenberg, and L. Samuelson. Few-electron quantum dots in nanowires. *Nano Lett.*, 4: 1621–1625, 2004.

[99] Y. Huang and et al. Lieber, C. M. Logic gates and computation from assembled nanowire building blocks. *Science*, 294(5545):1313–1317, 2001.

[100] F. Werner, F. Limbach, M. Carsten, C. Denker, J. Malindretos, and A. Rizzi. Electrical conductivity of InN nanowires and the influence of the native indium oxide formed at their surface. *Nano letters*, 9(4):1567–1571, 2009.

[101] Y. Huang, X. Duan, Y. Cui, and C. M. Lieber. Gallium nitride nanowire nanodevices. *Nano Lett.*, 1:6, 2001.

[102] S. J. Pearton, B. S. Kang, B. P. Gila, D. P. Norton, O. Kryliouk, F. Ren, Y. W. Heo, C. Y. Chang, G. C. Chi, W. M. Wang, et al. GaN, ZnO and InN nanowires and devices. *J. of Nanosci. and Nanotech.*, 8(1):99–110, 2008.

[103] A. Koeck, R. Hainberger, R. Heer, M. Kast, T. Maier, and C. Stepper. Electrical and optical nanosensors. In *Nanotech 2006 Conference and Expo*, volume 3, pages 66 – 69, 2006.

[104] Z. L. Wang. *Nanowires and Nanobelts: Materials, Properties, and Devices*. Kluwer Academic Publishers, 2003.

[105] T. Voss, G. T. Svacha, E. Mazur, S. Müller, C. Ronning, D. Konjhodzic, and F. Marlow. High-order waveguide modes in ZnO nanowires. *Nano Lett.*, 7(12):3675–3680, 2007.

[106] C. Grillet, C. Monat, C. L. Smith, B.J. Eggleton, D. J. Moss, S. Frédérick, D. Dalacu, P. J. Poole, J. Lapointe, G. Aers, et al. Nanowire coupling to photonic crystal nanocavities for single photon sources. *Opt. Express*, 15(3):1267–1276, 2007.

[107] J. Johansson and K. A. Dick. Recent advances in semiconductor nanowire heterostructures. *CrystEngComm*, 2011.

[108] W. Bergbauer, M. Strassburg, C. Kölper, N. Linder, C. Roder, J. Lahnemann, A. Trampert, S. Fündling, S. F. Li, H.H. Wehmann, et al. N-face GaN nanorods: Continuous-flux MOVPE growth and morphological properties. *J. Cryst. Growth*, 315(1):164–167, 2011.

[109] M. A. Herman and H. Sitter. Molecular beam epitaxy: Fundamentals and current status, vol. 7. *Springer Series in Materials Science (Springer, Berlin 1996) p*, 38:234, 1996.

[110] E. H. C. Parker. *The Technology and physics of molecular beam epitaxy*. Plenum Press, 1985.

[111] A. Ichimiya and P. I. Cohen. *Reflection high-energy electron diffraction*. Cambridge Univ Pr, 2004.

[112] R. J. Meijers. *Growth and Characterisation of Group-III Nitride-based Nanowires for Devices*. PhD thesis, Rheinisch-Westfälische Technische Hochschule Aachen, 2007.

[113] T. Gotschke. *Untersuchungen zum geordneten Wachstum von III-Nitrid Nanodrähten*. PhD thesis, Humboldt-Universität zu Berlin, 2012.

[114] G. Koblmüller, S. Fernández-Garrido, E. Calleja, and J. S. Speck. In situ investigation of growth modes during plasma-assisted molecular beam epitaxy of (0001) GaN. *Appl. Phys. Lett.*, 91:161904, 2007.

[115] S. Fernández-Garrido, G. Koblmüller, E. Calleja, and J. S. Speck. In situ GaN decomposition analysis by quadrupole mass spectrometry and reflection high-energy electron diffraction. *J. Appl. Phys.*, 104(3):033541, 2008. ISSN 00218979. doi: DOI: 10.1063/1.2968442. URL http://dx.doi.org/doi/10.1063/1.2968442.

[116] C. Cheze, L. Geelhaar, A. Trampert, and H. Riechert. In situ investigation of self-induced GaN nanowire nucleation on Si. *Appl. Phys. Lett.*, 97(4):043101, 2010. doi: 10.1063/1.3464956. URL http://link.aip.org/link/?APL/97/043101/1.

[117] C. Cheze. *Investigation and comparison of GaN nanowire nucleation and growth by the catalyst-assisted and self-induced approaches*. PhD thesis, Humboldt-Universität zu Berlin, 2010.

[118] F. Limbach, R. Caterino, T. Gotschke, T. Stoica, R. Calarco, L. Geelhaar, and H. Riechert. The influence of Mg doping on the nucleation of self-induced GaN nanowires. *AIP Adv.*, 2:012157, 2012.

[119] L. I. Maissel, R. Glang, and P. P. Budenstein. Handbook of thin film technology. *Journal of The Electrochemical Society*, 118:114C, 1971.

[120] B. Lewis and J. C. Anderson. *Nucleation and growth of thin films*. Academic Press New York, 1978.

[121] M. Volmer and A. Weber. Keimbildung in übersattigten Gebilden. *Z. Phys. Chem.*, 119:277, 1925.

[122] R. Becker and W. Döring. Kinetische Behandlung der Keimbildung in übersättigten Dämpfen. *Ann. Phys.*, 24:719, 1935.

[123] V. Consonni, A. Trampert, L. Geelhaar, and H. Riechert. Origin of the incubation time during the nucleation of self-induced GaN nanowires grown by molecular beam epitaxy. *Appl. Phys. Lett.*, 99:033102, 2011.

[124] S. D. Carnevale, J. Yang, P. J. Phillips, M. J. Mills, and R. C. Myers. Three-dimensional GaN/AIN nanowire heterostructures by separating nucleation and growth processes. *Nano Lett.*, 11(2):866–871, 2011. ISSN 1530-6984. doi: 10.1021/nl104265u.

[125] O. Landre, C. Bougerol, H. Renevier, and B. Daudin. Nucleation mechanism of GaN nanowires grown on (111) Si by molecular beam epitaxy. *Nanotechnology*, 20 (41):415602, 2009. URL http://stacks.iop.org/0957-4484/20/i=41/a=415602.

[126] R. Calarco, R. J. Meijers, R. K. Debnath, T. Stoica, E. Sutter, and H. Lüth. Nucleation and growth of GaN nanowires on Si(111) performed by molecular beam epitaxy. *Nano Lett.*, 7(8):2248–2251, 2007. doi: 10.1021/nl0707398. URL `http://pubs.acs.org/doi/abs/10.1021/nl0707398`.

[127] V. Consonni, M. Knelangen, A. Trampert, L. Geelhaar, and H. Riechert. Nucleation and coalescence effects on the density of self-induced GaN nanowires grown by molecular beam epitaxy. *Appl. Phys. Lett.*, 98(7):071913, 2011. doi: 10.1063/1.3555450. URL `http://link.aip.org/link/?APL/98/071913/1`.

[128] R. Mata, K. Hestroffer, J. Budagosky, A. Cros, C. Bougerol, H. Renevier, and B. Daudin. Nucleation of GaN nanowires grown by plasma-assisted molecular beam epitaxy: The effect of temperature. *J. Cryst. Growth*, 334(1):177 – 180, 2011. ISSN 0022-0248. doi: 10.1016/j.jcrysgro.2011.08.015. URL `http://www.sciencedirect.com/science/article/pii/S0022024811006877`.

[129] V. Consonni, M. Hanke, M. Knelangen, L. Geelhaar, A. Trampert, and H. Riechert. Nucleation mechanisms of self-induced GaN nanowires grown on an amorphous interlayer. *Phys. Rev. B*, 83(3), 2011. ISSN 1098-0121. doi: 10.1103/PhysRevB.83.035310.

[130] V. Consonni, M. Knelangen, L. Geelhaar, A. Trampert, and H. Riechert. Nucleation mechanisms of epitaxial GaN nanowires: Origin of their self-induced formation and initial radius. *Phys. Rev. B*, 81(8), 2010. ISSN 1098-0121. doi: 10.1103/PhysRevB.81.085310.

[131] A. R. Smith, R. M. Feenstra, D. W. Greve, M. S. Shin, M. Skowronski, J. Neugebauer, and J. E. Northrup. Reconstructions of GaN(0001) and (0001) surfaces: Ga-rich metallic structures. *J. Vac. Sci. Technol. B*, 16:2242, 1998.

[132] J. E. Northrup, J. Neugebauer, R. M. Feenstra, and A. R. Smith. Structure of GaN(0001): The laterally contracted Ga bilayer model. *Phys. Rev. B*, 61(15):9932, 2000.

[133] G. Mula, C. Adelmann, S. Moehl, J. Oullier, and B. Daudin. Surfactant effect of gallium during molecular-beam epitaxy of GaN on AlN(0001). *Phys. Rev. B*, 64(19):195406, 2001.

[134] C. Adelmann, J. Brault, G. Mula, B. Daudin, L. Lymperakis, and J. Neugebauer. Gallium adsorption on (0001) GaN surfaces. *Phys. Rev. B*, 67(16):165419, 2003.

[135] K. A. Bertness, A. Roshko, L. M. Mansfield, T. E. Harvey, and N. A. Sanford. Mechanism for spontaneous growth of GaN nanowires with molecular beam epitaxy. *J. Cryst. Growth*, 310(13):3154–3158, 2008.

[136] J. Ristic, E. Calleja, S. Fernandez-Garrido, L. Cerutti, A. Trampert, U. Jahn, and K. H. Ploog. On the mechanisms of spontaneous growth of III-nitride nanocolumns by plasma-assisted molecular beam epitaxy. *J. Cryst. Growth*, 310(18):4035–4045, 2008.

[137] M. Tchernycheva, C. Sartel, G. Cirlin, L. Travers, G. Patriarche, J. C. Harmand, L. S. Dang, J. Renard, B. Gayral, L. Nevou, et al. Growth of GaN free-standing nanowires by plasma-assisted molecular beam epitaxy: structural and optical characterization. *Nanotechnology*, 18:385306, 2007.

[138] R. Songmuang, O. Landre, and B. Daudin. From nucleation to growth of catalyst-free GaN nanowires on thin AlN buffer layer. *Appl. Phys. Lett.*, 91(25):251902, 2007. ISSN 0003-6951. doi: 10.1063/1.2817941.

[139] R. K. Debnath, R. Meijers, T. Richter, T. Stoica, R. Calarco, and H. Lüth. Mechanism of molecular beam epitaxy growth of GaN nanowires on Si(111). *Appl. Phys. Lett.*, 90:123117, 2007.

[140] K. A. Bertness, A. Roshko, N. A. Sanford, J. M. Barker, and A. Davydov. Spontaneously grown GaN and AlGaN nanowires. *J. Cryst. Growth*, 287(2):522–527, 2006. ISSN 0022-0248. doi: 10.1016/j.jcrysgro.2005.11.079.

[141] L. Lymperakis and J. Neugebauer. Large anisotropic adatom kinetics on nonpolar GaN surfaces: Consequences for surface morphologies and nanowire growth. *Phys. Rev. B*, 79(24):241308, 2009. doi: 10.1103/PhysRevB.79.241308.

[142] L. Lymperakis, H. Abu-Farsakh, O. Marquardt, T. Hickel, and J. Neugebauer. Theoretical modeling of growth processes, extended defects, and electronic properties of III-nitride semiconductor nanostructures. *Phys. Status Solidi B*, 248(8):1837 – 1852, 2011.

[143] B. Jenichen, O. Brandt, C. Pfüller, P. Dogan, M. Knelangen, and A. Trampert. Macro- and micro-strain in GaN nanowires on Si (111). *Nanotechnology*, 22:295714, 2011.

[144] P. Dogan, O. Brandt, C. Pfuller, A.K. Bluhm, L. Geelhaar, and H. Riechert. GaN nanowire templates for the pendeoepitaxial coalescence overgrowth on Si (111) by molecular beam epitaxy. *J. Cryst. Growth*, 22(29):295714, 2011.

[145] C. S. Gallinat, G. Koblmüller, J. S. Brown, and J. S. Speck. A growth diagram for plasma-assisted molecular beam epitaxy of In-face InN. *J. Appl. Phys.*, 102:064907, 2007.

[146] C. Denker, J. Malindretos, F. Werner, F. Limbach, H. Schuhmann, T. Niermann, M. Seibt, and A. Rizzi. Self-organized growth of InN-nanocolumns on p-Si(111) by MBE. *Phys. Status Solidi C*, 5(6):1706–1708, 2008.

[147] R. Averbeck and H. Riechert. Quantitative model for the MBE-growth of ternary nitrides. *Phys. Status Solidi A*, 176(1):301–305, 1999.

[148] E. Galopin, L. Largeau, G. Patriarche, L. Travers, F. Glas, and J. C. Harmand. Morphology of self-catalyzed GaN nanowires and chronology of their formation by molecular beam epitaxy. *Nanotechnology*, 22:245606, 2011.

[149] C. T. Foxon, S. V. Novikov, J. L. Hall, R. P. Campion, D. Cherns, I. Griffiths, and S. Khongphetsak. A complementary geometric model for the growth of GaN nanocolumns prepared by plasma-assisted molecular beam epitaxy. *J. Cryst. Growth*, 311(13):3423–3427, 2009.

[150] F. Limbach, E. O. Schäfer-Nolte, R. Caterino, T. Gotschke, T. Stoica, E. Sutter, and R. Calarco. Morphology and optical properties of Mg doped GaN nanowires in dependence of growth temperature. *J. Optoel. Adv. Mat.*, 12(6):1433–1437, 2010. ISSN 1454-4164.

[151] L. H. Robins, K. A. Bertness, J. M. Barker, N. A. Sanford, and J. B. Schlager. Optical and structural study of GaN nanowires grown by catalyst-free molecular beam epitaxy. II. Sub-band-gap luminescence and electron irradiation effects. *J. Appl. Phys.*, 101:113506, 2007.

[152] J. Renard, R. Songmuang, C. Bougerol, B. Daudin, and B. Gayral. Exciton and biexciton luminescence from single GaN/AlN quantum dots in nanowires. *Nano Lett.*, 8(7):2092–2096, 2008.

[153] K. Goodman, V. Protasenko, Vladimir, J. Verma, T. Kosel, G. Xing, and D. Jena. Molecular beam epitaxial growth of gallium nitride nanowires on atomic layer deposited aluminum oxide. *J. Cryst. Growth*, 334(1):113 – 117, 2011. ISSN 0022-0248. doi: 10.1016/j.jcrysgro.2011.08.032. URL `http://www.sciencedirect.com/science/article/pii/S0022024811007159`.

[154] M. Yoshizawa, A. Kikuchi, M. Mori, N. Fujita, and K. Kishino. Growth of self-organized GaN nanostructures on Al_2O_3(0001) by RF-radical source molecular beam epitaxy. *Jpn. J. Appl. Phys. Part 2 Let.*, 36(4B):L459–L462, 1997.

[155] T. Schumann, T. Gotschke, F. Limbach, T. Stoica, and R. Calarco. Cathodoluminescence spectroscopy on selectively grown GaN nanowires. In Jen-Inn Chyi, Yasushi Nanishi, Hadis Morkoç, Joachim Piprek, and Euijoon Yoon, editors, *Proceedings of SPIE Photonics West 2011*, volume 7939, page 793903. SPIE, 2011. doi: 10.1117/12.878836. URL `http://link.aip.org/link/?PSI/7939/793903/1`.

[156] T. Gotschke, T. Schumann, F. Limbach, T. Stoica, and R. Calarco. Influence of the adatom diffusion on selective growth of GaN nanowire regular arrays. *Appl. Phys. Lett.*, 98:103102, 2011.

[157] T. Schumann, T. Gotschke, F. Limbach, T. Stoica, and R. Calarco. Selective-area catalyst-free mbe growth of gan nanowires using a patterned oxide layer. *Nanotechnology*, 22:095603, 2011.

[158] K. Kishino, H. Sekiguchi, and A. Kikuchi. Improved Ti-mask selective-area growth (SAG) by rf-plasma-assisted molecular beam epitaxy demonstrating extremely uniform GaN nanocolumn arrays. *J. Cryst. Growth*, 311(7):2063 – 2068, 2009. ISSN 0022-0248. doi: 10.1016/j.jcrysgro.2008.11.056. URL `http://www.sciencedirect.com/science/article/pii/S0022024808013067`.

[159] T. Yamashita, S. Hasegawa, S. Nishida, M. Ishimaru, Y. Hirotsu, and H. Asahi. Electron field emission from GaN nanorod films grown on Si substrates with native silicon oxides. *Appl. Phys. Lett.*, 86:082109, 2005.

[160] V. M. Kaganer, K. Sabelfeld, O. Brandt, F Limbach, P. Dogan, O. Brandt, L. Geelhaar, and H. Riechert. Diffusional interaction in self-induced gan nanowire growth. *to be submitted*, 2012.

[161] D. J. As, T. Simonsmeier, B. Schöttker, T. Frey, D. Schikora, W. Kriegseis, W. Burkhardt, and B. K. Meyer. Incorporation and optical properties of magnesium in cubic GaN epilayers grown by molecular beam epitaxy. *Appl. Phys. Lett.*, 73:1835, 1998.

[162] C. G. Van de Walle and J. Neugebauer. First-principles calculations for defects and impurities: Applications to III-nitrides. *J. Appl. Phys.*, 95:3851, 2004.

[163] G. M. Dalpian and J. R. Chelikowsky. Self-purification in semiconductor nanocrystals. *Phys. Rev. Lett.*, 96:226802, 2006. doi: 10.1103/PhysRevLett.96.226802. URL http://link.aps.org/doi/10.1103/PhysRevLett.96.226802.

[164] T. Stoica and R. Calarco. Doping of III-Nitride nanowires grown by molecular beam epitaxy. *IEEE J. Sel. Top. Q. Ele.*, 17(4):859 –868, 2011. ISSN 1077-260X. doi: 10.1109/JSTQE.2010.2092416.

[165] B. Heying, R. Averbeck, L. F. Chen, E. Haus, H. Riechert, and J. S. Speck. Control of GaN surface morphologies using plasma-assisted molecular beam epitaxy. *J. Appl. Phys.*, 88(4):1855–1860, 2000. doi: 10.1063/1.1305830. URL http://link.aip.org/link/?JAP/88/1855/1.

[166] F. Furtmayr, M. Vielemeyer, M. Stutzmann, J. Arbiol, S. Estradé, F. Peirò, J. R. Morante, and M. Eickhoff. Nucleation and growth of GaN nanorods on Si(111) surfaces by plasma-assisted molecular beam epitaxy - the influence of Si- and Mg-doping. *J. Appl. Phys.*, 104(3):034309, 2008. doi: 10.1063/1.2953087. URL http://link.aip.org/link/?JAP/104/034309/1.

[167] J. Arbiol, S. Estrade, J. D. Prades, A. Cirera, F. Furtmayr, C. Stark, A. Laufer, M. Stutzmann, M. Eickhoff, M. H. Gass, A. L. Bleloch, F. Peiro, and J. R. Morante. Triple-twin domains in Mg doped GaN wurtzite nanowires: structural and electronic properties of this zinc-blende-like stacking. *Nanotechnology*, 20(14):145704, 2009. URL http://stacks.iop.org/0957-4484/20/i=14/a=145704.

[168] H. Harima. Properties of GaN and related compounds studied by means of raman scattering. *J. Phys.: Condens. Matter*, 14(38):R967, 2002.

[169] W. Limmer, W. Ritter, R. Sauer, B. Mensching, C. Liu, and B. Rauschenbach. Raman scattering in ion-implanted GaN. *Appl. Phys. Lett.*, 72(20):2589–2591, 1998. ISSN 00036951. doi: DOI:10.1063/1.121426. URL http://dx.doi.org/doi/10.1063/1.121426.

[170] Y. S. Park, J. H. Na, R. A. Taylor, C. M. Park, K. H. Lee, and T. W. Kang. The recombination mechanism of Mg-doped GaN nanorods grown by plasma-assisted molecular-beam epitaxy. *Nanotechnology*, 17(3):913, 2006. URL http://stacks.iop.org/0957-4484/17/i=3/a=049.

[171] T. Richter, H. Lüth R. Meijers, R. Calarco, and M. Marso. Doping concentration of GaN nanowires determined by opto-electrical measurements. *Nano Lett.*, 8(9):3056–3059, 2008. doi: 10.1021/nl8014395.

[172] F. Furtmayr, M. Vielemeyer, M. Stutzmann, A. Laufer, B. K. Meyer, and M. Eickhoff. Optical properties of Si-and Mg-doped gallium nitride nanowires grown by plasma-assisted molecular beam epitaxy. *J. Appl. Phys.*, 104(7):074309–074309, 2008.

[173] I. P. Smorchkova, E. Haus, B. Heying, P. Kozodoy, P. Fini, J. P. Ibbetson, S. Keller, S. P. DenBaars, J. S. Speck, and U. K. Mishra. Mg doping of GaN layers grown by plasma-assisted molecular-beam epitaxy. *Appl. Phys. Lett.*, 76:718, 2000.

[174] E. Iliopoulos, D. Doppalapudi, H. M. Ng, and T. D. Moustakas. Broadening of near-band-gap photoluminescence in n-GaN films. *Appl. Phys. Lett.*, 73:375, 1998.

[175] M. Yoshikawa, M. Kunzer, J. Wagner, H. Obloh, P. Schlotter, R. Schmidt, N. Herres, and U. Kaufmann. Band-gap renormalization and band filling in Si-doped GaN films studied by photoluminescence spectroscopy. *J. Appl. Phys.*, 86:4400, 1999.

[176] F. Limbach, T. Gotschke, T. Stoica, R. Calarco, and E. Sutter. Structural and optical properties of InGaN-GaN nanowire heterostructures grown by molecular beam epitaxy. *J. Appl. Phys.*, 109(1):014309, 2011. URL `http://link.aip.org/link/JAPIAU/v109/i1/p014309/s1&Agg=doi`.

[177] E. O. Schäfer-Nolte, T. Stoica, T. Gotschke, F. Limbach, E. Sutter, P. Sutter, and R. Calarco. Highly polarized Raman scattering anisotropy in single GaN nanowires. *Appl. Phys. Lett.*, 96:091907, 2010.

[178] N. Begum, A. S. Bhatti, F. Jabeen, S. Rubini, and F. Martelli. Lineshape analysis of Raman scattering from LO and SO phonons in III-V nanowires. *J. Appl. Phys.*, 106 (11):114317–114317, 2009.

[179] J. H. Zhu, J. Q. Ning, C. C. Zheng, S. J. Xu, S. M. Zhang, and H. Yang. Localized surface optical phonon mode in the InGaN/GaN multiple-quantum-wells nanopillars: Raman spectrum and imaging. *Appl. Phys. Lett.*, 99:113115, 2011.

[180] X. H. Wang, J. Q. Ning, S. J. Xu, and H. W. Choi. Raman and photoluminescence characterization of focused ion beam patterned InGaN/GaN multi-quantum-wells nanopillar array. *J. Appl. Phys.*, 110:093111, 2011.

[181] T. Yuasa, S. Naritsuka, M. Mannoh, K. Shinozaki, K. Yamanaka, Y. Nomura, M. Mihara, and M. Ishii. Raman scattering from coupled plasmon-LO-phonon modes in n-type $Al_xGa_{1-x}As$. *Phys. Rev. B*, 33:1222, 1986.

[182] Dow Corning Corporation. Datasheet dow corning xr-1541 e-beam resist (http://www.dowcorning.com/content/publishedlit/11-1547e-01.pdf), 2008.

[183] S. N. Mohammad. Contact mechanisms and design principles for (Schottky and Ohmic) metal contacts to semiconductor nanowires. *J. Appl. Phys.*, 108:034311, 2010.

[184] A. Motayed, M. He, A. V. Davydov, J. Melngailis, and S. N. Mohammad. Realization of reliable GaN nanowire transistors utilizing dielectrophoretic alignment technique. *J. Appl. Phys.*, 100:114310, 2006.

[185] L. M. Mansfield, K. A. Bertness, P. T. Blanchard, T. E. Harvey, A. W. Sanders, and N. A. Sanford. GaN nanowire carrier concentration calculated from light and dark resistance measurements. *J. Electron. Mater.*, 38(4):495–504, 2009.

[186] K. Jeganathan, R. K. Debnath, R. Meijers, T. Stoica, R. Calarco, D. Grutzmacher, and H. Lüth. Raman scattering of phonon-plasmon coupled modes in self-assembled GaN nanowires. *J. Appl. Phys.*, 105(12):123707, 2009.

[187] J. L. Pau, C. Bayram, P. Giedraitis, R. McClintock, and M. Razeghi. GaN nanostructured p-i-n photodiodes. *Appl. Phys. Lett.*, 93(22), 2008. ISSN 0003-6951. doi: 10.1063/1.3041641.

[188] S. Fernández-Garrido, J. Grandal, E. Calleja, M. A. Sánchez-García, and D. López-Romero. A growth diagram for plasma-assisted molecular beam epitaxy of GaN nanocolumns on Si(111). *J. Appl. Phys.*, 106(12):126102, 2009.

[189] T. Gotschke, E. O. Schäfer-Nolte, R. Caterino, F. Limbach, T. Stoica, E. Sutter, K. Jeganathan, and R. Calarco. Properties of uniform diameter InN nanowires obtained under Si doping. *Nanotechnology*, 22:125704, 2011.

[190] R. Calarco, M. Marso, T. Richter, A. I. Aykanat, R. Meijers, A. vd Hart, T. Stoica, and H. Lüth. Size-dependent photoconductivity in MBE-grown GaN-nanowires. *Nano Lett.*, 5(5):981–984, 2005.

[191] E. O. Schäfer-Nolte, T. Stoica, T. Gotschke, F. A. Limbach, E. Sutter, P. Sutter, D. Grützmacher, and R. Calarco. Enhanced light scattering of the forbidden longitudinal optical phonon mode studied by micro-Raman spectroscopy on single InN nanowires. *Nanotechnology*, 21:315702, 2010.

[192] Y. S. Park and H. Im. Spatially-resolved cathodoluminescence in GaN nanorods and in AlGaN/GaN multiquantum discs having different quantum confinement states. *J. Korean Phys. Soc.*, 54:1730, 2009.

[193] L. T. Romano, J. E. Northrup, A. J. Ptak, and T. H. Myers. Faceted inversion domain boundary in GaN films doped with Mg. *Appl. Phys. Lett.*, 77:2479, 2000.

[194] A. J. Ptak, T. H. Myers, L. T. Romano, C. G. Van de Walle, and J. E. Northrup. Magnesium incorporation in GaN grown by molecular-beam epitaxy. *Appl. Phys. Lett.*, 78(3):285–287, 2001.

[195] X. Kong, G. Q. Hu, X. F. Duan, Y. Lu, and X. L. Liu. Polarity determination for GaN thin films by electron energy-loss spectroscopy. *Appl. Phys. Lett.*, 81(11):1990–1992, 2002. ISSN 00036951. doi: DOI:10.1063/1.1504876. URL `http://dx.doi.org/doi/10.1063/1.1504876`.

[196] A. Cavallini, L. Polenta, M. Rossi, T. Richter, M. Marso, R. Meijers, R. Calarco, and H. Lüth. Defect distribution along single GaN nanowhiskers. *Nano Lett.*, 6(7):1548–1551, 2006. doi: 10.1021/nl060332n. URL `http://pubs.acs.org/doi/abs/10.1021/nl060332n`.

[197] M. Knelangen, M. Hanke, E. Luna, L. Schrottke, O. Brandt, and A. Trampert. Monodisperse (In,Ga)N insertions in catalyst-free-grown GaN(0001) nanowires. *Nanotechnology*, 22(36):365703, 2011. URL `http://stacks.iop.org/0957-4484/22/i=36/a=365703`.

[198] V. M. Kaganer, M. Wölz, O. Brandt, L. Geelhaar, and H. Riechert. X-ray diffraction profiles from axial nanowire heterostructures. *Phys. Rev. B*, 83:245321, 2011. doi: 10.1103/PhysRevB.83.245321. URL `http://link.aps.org/doi/10.1103/PhysRevB.83.245321`.

[199] M. Wölz, V. M. Kaganer, O. Brandt, L. Geelhaar, and H. Riechert. Analyzing the growth of $In_xGa_{1-x}N$/GaN superlattices in self-induced GaN nanowires by X-ray diffraction. *Appl. Phys. Lett.*, 98(26):261907, 2011. ISSN 00036951. doi: DOI:10.1063/1.3604810. URL `http://dx.doi.org/doi/10.1063/1.3604810`.

[200] I. Ho and G. B. Stringfellow. Solid phase immiscibility in GaInN. *Appl. Phys. Lett.*, 69:2701, 1996.

[201] T. Böttcher, S. Einfeldt, V. Kirchner, S. Figge, H. Heinke, D. Hommel, H. Selke, and P. L. Ryder. Incorporation of indium during molecular beam epitaxy of InGaN. *Appl. Phys. Lett.*, 73:3232, 1998.

[202] P. Waltereit, O. Brandt, K. H. Ploog, M. A. Tagliente, and L. Tapfer. In surface segregation during growth of (In,Ga)N/GaN multiple quantum wells by plasma-assisted molecular beam epitaxy. *Phys. Rev. B*, 66(16):165322, 2002.

[203] C. C. Hong, H. Ahn, C. Y. Wu, and S. Gwo. Strong green photoluminescence from $In_xGa_{1-x}N$/GaN nanorod arrays. *Opt. Express*, 17:17227, 2009.

[204] G. Tourbot, C. Bougerol, A. Grenier, M. Den Hertog, D. Sam-Giao, D. Cooper, P. Gilet, B. Gayral, and B. Daudin. Structural and optical properties of InGaN/GaN nanowire heterostructures grown by PA-MBE. *Nanotechnology*, 22:075601, 2011.

[205] J. Segura-Ruiz, G. Martinez-Criado, J. A. Sans, R. Tucoulou, P. Cloetens, I. Snigireva, C. Denker, J. Malindretos, A. Rizzi, M. Gomez-Gomez, N. Garro, and A. Cantarero. Direct observation of elemental segregation in InGaN nanowires by X-ray nanoprobe. *Phys. Status Solidi RRL*, 5:95, 2011.

[206] L. Polenta, M. Rossi, A. Cavallini, R. Calarco, M. Marso, R. Meijers, T. Richter, T. Stoica, and H. Lüth. Investigation on localized states in GaN nanowires. *ACS Nano*, 2(2):287–292, 2008. doi: 10.1021/nn700386w. URL `http://pubs.acs.org/doi/abs/10.1021/nn700386w`.

[207] S. Hernández, R. Cuscó, D. Pastor, L. Artús, K. P. O'Donnell, R. W. Martin, I. M. Watson, Y. Nanishi, and E. Calleja. Raman-scattering study of the InGaN alloy over the whole composition range. *J. Appl. Phys.*, 98(1):013511, 2005. ISSN 00218979. doi: DOI:10.1063/1.1940139. URL `http://dx.doi.org/doi/10.1063/1.1940139`.

[208] E. Alarcón-Lladó, R. Cuscó, L. Artús, J. Jiménez, B. Wang, and M. Callahan. Raman scattering of quasimodes in ZnO. *J. Phys.: Condens. Matter*, 20(44):445211, 2008. URL `http://stacks.iop.org/0953-8984/20/i=44/a=445211`.

[209] A. Kikuchi, M. Kawai, M. Tada, and K. Kishino. InGaN/GaN multiple quantum disk nanocolumn light-emitting diodes grown on (111)Si substrate. *Jpn. J. Appl. Phys. Part 2 Let.*, 43(12A):L1524–L1526, 2004. ISSN 0021-4922. doi: 10.1143/JJAP.43.L1524.

[210] G. Kunert, W. Freund, T. Aschenbrenner, C. Kruse, S. Figge, M. Schowalter, A. Rosenauer, J. Kalden, K. Sebald, J. Gutowski, M. Feneberg, I. Tischer, K. Fujan, K. Thonke, and D. Hommel. Light-emitting diode based on mask- and catalyst-free grown N-polar GaN nanorods. *Nanotechnology*, 22(26):265202, 2011. URL `http://stacks.iop.org/0957-4484/22/i=26/a=265202`.

[211] A.-L. Bavencove, G. Tourbot, J. Garcia, Y. Désières, P. Gilet, F. Levy, B. André, B. Gayral, B. Daudin, and L. S. Dang. Submicrometre resolved optical characterization of green nanowire-based light emitting diodes. *Nanotechnology*, 22(34):345705, 2011. URL `http://stacks.iop.org/0957-4484/22/i=34/a=345705`.

[212] M.-H. Kim, M. F. Schubert, Q. Dai, J. K. Kim, E. F. Schubert, J. Piprek, and Y. Park. Origin of efficiency droop in GaN-based light-emitting diodes. *Appl. Phys. Lett.*, 91(18):183507, 2007. ISSN 00036951. doi: DOI:10.1063/1.2800290. URL `http://dx.doi.org/10.1063/1.2800290`.

[213] A. Forchel and P. Malinverni. European commission technology roadmap - optoelectronic interconnects for integrated circuits, ftp://ftp.cordis.europa.eu/pub/esprit/docs/meloprm2.pdf. FTP server, 1998. URL `ftp://ftp.cordis.europa.eu/pub/esprit/docs/meloprm2.pdf`.

[214] S. S. Iyer and Y. H. Xie. Light emission from silicon. *Science*, 260(5104):40, 1993.

[215] Z. H. Lu, D. J. Lockwood, and J. M. Baribeau. Quantum confinement and light emission in SiO_2/Si superlattices. *Nature*, 378:258–260, 1995.

[216] T. Komoda, J. Kelly, F. Cristiano, A. Nejim, P. L. F. Hemment, K. P. Homewood, R. Gwilliam, J. E. Mynard, and B. J. Sealy. Visible photoluminescence at room temperature from microcrystalline silicon precipitates in SiO_2 formed by ion implantation. *Nucl. Inst. and Meth. in Phys. Res. Sec. B*, 96(1):387–391, 1995.

[217] B. Zheng, J. Michel, F. Y. G. Ren, L. C. Kimerling, D. C. Jacobson, and J. M. Poate. Room-temperature sharp line electroluminescence at λ= 1.54 μm from an erbium-doped, silicon light-emitting diode. *Appl. Phys. Lett.*, 64(21):2842–2844, 1994.

[218] L. Vescan and T. Stoica. Room-temperature SiGe light-emitting diodes. *J. Lumin.*, 80(1):485–489, 1998.

[219] D. Leong, M. Harry, K. J. Reeson, and K. P. Homewood. A silicon/iron-disilicide light-emitting diode operating at a wavelength of 1.5 μm. *Nature*, 387(6634):686–688, 1997.

[220] W. L. Ng, M. A. Lourenco, R. M. Gwilliam, S. Ledain, G. Shao, and K. P. Homewood. An efficient room-temperature silicon-based light-emitting diode. *Nature*, 410(6825):192–194, 2001.

[221] B. Huang, X. Zhang, W. Wang, Z. Dong, N. Guan, Z. Zhang, and H. Chen. Cmos monolithic optoelectronic integrated circuit for on-chip optical interconnection. *Opt. Commun.*, 284:16–17, 2011.

[222] K. D. Hirschman, L. Tsybeskov, S. P. Duttagupta, and P. M. Fauchet. Silicon-based visible light-emitting devices integrated into microelectronic circuits. *Nature*, 384: 338–341, 1996.

[223] H.W. Lin, Y.J. Lu, H.Y. Chen, H.M. Lee, and S. Gwo. InGaN/GaN nanorod array white light-emitting diode. *Appl. Phys. Lett.*, 97:073101, 2010.

[224] H. P. T. Nguyen, S. Zhang, K. Cui, X. Han, S. Fathololoumi, M. Couillard, G. A. Botton, and Z. Mi. p-type modulation doped InGaN/GaN dot-in-a-wire white-light-emitting diodes monolithically grown on Si(111). *Nano Lett.*, 11(5):1919, 2011.

[225] A.L. Bavencove, D. Salomon, M. Lafossas, B. Martin, A. Dussaigne, F. Levy, B. André, P. Ferret, C. Durand, J. Eymery, et al. Light emitting diodes based on GaN core/shell wires grown by MOVPE on n-type Si substrate. *Electron. Lett.*, 47(13): 765–767, 2011.

[226] K. Tomioka, J. Motohisa, S. Hara, K. Hiruma, and T. Fukui. GaAs/AlGaAs core multishell nanowire-based light-emitting diodes on Si. *Nano Lett.*, 10(5):1639–1644, 2010.

[227] H. Takeuchi, A. Wung, X. Sun, R. T. Howe, and T. J. King. Thermal budget limits of quarter-micrometer foundry CMOS for post-processing MEMS devices. *IEEE Trans. Electron. Dev.*, 52(9):2081–2086, 2005.

[228] W. Yun, R. T. Howe, and P. R. Gray. Surface micromachined, digitally force-balanced accelerometer with integrated CMOS detection circuitry. In *IEEE Solid-State Sensor and Actuator Workshop, 1992. 5th Technical Digest.*, pages 126–131. IEEE, 1992.

[229] Y. Furukawa, H. Yonezu, and A. Wakahara. Monolithic integration of III-V active devices into silicon platform for optoelectronic integrated circuits. *IEICE Trans. on Elec.*, 91(2):145–149, 2008.

[230] H. K. Choi, J. P. Mattia, G. W. Turner, and B. Y. Tsaur. Monolithic integration of GaAs/AlGaAs LED and Si driver circuit. *IEEE Elec. Dev. Lett.*, 9(10):512–514, 1988.

[231] K. Chilukuri, M. J. Mori, C. L. Dohrman, and E. A. Fitzgerald. Monolithic CMOS-compatible AlGaInP visible LED arrays on silicon on lattice-engineered substrates (SOLES). *Semiconductor science and technology*, 22:29, 2007.

[232] R. K. Debnath. *Growth of undoped and doped III-Nitride nanowires and their characterization*. PhD thesis, Rheinisch-Westfälischen Technischen Hochschule Aachen, 2009.

[233] M. A. Herman and H. Sitter. *Molecular beam epitaxy: fundamentals and current status*. Springer-Verlag Berlin, 1989.

List of Figures

List of Tables

Aknowledgments

The studies leading up to this thesis have been performed at the Instutute for Bio- and Nanosystems (IBN-1) (now Peter Grünberg Institute 9) at the Forschungszentrum Jülich GmbH in Jülich and at the Paul-Drude Institut für Festkörperelektronik in Berlin.

I would like to express my gratitude to all the people who supported and guided me during this time. In particular, I would like to thank:

Prof. Dr. Henning Riechert and Prof. Dr. Detlev Grützmacher for giving me the opportunity to perform these studies at their respective institutes.

Prof. Dr. Hans Lüth and Prof. Dr. Ted Masselink for excepting the task of reviewing this thesis.

Dr. Raffaella Calarco for receiving me in her team, the guidance she provided with her expertise, the careful correction of the thesis draft and for becoming a friend.

Dr. Lutz Geelhaar for the guidance he provided and making the relocation to PDI easy.

Dr. Toma Stoica for sharing his wisdom and experience with me and for the advise he gave me.

Dr. Tobias Gotschke for being a friend and companion in the pursuit of our PhD. All the shared office time and the help he offered whenever there was a need for it.

Roberta Caterino, Eike Schäfer-Nolte, Timo Schumann and Martin Wölz for their support with all the experiments and the great atmosphere I got to enjoy and proof reading of the manuscript.

Oliver Brandt, Christan Hauswald, Jonas Lähnemann, Carsten Püller, Manfred Ramsteiner and Martin Wienhold for the spectroscopic investigation of the NW and the great input and close collaboration I got to enjoy.

Luis Artus, Moritz Bommer, Jim Ciston, Ramon Cusco, Milena Erenburg, Sebastian Geburt, Sven Höfling, Kong Xiang, Stefan Kremling, Johannes Ledig, Carsten Ronning, Eli Sutter, Peter Sutter, Achim Trampert and Lukas Worschech for various kinds of measurements on my NWs.

Karl-Heinz Deussen, Claudia Hermann, Gert Jaschke and Hans-Peter Schönherr for the technical support with the MBE machines.

Anne-Kathrin Bluhm and Hans Peter Bochem for SEM images.

Aknowledgments

Heinz-Josef Penkalla for teaching me how to use a TEM.

The clean room teams at the FZ Jülich and at PDI for their constant support with the processing of my samples.

The whole nanowire group at PDI for listening to me and giving me feedback and ideas.

All the colleagues at the FZ Jülich and the PDI who have not been named directly but made my experience of staying with you a very pleasant one.

Meinen Eltern die mich immer unterstützt haben.

Silke die die Schwierigkeiten auf sich genommen hat die durch den Wechsel entstanden sind.

Selbständigkeitserklärung

Ich erkläre, dass ich die vorliegende Arbeit selbständig und nur unter Verwendung der angegebenen Literatur und Hilfsmittel angefertigt habe.

Berlin, den 13.03.2012 Friederich Limbach